

NORTHWESTERN UNIVERSITY

Multiscale Assessment of the Role of Particle-Scale Attributes on  
the Crushability of Granular Soils

A DISSERTATION

SUMMITTED TO THE GRADUATE SCHOOL  
IN PARTIAL FULFILLMENT OF THE REQUIREMENTS

for the degree

DOCTOR OF PHILOSOPHY

Field of Civil and Environmental Engineering

By

Changbum Sohn

EVANSTON, ILLINOIS

December 2018

© Copyright by Changbum Sohn 2018

All Rights Reserved

## ABSTRACT

Granular materials are ubiquitous elements of our daily life, representing some of the most manipulated materials on Earth and playing a key role in disparate fields of science and engineering. Considerable research has been performed to explore the factors that impact the mechanical behavior of granular materials. Within this context, major challenges derive from the analysis of granular material behavior at high confining pressure, in that under those conditions particles fracture, leading to localized deformation and major microstructural changes. Despite the importance of these processes, we still do not know how the shape of the grains affect the fracture mechanisms leading to comminution, how these mechanisms evolve during deformation, and whether the same processes triggered during external loading remain active during the spontaneous deformation stages often observed during long-term creep. Further progress is therefore necessary to clarify these open questions and understand the multi-scale mechanics of granular geomaterials. This study has the goal to fill these gaps in knowledge by exploring the role of particle attributes (e.g., size and shape) on the continuum-scale mechanical behavior of these materials, by placing particular emphasis on both instantaneous and delayed comminution, i.e. the fragmentation of the particles that constitute a granular solid.

This thesis discusses experiments conducted at particle and assembly scales on coarse-grained materials and interprets them in light of fracture mechanics theories. First, diametral compression tests on particles of varying size have been conducted to measure the energy stored in individual grains at the onset of fracture. Then, oedometric compression tests on samples made of the same particles have been performed to measure the yielding pressure, as well as to track the evolution of breakage. These experiments have been used to test the performance of recently proposed

scaling laws bridging the energy released by a single particle with the work input required to comminute an assembly.

Additionally, creep tests have been performed on quartz sands to evaluate the role of particle attributes on the accumulation of creep deformation, as well as the delayed breakage growth over time. The viscous breakage theory is further used to simulate the creep stress-strain response, evolution of particle gradation and delayed breakage growth of all tested sands with the purpose of quantifying the model parameters and validating the theoretical hypotheses.

Moreover, synchrotron X-ray microtomography is used to directly characterize how the particle shape affects the feedbacks between collective comminution and individual grain fracture. Rounded and angular sands are compressed beyond their comminution pressure and imaged at the microscale. An analytical study is further conducted to quantify grain-scale processes responsible for comminution. Lastly, the imaging technique is further used to directly confirm the experimental and numerical findings on time effects.

Finally, a discrete element method is used to simulate diametral, oedometric, and creep compression tests. These virtual laboratory experiments have the purpose to demonstrate how the local particle failure impacts to the collective breakage response, considering particle-to-particle interactions. To conclude, the main findings of the thesis are summarized and some directions for future research are discussed.

## ACKNOWLEDGEMENTS

I would like to express my sincere gratitude to the countless people who have supported me to have the privileged opportunity to study and pursue the research activity toward the doctoral degree at Northwestern University. I would like to thank my advisor, **Dr. Giuseppe Buscarnera**. He has not only provided the academic support, guidance, and encouragement, but also cultivated my fundamental knowledge in engineering and science. Under his outstanding supervision, I have enhanced my academic competence and performance along with persistence, fortitude, endurance and positive mindset. Moreover, I would like to extend my gratitude to the committee members: **Dr. Richard Finno and Dr. James Hambleton** for their critiques and appraisals. Their comments, feedback, and discussion have served to expand my comprehensive understandings in geotechnical engineering. Many colleagues, students, and friends have contributed to the success of my doctoral study, either directly or indirectly. I am indebted to my colleagues, **Dr. Mehmet B. Cil and Dr. Yida Zhang** for sharing their expertise and experience during the several stages of this research. Special thanks to: **Dr. Carmine Polito** for drawing my attention to geotechnical engineering, and encouraging me to pursue the graduate education at Northwestern University. **Dr. Mark Rivers, Dr. Denis T. Keane, and Dr. William (Mike) Guise** for allowing a flexible beamtime schedule and hands-on assistance to the use of synchrotron X-ray microtomography at 13-BM-D and 5-BM-C facilities of the Advanced Photon Source in Argonne National Laboratory, Illinois. **Mr. Luis Avila, Dr. Sangrae Kim, Mr. Minhyeok Ko, Mr. Yechan Won, Ms. Eunhye Kim, Ms. Dawa Seo, Ms. Jieun Kim, and Mr. Hyunjin Lee** for accompanying me and creating unforgettable experiences throughout my studies at Northwestern University.

## LIST OF NOTATIONS AND ABBREVIATIONS

### Latin Symbols

$a', b'$  : collective coefficient in particle fracture energy models

$a$  : half length of a crack

$a_c$  : particle-to-particle contact radius

$A_s$  : tangent of the inclination angle of the conical surface with respect to the platen

$B$  : breakage value or index

$\dot{B}$  : breakage growth rate

$\dot{B}_0$  : reference breakage growth rate

$C$  : circularity

$d_{50}$  : grain size corresponding to 50% pass by mass on the grain size distribution (GSD) curve

$d_M, d_m$  : maximum and minimum grain diameter, respectively

$d, d_p$  : particle diameter

$e$  : void ratio

$E$  : Young's modulus

$E_B$  : breakage energy

$E_c$  : critical breakage energy

$E_{pc}$  : particle fracture energy per unit volume

$F_0, F, F_u$  : initial, current, and ultimate cumulative GSD

$F_f$  : failure load in single particle for diametral compression test

$F_n$  : normal contact force

$G_{IC}$ : critical energy release rate

$k_n, k_s$ : normal and shear stiffness

$k_0, K_0$ : at-rest earth pressure coefficient

$K, G$ : bulk and shear modulus

$K_I$ : stress intensity factor at mode I

$K_{I0}$ : corrosion limit in terms of stress intensity factor

$K_{IC}$ : critical stress intensity factor of mode I crack

$\bar{K}, \bar{G}$ : non-dimensional bulk and shear modulus

$\dot{l}$ : crack velocity

$\dot{l}_0$ : reference crack velocity

$M$ : slope of critical state line in  $p$ - $q$  space

$m$ : pressure-dependent coefficient for elastic modulus

$p, p'$ : mean total and effective stress

$P_r$ : reference pressure

$q$ : deviatoric stress

$R$ : roundness

$S$ : sphericity

$t_B$ : characteristic breakage time

$t_f$ : time-to-failure of single particle at static fatigue

$U_n$ : particle overlap in discrete element model

$V_p$ : particle volume

$w_m$ : Weibull modulus

## Greek Symbols

$\alpha$  : fractal dimension

$\alpha_c$  : dimensionless crack radius

$\bar{\alpha}_f$  : average number of cumulated fragments

$\bar{\beta}_f$  : average number of new fragments generated by the particles which continue to crush upon successive loading steps

$\gamma$  : surface energy of a solid

$\Delta$  : displacement of the loading platen in single particle crushing test

$\delta$  : contact deformation

$\varepsilon_v, \varepsilon_s$  : volumetric and deviatoric strain

$\vartheta_M$  : mechanical grading index

$\lambda_c, \lambda_B$  : slope of a trendline of creep strain and delayed breakage growth rate, respectively

$\mu$  : frictional coefficient

$\nu$  : Poisson's ratio

$\xi$  : scaling factor

$\xi_c, \xi_B$  : fracture and breakage overstress function

$\sigma_a$  : axial stress

$\sigma_{pc}$  : particle characteristic stress

$\sigma_r$  : radial stress

$\sigma_y$  : macroscopic yield stress

$\phi$  : friction angle

$\phi_B$  : higher-order energy dissipation during time-dependent grain crushing

$\Phi$ : rate of energy dissipation of the system

$\chi$  : fitting parameter for a reference delayed breakage growth rate (or characteristic breakage time) of grains

$\Psi$  : Helmholtz free energy (or elastic strain energy) of the system

$\omega$  : breakage-friction coupling angle

### **Abbreviations**

A/D : analog-to-digital

CCD : charge coupled device

DEM : discrete element method

EXP : experiment

IDL : interactive data language

FE : flatness-elongation ratio

GSD : grain size distribution

LVDT : linear variable differential transformer

OED : oedometric

OSS : octahedral shear stress

REV : representative elementary volume

SEM : scanning electron microscope

SMT: synchrotron microtomography

VBM : viscous breakage mechanics

*I dedicate this study to my family, Hee Ik Sohn, Byung Ohk Park, and Changmo Sohn, whose love and unconditional support over many years laid the foundations for the discipline and application necessary to complete this work.*

## TABLE OF CONTENTS

|                                                      |    |
|------------------------------------------------------|----|
| ABSTRACT.....                                        | 3  |
| ACKNOWLEDGEMENTS.....                                | 5  |
| LIST OF NOTATIONS AND ABBREVIATIONS.....             | 6  |
| LIST OF FIGURES.....                                 | 16 |
| LIST OF TABLES.....                                  | 26 |
| CHAPTER 1: INTRODUCTION.....                         | 27 |
| CHAPTER 2: PREVIOUS STUDIES AND BACKGROUND.....      | 32 |
| 2.1 Mechanical Behavior of Crushable Soils.....      | 32 |
| 2.1.1 Particle fracture models.....                  | 33 |
| 2.1.2 Continuum breakage mechanics theory.....       | 36 |
| 2.2 Delayed Particle Crushing.....                   | 37 |
| 2.2.1 Subcritical crack growth theory.....           | 37 |
| 2.2.2 Viscous breakage mechanics theory.....         | 40 |
| 2.3 X-ray Microtomography Imaging.....               | 41 |
| 2.4 Discrete Element Modeling Analyses.....          | 42 |
| 2.5 Potential Areas of Interest.....                 | 44 |
| 2.5.1 Pile driving and penetration.....              | 44 |
| 2.5.2 Subsidence.....                                | 46 |
| 2.5.3 Mechanics of fault gouge.....                  | 47 |
| CHAPTER 3: LABORATORY EQUIPMENT AND METHODOLOGY..... | 49 |
| 3.1 Introduction.....                                | 49 |
| 3.2 Testing Materials.....                           | 49 |

|                                                                   |    |
|-------------------------------------------------------------------|----|
|                                                                   | 12 |
| 3.3 Miniaturized Test Apparatus .....                             | 52 |
| 3.3.1 Description and design .....                                | 52 |
| 3.3.2 Diametral compression tests.....                            | 54 |
| 3.3.3 Oedometric compression tests.....                           | 56 |
| 3.3.4 Creep tests .....                                           | 58 |
| 3.4 One-dimensional Consolidation Test Apparatus.....             | 58 |
| 3.4.1 Description and design .....                                | 58 |
| 3.4.2 Oedometer test.....                                         | 60 |
| 3.4.3 Creep test.....                                             | 61 |
| CHAPTER 4: COMPRESSION OF CRUSHABLE GRANULAR SOILS .....          | 63 |
| 4.1 Introduction .....                                            | 63 |
| 4.2 Theoretical Background .....                                  | 65 |
| 4.2.1 Particle-scale fracture models .....                        | 65 |
| 4.2.2 Continuum breakage models.....                              | 66 |
| 4.2.3 Bridging microscopic and macroscopic processes.....         | 69 |
| 4.3. Testing Materials and Procedures.....                        | 70 |
| 4.4. Interpretation of Experimental Results: Particle-scale ..... | 70 |
| 4.4.1 Contact elasticity .....                                    | 70 |
| 4.4.2 Particle fracture mechanism .....                           | 73 |
| 4.5. Interpretation of Experimental Results: Specimen-scale.....  | 76 |
| 4.5.1 Macroscopic yield stress and critical breakage energy ..... | 76 |
| 4.5.2 Breakage evolution.....                                     | 80 |
| 4.6. Concluding Remarks .....                                     | 82 |

|                                                                              |     |
|------------------------------------------------------------------------------|-----|
|                                                                              | 13  |
| CHAPTER 5: TIME EFFECTS ON THE COMMINUTION OF SANDS.....                     | 84  |
| 5.1 Introduction .....                                                       | 84  |
| 5.2 Theoretical Background .....                                             | 86  |
| 5.3 Test Materials and Procedures.....                                       | 91  |
| 5.4 Results and Data Analysis .....                                          | 91  |
| 5.4.1 Measurement of concurrent creep and breakage evolution.....            | 91  |
| 5.4.2 Data interpretation based on the kinetics breakage theory.....         | 95  |
| 5.5 Model Simulations.....                                                   | 99  |
| 5.6 Concluding Remarks .....                                                 | 108 |
| CHAPTER 6: X-RAY TOMOGRAPHY FOR PARTICLE COMMINUTION .....                   | 110 |
| 6.1 Introduction .....                                                       | 110 |
| 6.2 Synchrotron X-ray Microtomography .....                                  | 112 |
| 6.2.1 Imaging facility at Argonne National Laboratory, IL USA .....          | 112 |
| 6.2.2 SMT imaging for oedometer tests.....                                   | 113 |
| 6.2.3 SMT imaging for 24-hour Creep.....                                     | 115 |
| 6.3 Analyses of SMT Images .....                                             | 117 |
| 6.4 Results and Data Interpretation .....                                    | 118 |
| 6.4.1 Validation of post-processed SMT image analyses .....                  | 118 |
| 6.4.2 Effect of particle shape on soil crushability .....                    | 119 |
| 6.4.3 Impact of initial particle shape on the evolution of fragments.....    | 120 |
| 6.4.4 Quantification of particle failure mode .....                          | 122 |
| 6.4.5 Micro-Macro comparison for yielding stress and compression index ..... | 130 |
| 6.4.6 Creep behavior of geomaterials.....                                    | 131 |

|                                                                                              |     |
|----------------------------------------------------------------------------------------------|-----|
|                                                                                              | 14  |
| 6.4.7 Particle gradation over 24-hour creep .....                                            | 132 |
| 6.4.8 Comparison between delayed breakage growth and creep strain .....                      | 136 |
| 6.4.9 Micro-Macro comparison for delayed breakage growth rate and creep strain rate<br>..... | 136 |
| 6.5 Concluding Remarks .....                                                                 | 137 |
| CHAPTER 7: DEM MODELING OF SOIL CRUSHING.....                                                | 140 |
| 7.1 Introduction .....                                                                       | 140 |
| 7.2 Technical Background.....                                                                | 142 |
| 7.2.1 Overview of DEM.....                                                                   | 142 |
| 7.2.2 Contact models and failure law .....                                                   | 142 |
| 7.2.3 Particle replacement configuration.....                                                | 144 |
| 7.3 3D Virtual Assessment of Soil Crushing.....                                              | 145 |
| 7.3.1 Single particle crushing simulation .....                                              | 145 |
| 7.3.2 Oedometric compression simulation.....                                                 | 147 |
| 7.3.3 Creep simulation .....                                                                 | 150 |
| 7.4 Concluding Remarks .....                                                                 | 155 |
| CHAPTER 8: CONCLUSIONS .....                                                                 | 156 |
| 8.1 Main Conclusions.....                                                                    | 156 |
| 8.2 Future Scope of Work.....                                                                | 158 |
| REFERENCES .....                                                                             | 160 |
| APPENDIX A: FRACTURE MODELS .....                                                            | 173 |
| A.1 Surface Crack Model .....                                                                | 173 |
| A.2 Central Crack Model.....                                                                 | 173 |

|                                                                                           |     |
|-------------------------------------------------------------------------------------------|-----|
|                                                                                           | 15  |
| APPENDIX B: CONTACT MODELS.....                                                           | 174 |
| B.1 Linear Contact Model .....                                                            | 174 |
| B.2 Hertzian Contact Model.....                                                           | 174 |
| B.3 Conical Contact Model .....                                                           | 175 |
| APPENDIX C: COMBINATION OF FAILURE MODEL AND CONTACT MODEL.....                           | 176 |
| C.1 Surface Crack.....                                                                    | 176 |
| C.1.1 Hertzian contact model.....                                                         | 176 |
| C.2 Central Crack .....                                                                   | 176 |
| C.2.1 Linear contact model .....                                                          | 176 |
| C.2.2 Hertzian contact model.....                                                         | 176 |
| C.2.3 Conical contact model .....                                                         | 177 |
| APPENDIX D: TIME-TO-FAILURE OF PARTICLE BASED ON SUBCRITICAL CRACK<br>GROWTH THEORY ..... | 178 |

## LIST OF FIGURES

|                                                                                                                                                                                                                                                                                                              |    |
|--------------------------------------------------------------------------------------------------------------------------------------------------------------------------------------------------------------------------------------------------------------------------------------------------------------|----|
| Figure 1. (left): Normalized survival probability curves of quartz sand at failure, and (right): Grain size distribution curves before and after loading (Nakata et al., 2001b) .....                                                                                                                        | 32 |
| Figure 2. One-dimensional compression plots for three different size ranges of sand (McDowell, 2002) .....                                                                                                                                                                                                   | 33 |
| Figure 3. Prediction of failure mechanism for silica sands (data from Nakata et al. (2001b)) with various grain size ranges (Zhang et al., 2016) .....                                                                                                                                                       | 35 |
| Figure 4. (a) Analytical solutions of $E_{pc}$ - $\sigma_{pc}$ relationship for contact law exhibiting the linear (or flat), Hertzian and conical contact models correspond to slopes of 2.0, 1.66 and 1.5; (b) predictions of the combinations of failure modes and contact laws (Zhang et al., 2016) ..... | 35 |
| Figure 5. Example of model predictions on the propagation of crack length.....                                                                                                                                                                                                                               | 39 |
| Figure 6. 2D grey-scale image of single particle used for quantitative analysis on fracture patterns (Zhao et al., 2015).....                                                                                                                                                                                | 42 |
| Figure 7. Direct visualization of local grain failure during triaxial compression test on Hostun sand (Andò et al., 2013) .....                                                                                                                                                                              | 42 |
| Figure 8. DEM simulation of confined compression of a particle chain indicating the effect of the number of sub-particles within the agglomerate in the simulated crushing response of granular materials (Cil and Alshibli, 2015) .....                                                                     | 44 |
| Figure 9. DEM simulation of stress-strain and volumetric response under triaxial compression (Tapias et al., 2015) .....                                                                                                                                                                                     | 44 |
| Figure 10. Normalized vertical displacement after cone penetration (left): relative density, $D_R = 45\%$ ; (Right): relative density, $D_R = 82\%$ (Arshad et al., 2014).....                                                                                                                               | 45 |

|                                                                                                                                                                                                                                                                                                                                                                                              |    |
|----------------------------------------------------------------------------------------------------------------------------------------------------------------------------------------------------------------------------------------------------------------------------------------------------------------------------------------------------------------------------------------------|----|
| Figure 11. Cumulative subsidence of sand reservoir. Active production for the 17-year period (1965 – 1982) induced sand reservoir compaction, which resulted in the maximum surface subsidence of nearly 8 cm. Slow pore pressure drainage from the bounding shale resulted in an additional 8 cm subsidence for the first 10 years after depletion (1982 – 1992) (Chang et al., 2014) ..... | 46 |
| Figure 12. An impact of particle crushing on the ground subsidence .....                                                                                                                                                                                                                                                                                                                     | 47 |
| Figure 13. Effect of confined comminution on the physics of fault gouge. ....                                                                                                                                                                                                                                                                                                                | 48 |
| Figure 14. SEM images of (a) angular Q-ROK#1 sands; (b) Q-ROK#2 sands; (c) Q-ROK#4 sands; (d) rounded 20/40 sieved Ottawa sands; (e) spherical small glass beads (SGB); (f) medium glass beads (MGB); (g) large glass beads (LGB). Particles of the same class with different size exhibit similar shape characteristics .....                                                               | 51 |
| Figure 15. Initial grain size distribution curves of (a) 4 Silica sands and (b) 3 glass beads.....                                                                                                                                                                                                                                                                                           | 52 |
| Figure 16. Schematic of the miniature compression test cell used for the multiscale laboratory experiments .....                                                                                                                                                                                                                                                                             | 53 |
| Figure 17. A layout of the LABVIEW software for data acquisition of force and displacement measurements.....                                                                                                                                                                                                                                                                                 | 54 |
| Figure 18. General setup of a diametral compression test .....                                                                                                                                                                                                                                                                                                                               | 55 |
| Figure 19. Schematic of the typical set-up for the miniaturized oedometer compression and creep tests .....                                                                                                                                                                                                                                                                                  | 57 |
| Figure 20. Schematic of the LoadTrac-II load frame for consolidation tests .....                                                                                                                                                                                                                                                                                                             | 59 |
| Figure 21. Setup for the oedometer test using the LoadTrac-II load frame.....                                                                                                                                                                                                                                                                                                                | 60 |
| Figure 22. Setup for the creep test using LoadTrac-II load frame.....                                                                                                                                                                                                                                                                                                                        | 62 |

Figure 23. Schematics of two typical fracture modes: (a)-(c) contact failure due to local asperity damage; central splitting due to high tensile stresses on the median plane (d)-(f); (a) and (d): initial stage; (b) and (e) loading stage; (c) and (f): final stage ..... 66

Figure 24. Examples of crushing tests for individual particles: (a) Q-ROK sand ( $d_p = 1.07\text{mm}$ ; with calibrated contact elasticity parameters:  $E = 95.6\text{ GPa}$ ,  $E_{optimized} = 4.90\text{ GPa}$ ,  $\nu = 0.077$ ,  $a_c/R = 0.072$  and  $A_s = 7.5$ ); (b) glass beads ( $d_p = 1.09\text{mm}$ ; with calibrated contact elasticity parameters:  $E = 70.0\text{ GPa}$ ,  $\nu = 0.30$ ,  $a_c/R = 0.316$  and  $A_s = 1.0$  and  $A_{s\_optimized} = 0.020$ ). Calibrated parameters specific for the selected example curves, thus not coincident with those in Table 3, where averaged values based on a total number of 90 particles of Q-ROK sand and glass bead have been considered ..... 71

Figure 25. Energy-particle strength relationship for (a) Q-ROK sands and (b) glass beads with calibrated model predictions based on different elastic contact models..... 73

Figure 26. All particle strength obtained from diametral compression of (a) Q-ROK sand particles and (b) glass beads. The data cloud represents the characteristic particle strengths computed for each batch of particles on the basis of 30 experiments. Averaged particle strength with 95% confidence interval of (c) Q-ROK sands and (d) glass beads. The average values have been used to analyze the observed dataset for each batch of particles. .... 74

Figure 27. Values of volume-specific energy at fracture ( $E_{pc}$ ) plotted as a function of particle diameter for (a) Q-ROK sand particles and (b) glass beads, along with prediction of four combinations of contact and fracture models. The data cloud represents the values of  $E_{pc}$  computed for each batch of particles on the basis of 30 experiments. Averaged  $E_{pc}$  with

- 95% confidence interval of (c) Q-ROK sands and (d) glass beads. The average values have been used to analyze the observed dataset for each batch of particles. .... 75
- Figure 28. Oedometric compression tests results and model simulations based on the breakage mechanics model for: (a) Q-ROK sands and (b) glass beads ..... 76
- Figure 29. Critical breakage energy,  $E_c$ , as a function of particle diameters for (a) Q-ROK sand and (b) glass beads with the performance of four combinations of contact models and fracture models. The trend lines are predicted on the basis of calibrated particle-scale models (Figure 27) and averaged values of the scaling factor  $\zeta$  in Eq. (4.7) ( $\zeta = 0.35$  for glass beads and  $\zeta = 0.21$  for Q-ROK sands) ..... 79
- Figure 30. Average particle size and macroscopic yield stresses relationship of (a) Q-ROK sands; and (b) glass beads with the assessment of the performance of two considered fracture models ..... 79
- Figure 31. Illustration of the determination of the current breakage value,  $B$  for Q-ROK#4 sand at 20 MPa stress ..... 80
- Figure 32. Evolution of  $B$  measured in the experiments (symbols) and computed through model data simulations (lines) for (a) Q-ROK sands and (b) glass beads ..... 82
- Figure 33 Schematics of (a-c) delayed fracture in brittle systems and (d-f) delayed breakage in a granular continuum; (a) typical configuration of deep-notch bending tests; (b) example of single particle crushing test; (c) propagation of pre-existing crack; (d) example of oedometric creep test; (e) creep deformation due to delayed breakage; (f) evolution of particle gradation– the percent of fine fragments increases with time. .... 86
- Figure 34 Schematic of breakage initiation in the p-q plane. Point A indicates the first violation of the yield criterion (i.e.,  $y = 0$ ). The difference between B and C indicates the initial

|                                                                                                                                                                                                                                                                                                                                                                                                                                                      |     |
|------------------------------------------------------------------------------------------------------------------------------------------------------------------------------------------------------------------------------------------------------------------------------------------------------------------------------------------------------------------------------------------------------------------------------------------------------|-----|
| overstress at the onset of creep (C indicates the stress state at the onset of creep, while B marks the position of the yield surface at that same state). Dashed lines indicate gradual growth of the yield surface due to elastic hardening (i.e., delayed particle fragmentation leading to higher comminution resistance), which stops when the surface reaches point C (i.e., when both breakage growth rate and creep strain rate vanish)..... | 91  |
| Figure 35. 24-hour creep compression for (a) Q-ROK#1, (b) Q-ROK#2, (c) Q-ROK#4, and (d) Ottawa sands at various stress levels. Open symbols indicate the initial state prior to creep. Closed symbols indicate the end of the creep test. ....                                                                                                                                                                                                       | 92  |
| Figure 36 Graphical representation of delayed breakage growth. The shaded area represents the breakage cumulated over time. ....                                                                                                                                                                                                                                                                                                                     | 93  |
| Figure 37 GSD curves measured through sieving after 24-hour creep tests at different stress levels (a) Q-ROK#1 (b) Q-ROK#2 (c) Q-ROK#4 and (d) Ottawa sands. ....                                                                                                                                                                                                                                                                                    | 94  |
| Figure 38 Evolution of breakage during creep tests at selected normalized stress levels .....                                                                                                                                                                                                                                                                                                                                                        | 95  |
| Figure 39 Plot of the breakage growth rate against the breakage overstress function for all tested sands for estimation of stress corrosion index, $n$ . It is found that the measurements are satisfactorily fitted by the typical range of stress corrosion index reported in the literature for quartz (i.e., $15 \leq n \leq 60$ ).....                                                                                                          | 97  |
| Figure 40 Parametric study assessing the grainsize dependence of the model parameters $\dot{B}_0$ and $n$ .....                                                                                                                                                                                                                                                                                                                                      | 99  |
| Figure 41. Measurement of 24-hour creep at various stresses with the breakage model simulations for (a) Q-ROK#1, (b) Q-ROK#2, (c) Q-ROK#4 and (d) Ottawa sand .....                                                                                                                                                                                                                                                                                  | 101 |

|                                                                                                                                                                                                                                                                            |     |
|----------------------------------------------------------------------------------------------------------------------------------------------------------------------------------------------------------------------------------------------------------------------------|-----|
| Figure 42 Measurements of 24-hour creep strains (symbols) and corresponding model simulations (lines): (a) Q-ROK#1, (b) Q-ROK#2, (c) Q-ROK#4 and (d) Ottawa sands.....                                                                                                     | 102 |
| Figure 43 Measurements of the breakage value for 24-hour creep at $\sigma/\sigma_{yield} = 1.33$ and 2.73 (symbols) along with the VBM simulations (lines): (a) Q-ROK#1, (b) Q-ROK#2, (c) Q-ROK#4, and (d) Ottawa sand.....                                                | 103 |
| Figure 44 Evolution of particle gradation at 24-hour creep compressions (symbols) with the breakage model simulations (lines): (a) Q-ROK#1, (b) Q-ROK#2 (c) Q-ROK#4 and (d) Ottawa sands .....                                                                             | 104 |
| Figure 45 Measurements of the size-dependent reference breakage rate and characteristic breakage time .....                                                                                                                                                                | 106 |
| Figure 46. Illustration of logarithmic delayed deformation coefficients $\lambda_B$ and $\lambda_\epsilon$ extracted from $B$ -time and $\epsilon$ -time plots. These factors quantify the rates of delayed breakage growth and creep strain over time, respectively ..... | 107 |
| Figure 47. Comparison of the rate of creep accumulation with respect to the rate of breakage growth for all Q-ROK sands at $\sigma/\sigma_y = 1.33$ and 2.73, exhibiting their linear size-sensitive characteristics.....                                                  | 108 |
| Figure 48. X-ray microtomography setup at GSECARS 13-BM-D, APS, Argonne National Laboratory.....                                                                                                                                                                           | 114 |
| Figure 49. SMT scans performed at selected stress states during oedometer tests on Q-ROK#2 and Ottawa sands .....                                                                                                                                                          | 115 |
| Figure 50. X-ray microtomography setup at DNDCAT 5-BM-C of the APS, Argonne National Laboratory.....                                                                                                                                                                       | 116 |

- Figure 51. 24-hour oedometric creep compression curves for Q-ROK#1, #2, #4 sands and Ottawa sand ..... 117
- Figure 52. Example of post-processing a reconstructed X-ray microtomography image via Aivzo: (a) filtering; (b) thresholding and separation; (c) labeling of Ottawa sand..... 118
- Figure 53. Grain size distribution (GSD) curves at preloading ( $\sigma_v = 0\text{MPa}$ ) and final loading ( $\sigma_v = 80\text{MPa}$ ) during the oedometric compression tests obtained through sieve analyses (symbol) and tomography image analyses (lines) techniques ..... 119
- Figure 54. Evolution of the average 3D shape parameters of the tested sands during oedometric compression. .... 121
- Figure 55. Grayscale vertical cross-sections (top row) from 3D SMT images of Q-ROK#2 sand with 3D renderings (bottom row) exhibiting shape-dependency of local grain failure (i.e., initially angular particles were broken into multiple fragments at the onset of crushing due to surface fracture) ..... 122
- Figure 56. Grayscale vertical cross-sections (top row) from 3D SMT images of Ottawa sand with 3D renderings (bottom row), exhibiting shape-dependency of local grain failure (i.e., initially rounded particles tend to split into two at the onset of crushing and then crumble at higher pressures) ..... 123
- Figure 57. Evolution of GSD curves for (a) Q-ROK#2 and (b) Ottawa sands during oedometric compression, exhibiting progressive growth of finer materials with an increase of loading ..... 125
- Figure 58. Evolution of (a) the breakage index  $B$  and (b) the percent of fragmented particles for Q-ROK#2 and Ottawa sands. The figures display a more marked growth of breakage index  $B$ , and percent of crushed particles for Ottawa sand..... 125

|                                                                                                                                                                                                                                                                                                                             |     |
|-----------------------------------------------------------------------------------------------------------------------------------------------------------------------------------------------------------------------------------------------------------------------------------------------------------------------------|-----|
| Figure 59. Evolution of (a)-(b) average fracture mode indices for individual particles.....                                                                                                                                                                                                                                 | 127 |
| Figure 60. Statistical distribution of particle-specific cumulative fracture index, $\alpha_f$ at $\sigma/\sigma_y = 0.50$ ,<br>1.00, 1.33, 1.66 and 2.00.....                                                                                                                                                              | 128 |
| Figure 61. Statistical distribution of particle-specific incremental fracture index, $\beta_f$ at $\sigma/\sigma_y = 0.50$ ,<br>1.00, 1.33, 1.66 and 2.00.....                                                                                                                                                              | 129 |
| Figure 62 micro-macro comparison for (a) the yield stresses and (b) the compression indices of Q-<br>ROK#2 and Ottawa sand .....                                                                                                                                                                                            | 130 |
| Figure 63. 24-hour creep strains for Q-ROK#1, #2, #4 and Ottawa sands at $\sigma/\sigma_y = 1.33$ , showing<br>that the rate of creep deformation is size- and shape-dependent (i.e., the rate of creep<br>deformation is expected to become higher with an increase of particle size or initially<br>rounded grains) ..... | 131 |
| Figure 64. Evolution of GSD curves for (a) Q-ROK#1, (b) Q-ROK#2, (c) Q-ROK#4 and (d)<br>Ottawa sands over 24-hour creep compressions at $\sigma/\sigma_y = 1.33$ .....                                                                                                                                                      | 132 |
| Figure 65. Evolution of delayed breakage values for (a) Q-ROK#1, (b) Q-ROK#2, (c) Q-ROK#4<br>and (d) Ottawa sands over 24-hour creep at $\sigma/\sigma_y = 1.33$ , exhibiting higher breakage growth<br>rate for larger grains or rounded particles.....                                                                    | 133 |
| Figure 66. Grayscale vertical cross-sections from 3D SMT images of angular Q-ROK#1 (Top row),<br>Q-ROK#2 (middle row) and Q-ROK#4 (bottom row) sands exhibiting subcritical crack<br>propagation over 24-hour creep at $\sigma/\sigma_y = 1.33$ .....                                                                       | 134 |
| Figure 67. Grayscale vertical cross-sections from 3D SMT images of round Ottawa sand exhibiting<br>subcritical crack propagation over 24-hour creep at $\sigma/\sigma_y = 1.33$ .....                                                                                                                                       | 135 |

|                                                                                                                                                                                                                                                                                                                                                                 |     |
|-----------------------------------------------------------------------------------------------------------------------------------------------------------------------------------------------------------------------------------------------------------------------------------------------------------------------------------------------------------------|-----|
| Figure 68 Alteration of the average 3D shape parameters of Q-ROK#2 and Ottawa sands during 24-hour creep ( $\sigma/\sigma_y = 1.33$ ) .....                                                                                                                                                                                                                     | 135 |
| Figure 69. Relationship between the rate of creep strain and delayed breakage growth for Q-ROK sands during 24-hour microscopic creep experiments (i.e., the use of a miniaturized apparatus) at $\sigma/\sigma_y = 1.33$ .....                                                                                                                                 | 136 |
| Figure 70. Micro-macro comparison for (a) the rate of creep strain and (b) delayed breakage growth rate during 24-hour creep measurements at $\sigma/\sigma_y = 1.33$ .....                                                                                                                                                                                     | 137 |
| Figure 71. Initial configuration of single particle and particle replacement configuration, illustrating that an initial particle is broken and replaced by 20 new fragments arranged through an Apollonian packing.....                                                                                                                                        | 144 |
| Figure 72. DEM simulation of force-displacement behavior of single particle using the stress-based failure criteria with Hertzian contact model .....                                                                                                                                                                                                           | 145 |
| Figure 73. Example of a virtual DEM particle after a diametral compression simulation .....                                                                                                                                                                                                                                                                     | 146 |
| Figure 74. A virtual DEM specimen composed of monodisperse particles ( $d = 670$ micron) prior to an oedometric compression simulation. The color reflects the particle size. ....                                                                                                                                                                              | 147 |
| Figure 75. (a) stress-strain behavior of the DEM specimen for oedometric compression, and (b) the GSD evolution for the same virtual simulation based on the Hertzian contact law and surface crack mode .....                                                                                                                                                  | 149 |
| Figure 76. (left): A virtual DEM specimen made of initially uniform particle size ( $d = 670$ micron) after the oedometric compression simulation. The color reflects the particle size in radius. (Right): The force chain of inter-particle contacts after the completion of loading. The color reflects the magnitude of inter-particle contact forces ..... | 149 |

- Figure 77. Result of 3D DEM simulation (symbols) for single particle under static fatigue plotted with the trendline of the crack propagation (line). The crack growth progressively continued until a sudden increase of the crack length at which the particle completely fractured. .... 151
- Figure 78. (left) Macroscopic creep stress-strain response and (right) accumulation of creep strain of the virtual DEM specimen using the particle-scale subcritical crack theory ..... 153
- Figure 79. A virtual DEM specimen after creep compression simulation which initially composed of monodisperse particles ( $d = 670$  micron) including uniform crack sizes. (a)-(b) an indicator of crack growth sign, signaling the crack growth if the color of particle is green at pre-creep and post-creep, respectively; (c)-(d) crack size of individual grains in *meters* at pre-creep and post-creep, respectively..... 154

## LIST OF TABLES

|                                                                                                                                        |     |
|----------------------------------------------------------------------------------------------------------------------------------------|-----|
| Table 1. Summary of physical and index properties, and mineralogical characteristics for testing granular materials in this study..... | 50  |
| Table 2. Summary of the minimum, maximum and average values of circularity and roundness measurements.....                             | 51  |
| Table 3. Summary of averaged values of calibrated contact model parameters and fracture model parameters.....                          | 72  |
| Table 4. Summary of the calibrated parameters used for the simulations based on the breakage mechanics model.....                      | 80  |
| Table 5 Summary of the viscous breakage model parameters.....                                                                          | 104 |
| Table 6. Summary of DEM model parameters for simulating single particle crushing .....                                                 | 146 |
| Table 7. Summary of DEM model parameters for simulating oedometric compression .....                                                   | 148 |
| Table 8. Summary of DEM model parameters for simulating subcritical crack propagation of single particle.....                          | 152 |

## CHAPTER 1: INTRODUCTION

Granular materials are widely studied in disparate fields of science and technology. Understanding their fundamental properties is therefore crucial for a range of applications, from the exploitation of natural resources, to engineering design and public safety. One of the challenges concerning the mechanics of particulate granular geomaterials is their response to the high pressures acting in the ground. Since grain crushing under high confinement is an area of interest for engineers and geoscientists, numerous studies have been performed to the crushability of granular materials. For example, the behavior of sand and rockfill (often controlled by the mechanics of brittle particles) has gained attention in applications such as dam engineering and pile bearing capacity (Nakata et al., 2001b). Early empirical and analytical models describe such crushable systems in terms of either microscale (e.g., particle-scale) or macroscale response (e.g., assembly-scale). For instance, Lade et al. (1996) and Shahnazari and Rezvani (2013) have examined the correlation between energy input and degree of comminution, providing a unique relation between particle breakage and energy supply per unit volume. Miura and O-Hara (1979) and Ovalle et al. (2013) suggest that the increase of surface area (e.g., another indicator of the extent of grain crushing) exhibits close correlation with the plastic work done on the specimen during compression paths. However, these studies are performed in terms of macroscopic quantities defined at the assembly scale, implying that there is a limited connection between the macroscopic soil response and the properties of the constituting grains.

A notable exception to explore the multi-scale dependencies of crushing processes is the breakage mechanics framework (Einav, 2007a, Einav, 2007b) which enables the thermodynamics interpretation of the compression behavior of granular media subjected to high confining stresses.

This framework establishes yield criteria and evolution laws based on an energy measure analogous to the energy release rate for fracture processes, thus providing a pathway to link energy input, degree of comminution and stress-strain responses.

The recent study by Zhang et al. (2016) has further established a link between fracture properties of individual particles and macroscopic breakage by using a number of analytical models, thus providing new tools to explore the multi-scale implications of varying size, shape and mineralogy of the constituting grains. This link is a good starting point to study the time-dependent grain crushability at high pressures. In fact, creep experiments performed by Karimpour and Lade (2013) on dense sand specimens subjected to triaxial conditions, found that the accumulation of creep strain increases with the confining pressure. Although this study suggested that grain fracture was the main factor responsible for the rearrangement of microstructure over time, all measurements were conducted at the assembly-scale, thus hindering the direct assessment of the time-dependent mechanical response at the grain-scale.

Oldecop and Alonso (2007) advocated stress corrosion mechanisms (inspired by delayed fracture of ceramics) to examine the phenomenon of crack growth in rockfill element at macroscale. This study enabled us to compute the time to failure of an individual particle subjected to diametral compression by knowing the fracture properties of constituting minerals. However, it established only a qualitative link between delayed grain fracture and continuum modeling of the soil response, in that the modeling approach used to reproduce macroscopic creep was based on a visco-plastic adaptations of critical state theories which bear no connection to the physics of particle fracture. These considerations constitute one of the motivations for this study.

The main objective of this thesis is to improve our understanding of the mechanics of grain crushing at multiple length scales by exploring the role of grain size and shape, as well as how

they affect the collective behavior of granular soil samples. Different shapes of granular materials with various particle size ranges will be considered to conduct particle-scale and sample-scale experiments under the quasi-static loading regimes and high pressures (i.e., stresses sufficiently high to cause pervasive grain crushing). The continuum breakage mechanics theory (Einav, 2007a) and multi-scale fracture models (Zhang et al., 2016) will be used to guide the experimental measurements. Furthermore, a fundamental understanding of the time-dependent physics of delayed fracture of granular materials will be assessed through a macroscale experimental program, as well as in light of a rate-dependent breakage mechanics constitutive framework. To achieve a comprehensive understanding of the connection between the particle-scale and the assembly-scale behavior, the thesis will benefit from advanced experimental techniques such as synchrotron X-ray microtomography (SMT) and digital image analyses, as well as from computational analyses based on the Discrete Element Method (DEM), thus providing tools to incorporate the understanding of the role of particle-scale attributes on the collective breakage behavior through both discrete and continuum models. In summary, the following aspects are the objectives of this study:

1. The rate-independent characterization of crushable granular soils with different attributes (i.e., size and shape) will be assessed through a systematic experimental program and continuum breakage model simulations.
2. The time-dependent characterization of crushable granular soils will be examined through creep experiments along with viscous breakage model simulations
3. X-ray microtomography imaging will be performed to evaluate the mechanical response and local failure mechanism of granular geomaterials, with the goal to corroborate the model hypotheses through direct visualization.

4. The computational (or virtual) assessment of particle interactions will be conducted via DEM simulations to understand the role of internal microstructure on the continuum stress-strain behavior of the granular system at high vertical stresses.

The thesis is organized as follows: Chapter 2 discusses the state of the art about the laboratory experiments to assess the particle-scale fracture and assembly-scale comminution in granular materials. In addition, the theoretical backgrounds regarding fracture mechanics, continuum breakage mechanics, subcritical crack growth theory, and delayed breakage mechanics are briefly introduced. Chapter 3 provides the details of testing materials and methodology of laboratory equipment being used for this study. The particle-scale attributes and index properties of all tested materials will be described. Moreover, the micro- and macro-scale laboratory experimental technique and procedure will be discussed in detail. Chapter 4 reports the assessment of compression and crushing behaviors of granular materials (i.e., having different particle size and shape) through laboratory tests. At particle-scale, single particle crushing tests will be performed via a specially designed test cell enabling diametral particle compression. At sample-scale, an oedometer test will be carried out by using a one-dimensional consolidation apparatus. Additionally, the experimental observations will be simulated within the continuum breakage mechanics framework, establishing the macroscopic yielding criteria as well as evolution laws based on an energy measure analogous to the energy release rate for fracture processes, thus providing a pathway to link energy input, degree of comminution and stress-strain responses.

Chapter 5 presents time-dependent laboratory experiments at high vertical pressures. Oedometric creep tests will be performed on natural silica quartz sands. The evolution law recently proposed by Zhang and Buscarnera (2017) to incorporate subcritical crack growth and nonlinear energy

dissipation into a rate-dependent breakage model will be used as a reference to interpret the measurements. Chapter 6 presents microscopic replicas of the macroscale experiments based on the synchrotron X-ray microtomography (SMT) performed at Argonne National Laboratory in Lemont, Illinois, USA, with the purpose of directly measuring the deformation behavior and microstructure evolution. Chapter 7 presents a computational assessment of crushing behavior in granular materials via DEM simulations. Both particle-scale and sample-scale crushing behaviors will be modeled to show the capabilities of discrete simulations for geomechanical applications. Finally, Chapter 8 highlights and summarizes the key findings of the thesis and suggests possible directions for the future work.

## CHAPTER 2: PREVIOUS STUDIES AND BACKGROUND

### 2.1 Mechanical Behavior of Crushable Soils

Numerous works have shown that the rate-independent crushing behavior of soils is controlled by various components (i.e., grain size, mineralogical compositions, and shape). Nakata et al. (2001b) carried out single particle crushing tests and measured the statistical characteristics of crushing processes in relation with the Weibull survival probability of individual grains. Their findings suggest that (i) a particle characteristic stress (or tensile strength) can be defined as the first peak in the force-displacement curve; (ii) From the Weibull statistics, a characteristic stress can be defined as to measure the characteristic strength at which particles have 37% probability of survival (Figure 1); (iii) the Weibull modulus,  $w_m$ , represents the variability in strength of the particles, with smaller values of  $w_m$  corresponding to large variability in strength of the particles; (iv) the amount of crushing can be measured by the evolution of the grain size distribution (GSD) curves (Figure 1); and (v) the yielding surface is associated with the amount of particle breakage.

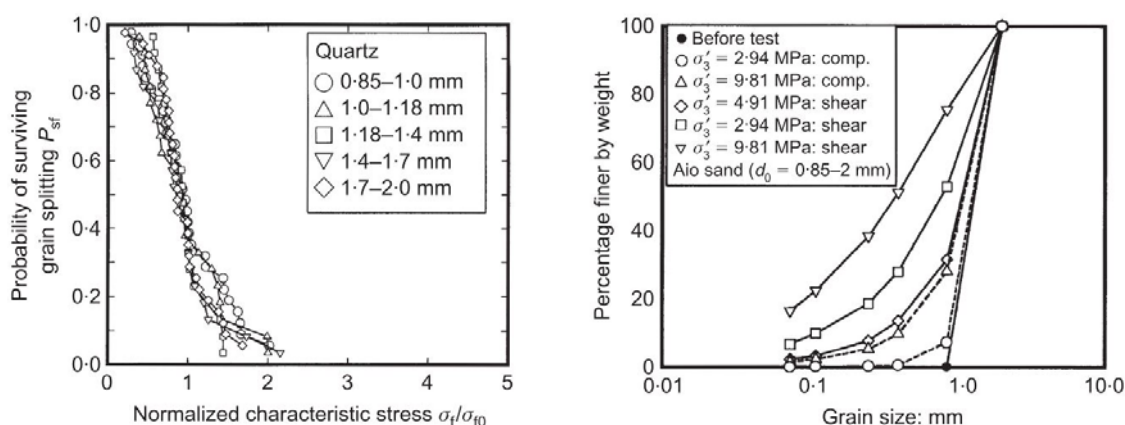


Figure 1. (left): Normalized survival probability curves of quartz sand at failure, and (right): Grain size distribution curves before and after loading (Nakata et al., 2001b)

McDowell (2002) performed diametral compression tests and one-dimensional compression tests with a wide range of particle sizes of silica sands, and yet having similar shape. This study shows that (i) the yielding stress is proportional to the tensile strength of single particles and is found to increase with decreasing grain size (Figure 2); (ii) the GSD curves evolve as the applied stresses progressively increase. Nevertheless, several open questions remained: (i) How does the local fracture mechanism affect macroscopic mechanical properties such as a yielding strength? (ii) How do these mechanisms depend on the shape of grains? (iii) Do the mechanisms of local grain fracture change when the particles are crushed within a soil assembly?

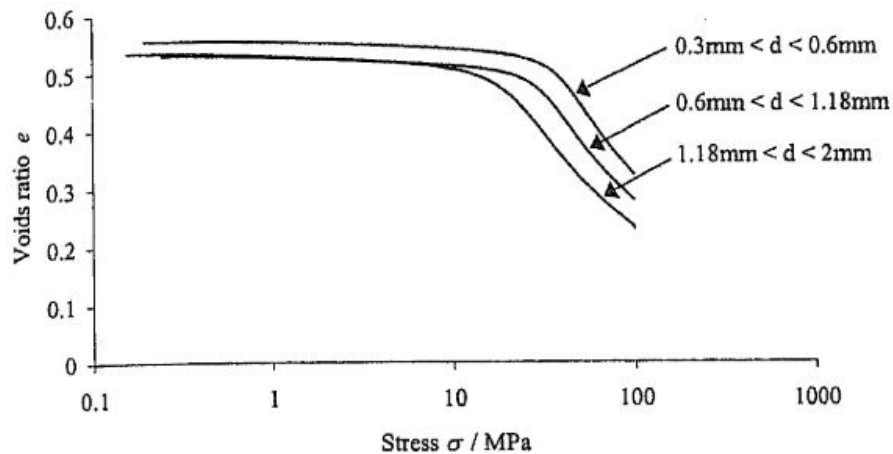


Figure 2. One-dimensional compression plots for three different size ranges of sand (McDowell, 2002)

### 2.1.1 Particle fracture models

The failure of an individual grain can be quantified by the characteristic strength,  $\sigma_{pc}$  that can be measured through diametral compression of single particle between two rigid platens (Jaeger, 1967)

$$\sigma_{pc} = \frac{F_f}{d_p^2} \quad (2.1)$$

where  $F_f$  is the maximum force that determines a failure of the particle, while  $d_p$  is a particle diameter. Alternatively, an energy measure,  $E_{pc}$  (volume specific fracture energy) can be computed by integrating the force-displacement relationship up to the major failure force in order to describe the resistance of particle against breakage.

$$E_{pc} = \frac{1}{V_p} \int F_f d\Delta \quad (2.2)$$

where  $V_p$  is the particle volume, and  $\Delta$  is the axial displacement. Experimental and numerical studies have shown that individual particles can exhibit two types of fracture modes under the diametral loading: The evolution of crack propagation initiates either at particle contacts (Hiramatsu and Oka, 1966) or at the center of the grain (Shipway and Hutchings, 1993). Tapias et al. (2015) suggest that the center crack mode is associated with the high stress level (e.g., the applied stress is typically greater than the yield stress), whereas the surface crack is triggered by small contact forces upon diametral loading. Zhang et al. (2016) derived analytical solutions of failure load  $F_f$ , as well as fracture energy,  $E_{pc}$ , describing both failure modes as a function of particle size, shape and mineralogy. This study suggested that the analytical expressions based on the linear elastic fracture mechanics enable to distinctly capture two failure modes on a double-logarithmic  $\sigma_{pc}$ - $d_p$  plane where negative slopes of 0.5 and 1.5 are expected for central crack and surface failure modes, respectively (Figure 3).

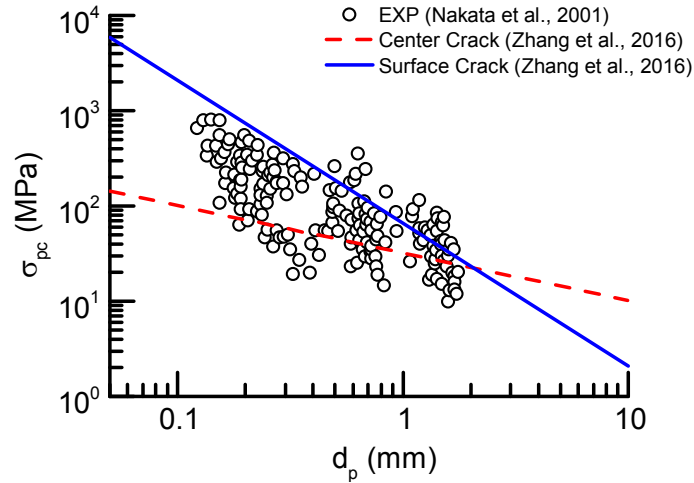


Figure 3. Prediction of failure mechanism for silica sands (data from Nakata et al. (2001b)) with various grain size ranges (Zhang et al., 2016)

On the other hand, a  $E_{pc}-\sigma_{pc}$  relation is used to describe the properties of contact elasticity (e.g., linear, Hertzian and conical contacts) because fracture energy is computed by integration of the contact response up to failure (Figure 4a). Moreover, the  $E_{pc}-d_p$  relation is influenced by both failure mode and contact law, and hence resulting in a wide range of size effects (Figure 4b).

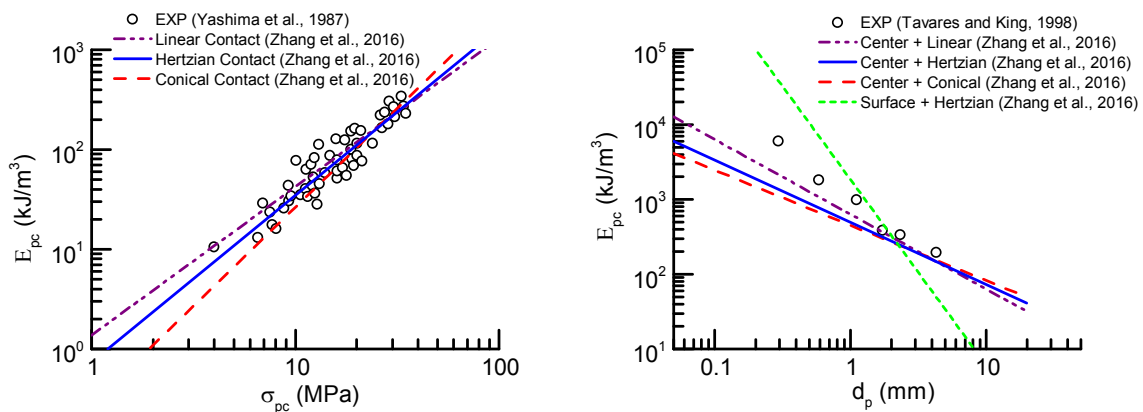


Figure 4. (a) Analytical solutions of  $E_{pc}-\sigma_{pc}$  relationship for contact law exhibiting the linear (or flat), Hertzian and conical contact models correspond to slopes of 2.0, 1.66 and 1.5; (b) predictions of the combinations of failure modes and contact laws (Zhang et al., 2016)

### 2.1.2 Continuum breakage mechanics theory

The breakage mechanics theory proposed by Einav (2007a) postulates that the yielding of sands at high pressure is a consequence of grain crushing. The theory is an important tool to understand collective interactions in granular materials, such as the dynamics of force chains (Zhao and Song, 2015) and energy redistribution caused by particle breakage (Nguyen and Einav, 2009, Russell and Einav, 2013). The breakage mechanics enables to interpret the evolution of the GSD of a granular material by postulating that the macroscopic yielding occurs when the breakage energy reaches a critical threshold,  $E_c$ . The yielding condition considering both breakage and frictional dissipation can be expressed as follows:

$$\frac{E_B}{E_c}(1-B)^2 + \left(\frac{q}{Mp}\right)^2 \leq 1 \quad (2.3)$$

where  $E_B = -\frac{\partial\Psi}{\partial B}$  is the breakage energy;  $\Psi$  is the elastic strain energy;  $E_c$  is the critical breakage energy; and  $B$  is the breakage index, indicating the amount of fragmentation within the representative elementary volume (REV) (e.g., spanning from zero to unity, implying no breakage and complete breakage, respectively). From the continuum modeling standpoint, the use of energy principles to define yielding (e.g., critical breakage energy,  $E_c$ ) bears similarity with the Griffith fracture theory, where the energy release rate reaches a critical energy release rate,  $G_{IC}$ , at the onset of fracture. Individual grain crushability impacts collective particle properties of granular materials, such as yield stress, inelastic compressibility and frictional resistance (McDowell and Bolton, 1998, Coop et al., 2004, Brzesowsky et al., 2014, Zhang et al., 2016). Considering the links between

local energy threshold  $E_{pc}$  at the particle scale and the REV yielding threshold  $E_c$ , Zhang et al. (2016) proposed the following simple energy-based scaling relation:

$$E_c = \xi(1 - n)E_{pc} \quad (2.4)$$

where  $n$  is the porosity of the assembly, and  $\xi$  is the scaling factor. Such scaling law has been indirectly validated with several datasets on quartz sands reported in the literature (Zhang et al., 2016), finding that an approximated scaling factor of 0.25 provides a satisfactory agreement with experimental results reported by Nakata et al. (2001b) and McDowell (2002). More recently, Cil and Buscarnera (2016) conducted DEM simulations to quantify the range of values viable for the scaling factor  $\xi$ , obtaining values between 0.15 and 0.43 for a range of deterministic and probabilistic fracture models. Their findings indicate that (i) the use of constant value of  $\xi$  is valid if the fracture mode (e.g., center crack or surface crack) is fixed for all particles, and that (ii) the simulation confirms that the existence of the same size-dependent trends both at particle and assembly scales, implying that  $\xi$  can be dependent of particle size, shape and mineralogy. Nevertheless, since no experimental data are currently available to test the abovementioned results explicitly, this research aims to select particles of different size and shape to provide experimental verification of the model hypotheses.

## 2.2 Delayed Particle Crushing

### 2.2.1 Subcritical crack growth theory

Creep is a deformation process that occurs over time under constant loading. Numerous works have suggested different mechanisms to describe the change of the creep rate with time. Kwok and

Bolton (2013) suggested that creep in granular soils at high stresses is associated with grain crushing and consequent particle rearrangement. Takei et al. (2001) conducted oedometric creep compression tests on crushable materials, showing that the time-dependent response of sands is due to repetitive crushing and redistribution of contact properties. In earlier studies, Wiederhorn et al. (1980) and Freiman (1984) adopted the delayed fracture theories originally conceived for ceramics with the stress corrosion cracking (i.e., crack starts to grow at a specific velocity given by a rate of chemical reaction at the crack tip under the collective performances of the applied stress and fluid). Their findings suggest that the growth of microcracks in ceramics can be determined by the tensile stress at the crack tip. McDowell and Khan (2003) used a similar concept of time-dependent strength in order to propose an analytical model, hypothesizing that (i) particle fracture is associated with soil compression and that (ii) creep at constant loading is caused by the slow decrease of particle strength with time. A more physical connection with the physics of grain fracture was established by Oldecop and Alonso (2007), who also used the concept of crack propagation to study the progressive settlement of rockfill. A simple mathematical expression proposed by Charles (1958) is in fact to model the phenomenon of delayed particle fracture at particle-scale in light of subcritical crack growth:

$$\dot{i} = \dot{i}_0 \left( \frac{K_I}{K_{I,ref}} \right)^n \quad (2.5)$$

where  $n$  is the subcritical exponent (e.g., a constant that controls crack growth rate, ranging from 15 to 60 for quartz minerals),  $K_I$  is the stress intensity factor,  $K_{I,ref}$  is the normalizing stress intensity factor (i.e., it can be either critical fracture toughness under vacuum condition,  $K_{IC}$  or the minimum stress intensity factor for fracture growth under the considered environmental condition,  $K_{I0}$ ), and

$\dot{l}_0$  is the rate of reference crack propagation. The main shortcoming of Eq. (2.5) is that, while being inspired by fracture kinetics theories, it implies that fractures grow regardless of the magnitude of the tensile stress acting locally (i.e., they imply no threshold). An alternative that is compatible with existence of an energy threshold for fracture (Griffith, 1921) has been proposed by Maugis (1985), who suggested an analytical expression including a stress corrosion limit (e.g.,  $\dot{l} > 0$ ), as well as parameters of the Charles model to describe the subcritical crack growth:

$$\dot{l} = \dot{l}_0 \left\langle \frac{K_I^2}{K_{I0}^2} - 1 \right\rangle^{n/2} = \dot{l}_0 \left\langle \frac{G_I}{2\gamma} - 1 \right\rangle^{n/2} \quad (2.6)$$

where  $G_I$  is the strain energy release rate,  $\gamma$  is the intrinsic surface energy (e.g., associated with the onset of crack propagation under the given environmental condition). This formulation is useful to model more accurately the time of failure (Figure 5). As a result, it provides a more convenient platform to simulate, in a physically-consistent manner, the delayed accumulation of breakage in granular soil samples within both a DEM context and a continuum modeling context.

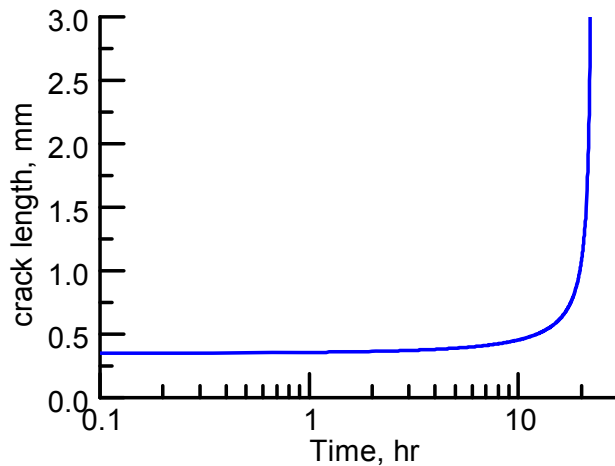


Figure 5. Example of model predictions on the propagation of crack length

### 2.2.2 Viscous breakage mechanics theory

When an assembly composed of sand particles is subjected to a constant loading (e.g., creep test), individual particles aligned along the major force chains can be fractured if the applied stress is sufficiently high. This event is reflected macroscopically by inelastic strains developed over time. A stable equilibrium condition can be achieved where the limited strain accumulation is collected over time. It is known that the energy dissipation caused by macroscopic crushing includes the dissipation associated with (i) the creation of new surface area, (ii) the energy redistribution, and (iii) additional net energy dissipation caused by delayed inelastic interactions at crack tips. Time-independent dissipation rate functions can be defined as follows (Zhang and Buscarnera, 2017):

$$\Phi(B, \dot{B}) = \frac{E_c}{(1-B)^2} \dot{B} + \phi_B(\dot{B}) \geq 0 \quad (2.7)$$

where  $\dot{B}$  is an incremental breakage index, and  $\phi_B$  is an additional energy dissipation term due to delayed breakage. In order to make the above relation time-dependent, Zhang and Buscarnera (2017) derived a breakage evolution law based on a dissipation potential characterized by a similar mathematical form to the dissipation potential of Maugis crack growth law. This led to a breakage kinetics relation that can be expressed as follows:

$$\dot{B} = \dot{B}_0 \xi_B^{n/2} \quad (2.8)$$

where

$$\xi_B(E_B, p, q) = \left\langle \frac{(1-B)^2 E_B}{E_c} + \left( \frac{q}{Mp} \right)^2 - 1 \right\rangle \quad (2.9)$$

While convenient from a modeling standpoint and capable of replicating macroscopic evidence of creep in crushable soils, the equations above have not yet been validated through dedicated experiments conducted at both particle and assembly scales. As a result, numerous open questions remain, such as: (i) Can the same stress corrosion coefficient,  $n$  used for particle-scale crack growth be used to describe the nonlinear rate-dependence of breakage growth? (ii) What is the effect of particle attributes on the characteristic time of grain breakage (i.e.,  $t_B = 1 / \dot{B}_0$ )? This research will address these questions, with the goal to provide experimental and computational validation of the model hypotheses detailed above.

### **2.3 X-ray Microtomography Imaging**

X-ray microtomography has been widely used in geomechanics to examine the microstructure of geomaterials. In the early study, Desrues et al. (1996) and Alshibli et al. (2000) first used the X-ray tomography technique to track strain localizations under the triaxial compression, thus demonstrating that imaging can be useful for quantitative analyses of the volume change and direct assessment of the mode of strain localization. However, these studies relied on a coarse spatial resolution (i.e., the given pixel size was nearly hundreds of microns), and hence the characterization of grain-scale properties and attributes was not possible. Recently, as shown in Figure 6 and Figure 7, high-resolution tomographic imaging has enabled the study of particle- and specimen-scale micro-mechanical interactions, as well as fracture mechanism under load (Andò et al., 2012, Hall et al., 2010, Fonseca et al., 2012, Cil and Alshibli, 2014, Zhao et al., 2015, Karatza et al., 2018). Synchrotron radiation is accessible at the Advanced Photon Source (APS), Argonne National Laboratory, Lemont in Illinois, USA, and it provides X-ray imaging capabilities down to few microns spatial resolution within a reasonable data collection time (Rivers et al., 2010).

Therefore, for this project, Synchrotron X-ray microtomography (SMT) imaging will be used to corroborate the experimental and numerical findings. The methodology and technique of SMT will be further discussed in greater detail in chapter 6.

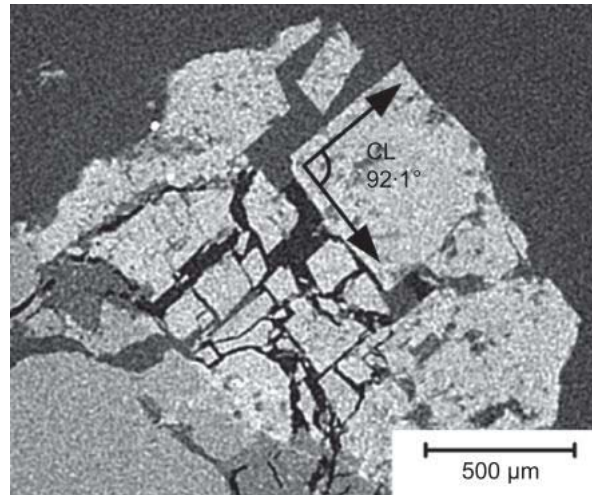


Figure 6. 2D grey-scale image of single particle used for quantitative analysis on fracture patterns (Zhao et al., 2015)

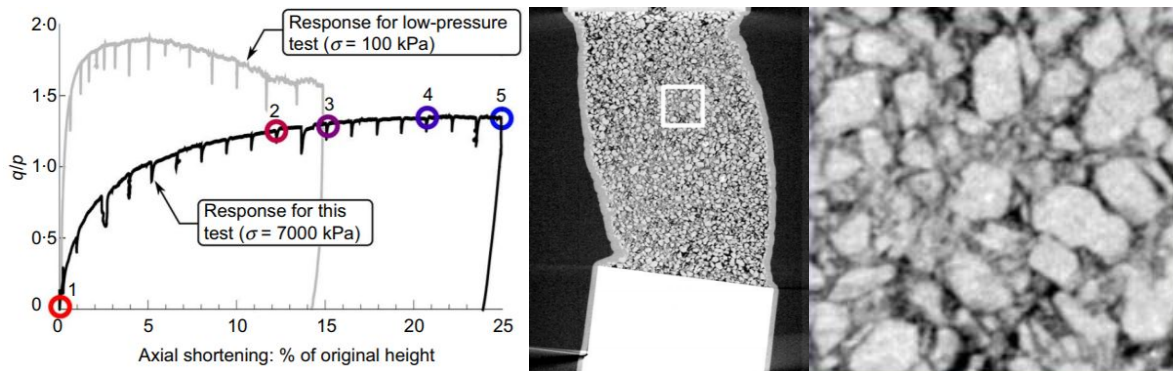


Figure 7. Direct visualization of local grain failure during triaxial compression test on Hostun sand (Andò et al., 2013).

## 2.4 Discrete Element Modeling Analyses

The discrete element method (DEM) has been first introduced in geomechanics by Cundall and Strack (1979). Since then, many authors have been involved in the modeling of particle fracture

phenomena through DEM (ARROYO et al., 2011, McDowell and de Bono, 2013, Jiang et al., 2015, Falagush et al., 2015, Cil and Alshibli, 2015, Cil and Buscarnera, 2016), mostly because of its ability to compute particle-to-particle contact forces and individual grain positions. Cil and Alshibli (2015) performed 3D DEM simulation of oedometric compression to investigate the role of agglomerate shape, as well as the size distribution of spherical subparticles (i.e., the units which constitute a particle agglomerate) on the crushing response. This study suggests that the determination of grain size and number of subparticles controls the shape of the agglomerates which consequently affects the contact properties as well as failure mode (Figure 8). Furthermore, Tapias et al. (2015) conducted 3D DEM analyses of both 1D compression, as well as triaxial compression tests to qualitatively investigate the failure response of rockfill aggregates, adapting the particle substitution technique (i.e., at the onset of breakage the original microsphere is replaced by a number of smaller spherical elementary particles). The authors also implemented a virtual crack length  $a = a_0 + v \times \Delta t$  and its velocity of propagation  $v = v_0 \times \left( \frac{K_I}{K_{IC}} \right)^n$  in each particle, in accordance with previous propositions by Oldecop and Alonso (2007). Figure 9 presents examples of a DEM simulation of stress-strain response, as well as volumetric change upon triaxial compression loading, showing the possibility to capture the macroscopic trends of behavior by benefiting from data about particle strength characteristics. Therefore, in this study, the DEM technique will be used as a virtual laboratory tool to predict the mechanical responses at particle- and assembly-scale compression tests. In addition, subcritical crack growth theory will be implemented in the model simulations to predict the time of failure of grains susceptible to static fatigue, as well as the accumulation of creep strains at specimen-scale.

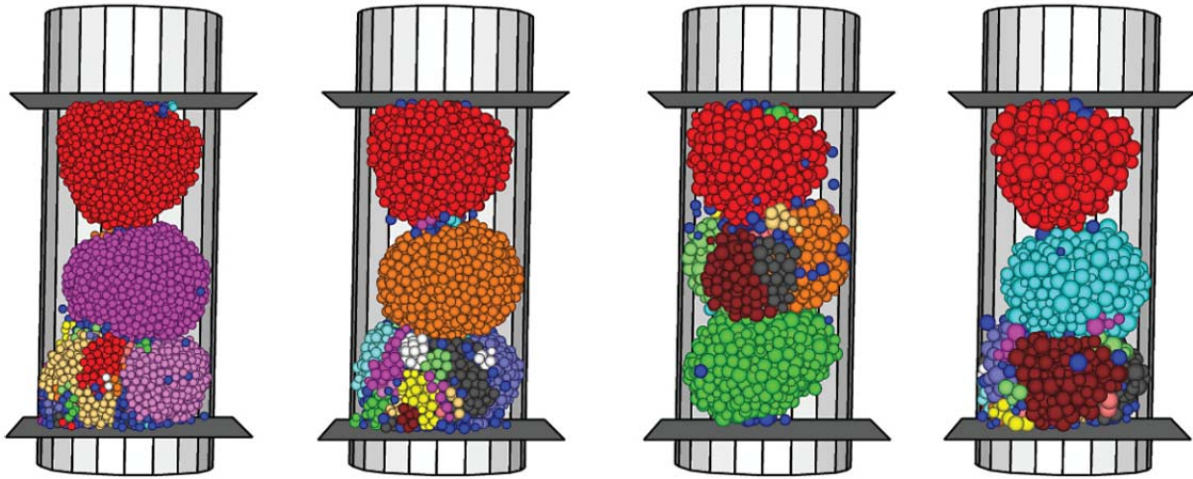


Figure 8. DEM simulation of confined compression of a particle chain indicating the effect of the number of sub-particles within the agglomerate in the simulated crushing response of granular materials (Cil and Alshibli, 2015)

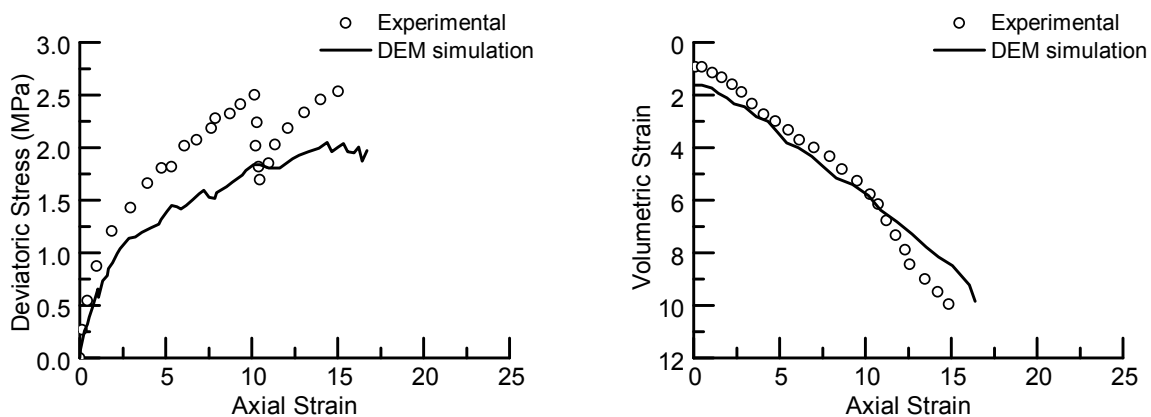


Figure 9. DEM simulation of stress-strain and volumetric response under triaxial compression (Tapias et al., 2015)

## 2.5 Potential Areas of Interest

### 2.5.1 Pile driving and penetration

A comprehensive understanding of the micromechanics of crushing is crucial for pile penetration in granular deposits. When a pile is driven into compressible sand, non-negligible particle crushing occurs, which in turn leads to the major deformation of the soil in proximity of the pile tip. Arshad et al. (2014) found through an experimental study that soil crushability during pile penetration is

highly dependent of particle size and shape, the depth of penetration, as well as the soil density. As shown in Figure 10, soil crushability controls the geometry of the displacement field, showing that vertical displacements increase beneath the pile tip. Moreover, the displacement field becomes wider for soils of higher density, implying that localized deformation occurs simultaneously with grain crushing during the penetration. Furthermore, the cone penetration resistance can be used to evaluate the mechanical behavior of granular soils i.e., stress state, soil strength, and susceptibility to liquefaction (Salgado et al., 1997). Therefore, a fundamental understanding of particle crushing mechanisms is important to interpret in-situ tests and guarantee an objective site characterization in deposits for which undisturbed samples cannot be retrieved.

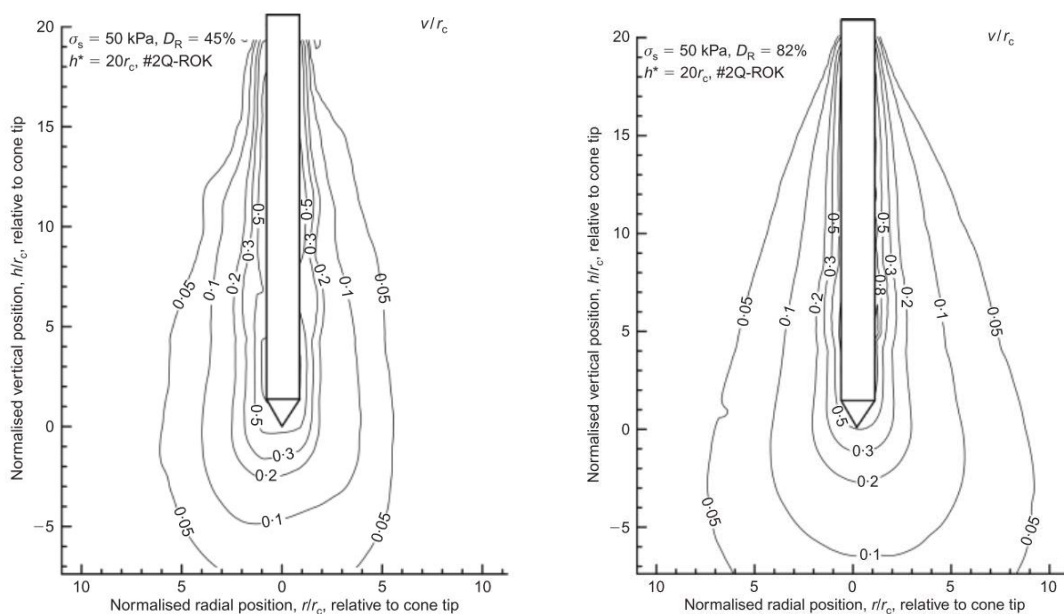


Figure 10. Normalized vertical displacement after cone penetration (left): relative density,  $D_R = 45\%$ ; (Right): relative density,  $D_R = 82\%$  (Arshad et al., 2014)

### 2.5.2 Subsidence

Ground (or surface) subsidence is a major cause of geological disasters and economic loss due to extraction of hydrocarbons and other underground fluids. An example is groundwater extraction in the coastal plain area in Tianjin, China which has been initiated in 1898 and dramatically increased after 1949. Such activity has eventually resulted in a maximum cumulative ground subsidence of up to 3.08 m from 1959 to 2007 and approximate economic losses of USD 18 billion (including damages in the building, drainage system, water supply system, gas pipelines, road networks, bridges, and railway system (Lixin et al., 2010)). Similarly, coastal Louisiana in the Gulf of Mexico, USA, where frequent production of hydrocarbons (including the withdrawal of oil and gas reservoirs) has determined significant land loss (Chang et al., 2014). In particular, as shown in Figure 11, ground settlement has been continuously observed in the post-depletion stage, which in turn caused losses of more than USD 37 billion for infrastructure and service rehabilitation over 50 years (Chan and Zoback, 2007).

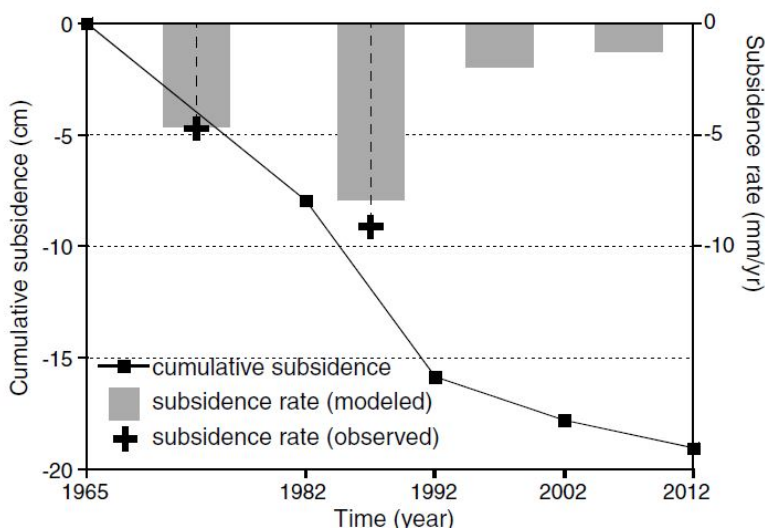


Figure 11. Cumulative subsidence of sand reservoir. Active production for the 17-year period (1965 – 1982) induced sand reservoir compaction, which resulted in the maximum surface subsidence of nearly 8 cm. Slow pore pressure drainage from the bounding shale resulted in an additional 8 cm subsidence for the first 10 years after depletion (1982 – 1992) (Chang et al., 2014)

Although multiple factors are involved in ground subsidence, one of the components that triggers the settlement and determines its long-term evolution is the compaction of the reservoir when the pore pressure decreases during depletion. As illustrated in Figure 12, depletion, in fact, induces a simultaneous increase of effective stress and decrease of permeability that can be active over very long time scales (Zhang and Buscarnera, 2017, Esna Ashari et al., 2018). When the effective stress increases beyond a threshold, the reservoir rocks are subjected to permanent compression and possible grain crushing, consequently inducing rearrangement of the microstructure and loss of permeability which lead to a deterioration of the reservoir quality and possible propagation of permanent surface subsidence. Over time, the economic and environmental consequences of these processes can be dramatic, in that they can severely damage infrastructures and ecosystems.

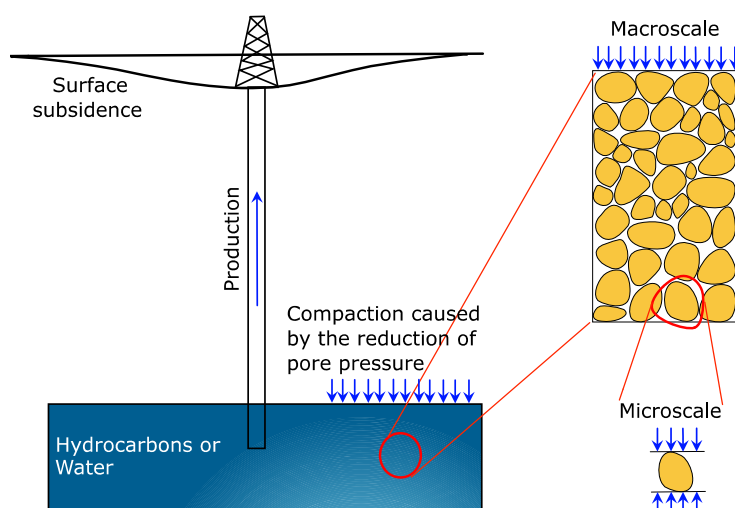


Figure 12. An impact of particle crushing on the ground subsidence

### 2.5.3 Mechanics of fault gouge

Other examples relevant for the mechanics of geomaterials under high pressure come from the area of geophysical sciences. Tectonic deformations, seismogenic ruptures, healing and

granulation form a fault gouge along a localized zone of compaction in a rock are all examples in which the granular materials constituting the Earth undergo major microstructural changes. As shown in Figure 13, the fault zone disintegrates into individual constituents that further fragment during slip (Ben-Zion and Sammis, 2003, Marone et al., 1995, Tenthorey et al., 2003). Such micro-scale physical phenomena are directly associated with movements at plate-tectonics scale (i.e., translation and rotation), and hence a fundamental understating of the complex microstructure is necessary to predict the temporal dynamics of large-scale crustal failures.

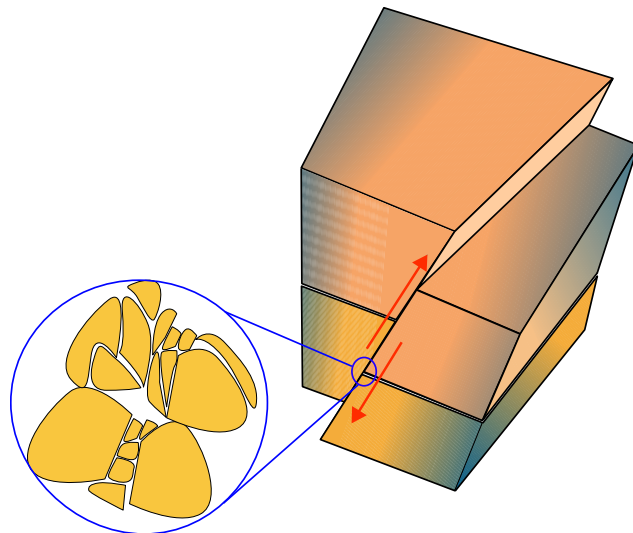


Figure 13. Effect of confined comminution on the physics of fault gouge

## CHAPTER 3: LABORATORY EQUIPMENT AND METHODOLOGY

### 3.1 Introduction

This chapter provides an overview of the micro-scale and macro-scale experimental program and the testing methodology. General descriptions and details regarding the specific micro-scale testing used via a miniaturized test apparatus are provided. Additionally, the macroscale one-dimensional consolidation test apparatus and its methodology are described along with detail testing procedures. The characteristics of the tested granular materials are presented including the physical and mechanical properties with visual observations through scanning electron microscope (SEM) images.

### 3.2 Testing Materials

Two classes of granular materials were used for this study: silica sands and glass beads. Constraints to the availability of similar shape characteristics for multiple grain sizes, as well as limitations of the testing devices restricted the analysis to three size values. Despite such limitations, the selected materials allowed a rather broad characterization of the role of size and shape on the link between particle strength and macroscopic yielding. Three sands characterized by different average particle size were selected, namely Q-ROK#1 ( $D_{50} = 0.350$  mm), Q-ROK#2 ( $D_{50} = 0.670$  mm), and Q-ROK#4 ( $D_{50} = 1.000$  mm). Similarly, three types of glass beads were used, i.e. small (SGB,  $D_{50} = 0.145$  mm), medium (MGB,  $D_{50} = 0.520$  mm) and large (LGB,  $D_{50} = 1.132$  mm) average particle size. Lastly, 20/40 Ottawa sand ( $D_{50} = 0.600$  mm) was selected. All granular materials are commercially available from US Silica and Corpuscular, Inc., respectively. Q-ROK sands and Ottawa sand have a specific gravity of 2.65 and their primary constituent is quartz. By contrast,

the selected glass beads are made of soda-lime glass with a specific gravity of 2.50. The minimum void ratios for each material were obtained by pouring multiple layers in a stainless steel container and densifying them by tamping and vibration based on ASTM D4253 (Table 1).

Table 1. Summary of physical and index properties, and mineralogical characteristics for testing granular materials in this study

| Material     | $G_s$ | $e_{min}$ | $D_{50}$ (mm) | Mineral         |
|--------------|-------|-----------|---------------|-----------------|
| Q-ROK#1      | 2.65  | 0.59      | 0.350         | Quartz          |
| Q-ROK#2      | 2.65  | 0.76      | 0.670         | Quartz          |
| Q-ROK#4      | 2.65  | 0.76      | 1.000         | Quartz          |
| 20/40 Ottawa | 2.65  | 0.60      | 0.600         | Quartz          |
| SGB          | 2.50  | 0.55      | 0.145         | Soda-lime glass |
| MGB          | 2.50  | 0.58      | 0.520         | Soda-lime glass |
| LGB          | 2.50  | 0.61      | 1.132         | Soda-lime glass |

The initial particle shape was assessed from two-dimensional images taken on 30 particles from each batch of grains. In particular, the minimum, maximum and average values of circularity (defined as  $C = 4\pi A / P^2$ , where  $A$  is the particle area and  $P$  is its perimeter) and roundness (here defined as  $R = 4A / (\pi D_{max}^2)$ , where  $D_{max}$  is the Feret diameter, i.e. the longest span across the particle) were quantified (Table 2). The results reflect nearly spherical shapes for glass beads, rounded for Ottawa sand, and non-negligible asperities for Q-ROK sands. These attributes were confirmed by visual inspection based on scanning electron microscope (SEM) images (Figure 14), which indicated Q-ROK grains with highly angular traits and rough surface texture, Ottawa sand with rounded and smooth surfaces, and glass beads with spherical morphology and smooth surfaces.

Table 2. Summary of the minimum, maximum and average values of circularity and roundness measurements

| Material     | Circularity, $C$ |           |              | Roundness, $R$ |           |              | Angularity |
|--------------|------------------|-----------|--------------|----------------|-----------|--------------|------------|
|              | $C_{min}$        | $C_{max}$ | $C_{avg}$    | $R_{min}$      | $R_{max}$ | $R_{avg}$    |            |
| Q-ROK#1      | 0.627            | 0.905     | <b>0.804</b> | 0.488          | 0.812     | <b>0.678</b> | Subangular |
| Q-ROK#2      | 0.629            | 0.885     | <b>0.748</b> | 0.503          | 0.758     | <b>0.650</b> | Angular    |
| Q-ROK#4      | 0.594            | 0.837     | <b>0.734</b> | 0.409          | 0.824     | <b>0.650</b> | Angular    |
| 20/40 Ottawa | 0.830            | 0.979     | <b>0.911</b> | 0.574          | 0.854     | <b>0.747</b> | Round      |
| SGB          | 0.894            | 1.002     | <b>0.969</b> | 0.657          | 0.955     | <b>0.881</b> | Spherical  |
| MGB          | 0.942            | 0.987     | <b>0.973</b> | 0.728          | 0.991     | <b>0.934</b> | Spherical  |
| LGB          | 0.993            | 1.000     | <b>0.997</b> | 0.920          | 0.989     | <b>0.970</b> | Spherical  |

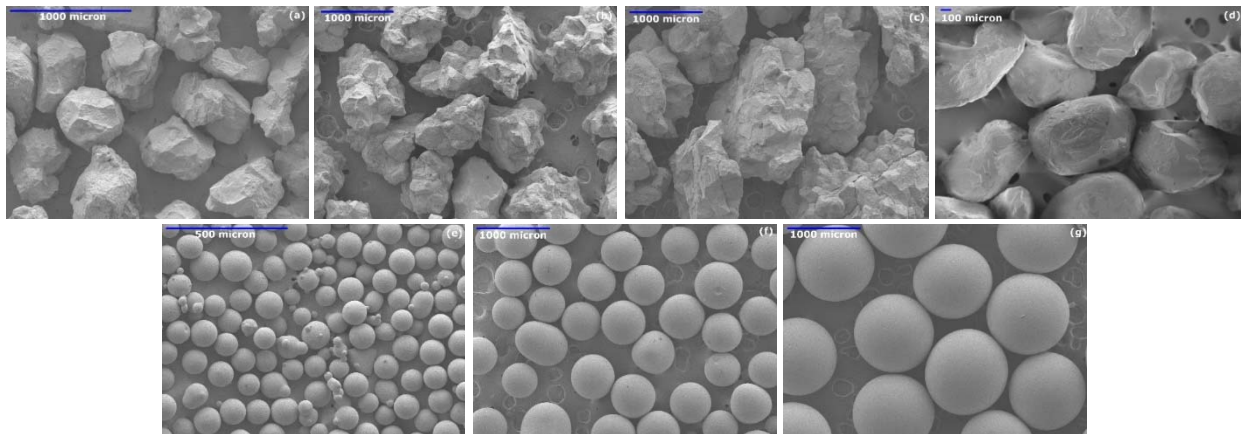


Figure 14. SEM images of (a) angular Q-ROK#1 sands; (b) Q-ROK#2 sands; (c) Q-ROK#4 sands; (d) rounded 20/40 sieved Ottawa sands; (e) spherical small glass beads (SGB); (f) medium glass beads (MGB); (g) large glass beads (LGB). Particles of the same class with different size exhibit similar shape characteristics

The grain size distribution (GSD) curves of the abovementioned sands and glass beads were determined by sieve analysis based on procedures delineated in ASTM D6913 and reported in Figure 15, which showed that while all the selected types of particles had a narrow size variability, the GSDs of batches with smaller grain sizes tended to have relatively less uniformity than coarser grains, thus implying stronger size variability for Q-ROK#1 and SGB than for Q-ROK#4 and LGB.

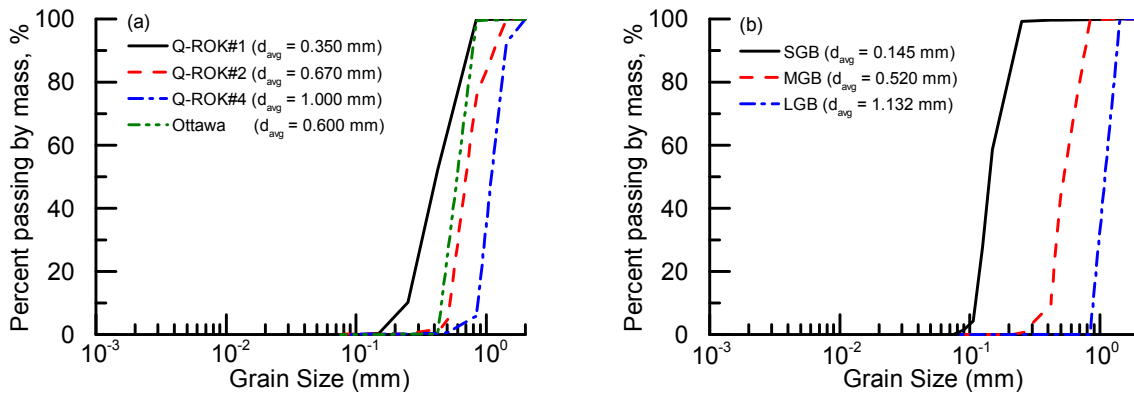


Figure 15. Initial grain size distribution curves of (a) 4 Silica sands and (b) 3 glass beads

### 3.3 Miniaturized Test Apparatus

#### 3.3.1 Description and design

A miniaturized testing apparatus was specially designed to conduct micro-scale geotechnical experiments (i.e., diametral compression tests, oedometer tests, and creep tests). The device was specifically developed to investigate mechanical responses (i.e., stress-strain behavior and volume change) and local failure modes of granular geomaterials under a high vertical stress. The term, miniaturized, has been used because the prepared sample size is relatively small (i.e., a cylindrical soil specimen has a typically 4-mm diameter with 5-mm height). The testing cell can be used in combination with 3D X-ray microtomography imaging techniques, enabling direct observations of the micro-scale characteristic of geomaterials. (i.e., evolution of particle morphology, local particle-to-particle fracture mode, and packing condition). Such a versatile testing equipment has been manufactured by Romus Inc., Illinois, USA (Figure 16), and it consists of two key components: i) a National Instrument USB-6216 data acquisition system acquiring sensor measurements and transferring to a computer as digital data, and ii) a test cell.

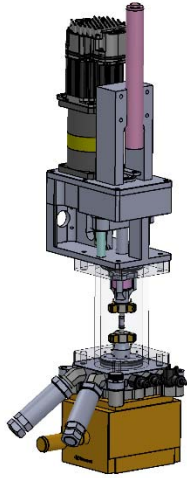


Figure 16. Schematic of the miniature compression test cell used for the multiscale laboratory experiments

The test cell is composed of an actuator, load cell, linear variable differential transducer (LVDT), two stainless steel loading pistons, acrylic cylindrical container, pore pressure transducer, and base plate. The actuator (Model CPM-MCVC-2310P-RLN, Teknic Inc.) is the servo system controlling the constant speed while exerting force on a sample. Displacement rates in the range of 0.01 mm/min up to 20 mm/min can be imposed. The axial translation range of the servo system is nearly 30 mm, thus providing a capacity of more than 50% axial strain for a sample specimen with 50 mm height. The axial force is measured via a load cell with a diameter of 19 mm (Model LC302-250 Omega, Inc.) with a capacity of 1112 N having a resolution of 0.10 N. The load cell is attached to the top loading platen. The axial displacement is measured through a 25-mm range LVDT (Model LD620-25, Omega Inc.) of stainless steel body. An acrylic cylindrical container of 44 mm inner diameter with a height of 132 mm is used to support the loading frame, particularly considering the X-ray penetrability and the possibility of reconstructing X-ray tomography images at Argonne National Laboratory which will be further discussed in Chapter 6. The pore pressure

transducer (PX309-005G5V, Omega Inc.), having a measurement range up to 34.5 kPa and an accuracy of  $\pm 0.25\%$  can be used to monitor the development of porewater pressure of the saturated soil specimen during the various stages of loading. The miniaturized test cell also has equipped with an inlet and outlet hole for the experiments testing chemo-mechanical interactions (i.e., mineral precipitation, dissolution, and reactive flow in porous media). Actuator control and measurements are processed by a customized data analysis algorithm within the LABVIEW software that enables to implement the displacement-controlled and load-controlled experiments (Figure 17).

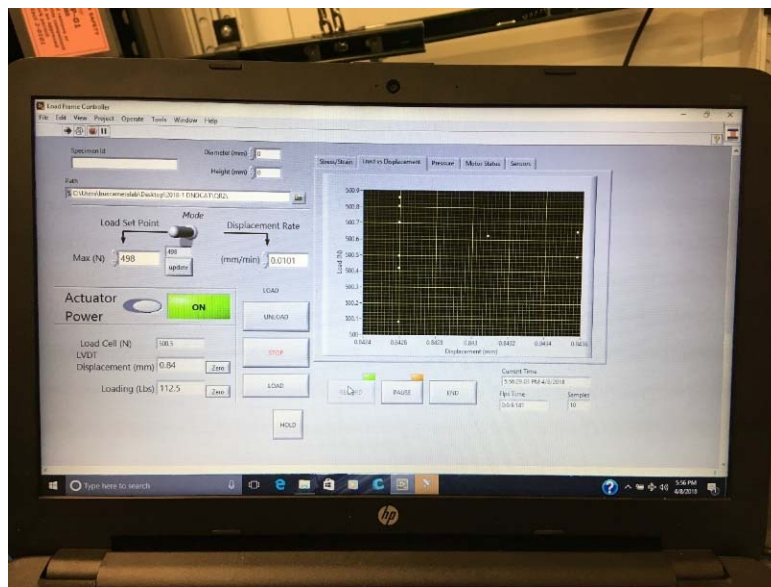


Figure 17. A layout of the LABVIEW software for data acquisition of force and displacement measurements

### 3.3.2 Diametral compression tests

Figure 18 shows a typical setup of the diametral compression test to determine the force-displacement response of individual grains. To set up a diametral compression test for single particles, the base plate is first prepared for deposition. A loading piston is placed within a hole inside the bottom platen and tighten firmly with an attached screw. The acrylic container is then

placed over the base platen and held securely together by four screws. A loading frame is placed on the acrylic container with a piston attached to a hole in the top platen. Sensor cables attached to the data acquisition system are tightly connected to the loading frame, enabling the measurement of force and displacement through the built-in load cell and LVDT, respectively.

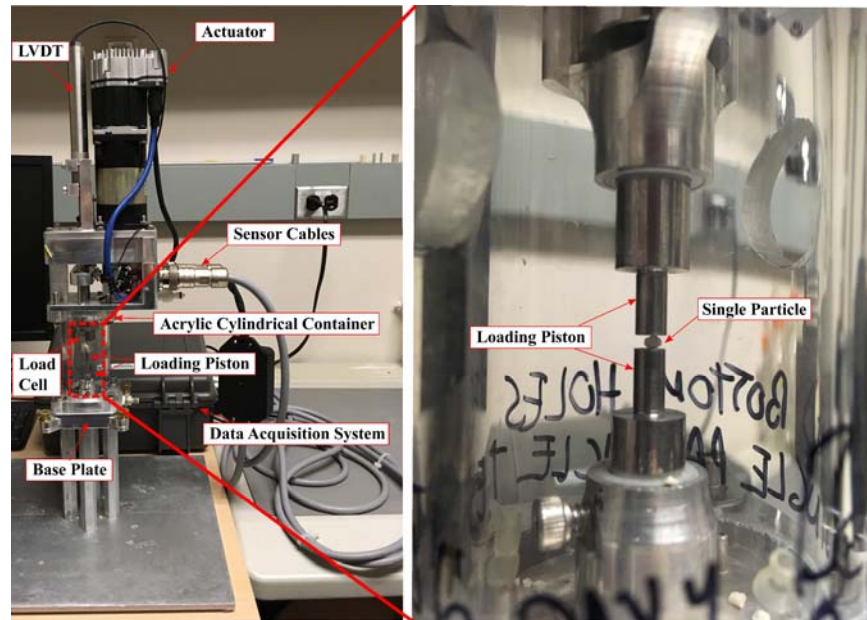


Figure 18. General setup of a diametral compression test

After test setup is complete, an individual grain is placed in the small gap between top and bottom loading pistons (Figure 18). Within the LABVIEW software, the current reading values for force and displacement should be set to zero prior to run tests. This study has been performed at a strain-controlled condition, and therefore the actuator feedback in the software is set to the mode called *displacement rate*. Prior to testing, it is important to ensure that the top loading piston moves freely upward or downward without side friction, thus preventing inaccuracies in force measurements and in turn incorrect particle strength results. During the test, axial load is continuously applied at a constant quasi-static displacement rate (i.e., 0.00083 mm/sec) up to failure, which is identified when a particle is broken into multiple fragments.

Following test completion, the measured data file is saved within the LABVIEW software. The test data can be exported and saved as a comma-delineated file (.csv file). Prior to disassembling, the axial load and displacement in the system are reset to zero by unloading. The top piston is then raised to the original position, and the fragmented particle can be removed. After discarding the tested grain, a new individual particle is placed in the same position for another test. The results from these tests are discussed and summarized in Chapter 4.

### *3.3.3 Oedometric compression tests*

Figure 19 illustrates a general setup for the uniaxial compression test on an assembly made of granular materials using the miniaturized test apparatus. To set up the oedometer test, the base plate is first prepared for deposition. A loading piston is then placed in a hole inside the bottom platen. An aluminum tubing having a 4.1 mm diameter and 18 mm height is prepared and placed on the bottom loading piston. Specimens are then prepared using dry pluviation, i.e., pouring sand particles in an aluminum tubing through a funnel and densifying them with tamping and vibration until obtaining the desired void ratio. Specimens can have an initial height ranging from 4.0 to 6.0 mm depending on particle attributes (e.g., size and shape) as well as packing conditions. Given such dimensions, the total particle number inside the specimen varies between 300 and 500, a number which, although limited, will be shown to provide sufficient information to capture some salient features of collective grain interactions on the stress-strain response of crushable granular materials. Additionally, the concurrent use of X-ray microtomography imaging will be shown to provide direct confirmation about the local grain fracture characteristics, as well as about the evolution of particle morphology at various stages of compression or creep tests. After the sample preparation is completed, a top loading platen is then placed over the specimen, and the acrylic

cylindrical container is placed over the base platen and held securely together by screws. The loading frame is finally placed on the acrylic container with sensor cables attached to the data acquisition system. After completion of the test set-up, the oedometer test can be performed at a constant quasi-static displacement rate to quantify the macroscopic stress-strain response. While most oedometric compression tests have been conducted under dry conditions to facilitate the preparation of dense specimens, the same experiments can be conducted under fully saturated conditions by preparing the samples through wet pluviation. This technique was for instance used in creep tests to rule out possible effects of variable ambient humidity on the rate of deformation. The results from these tests are discussed and summarized in Chapter 6.

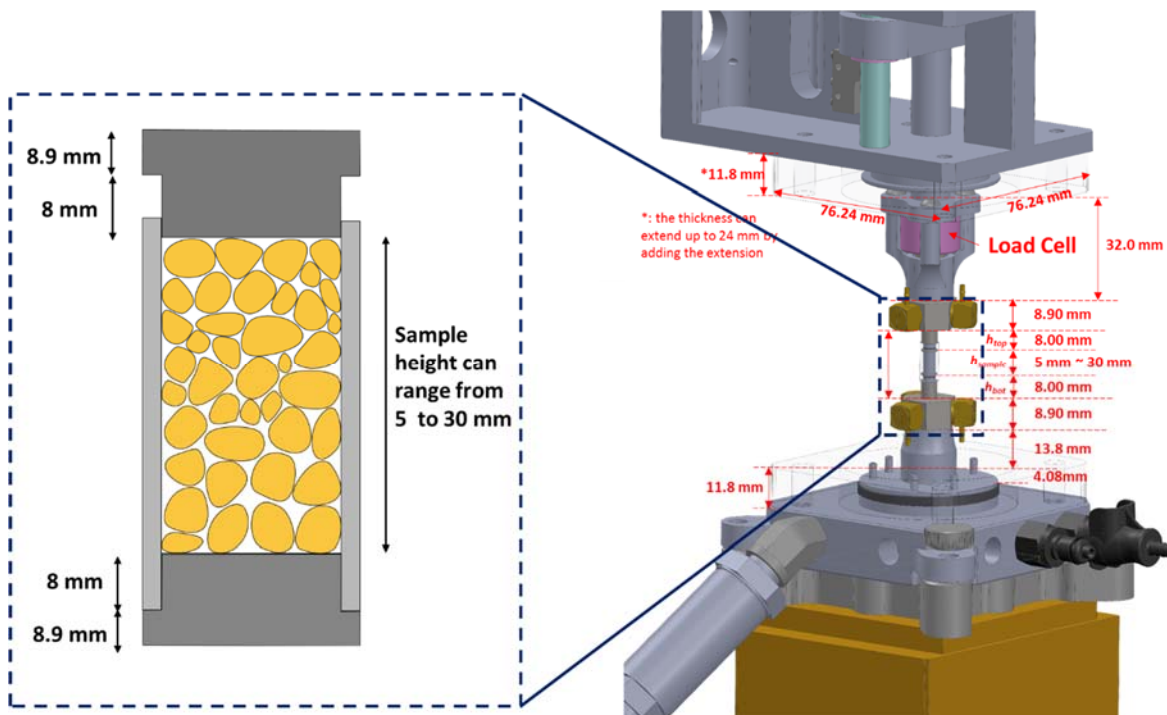


Figure 19. Schematic of the typical set-up for the miniaturized oedometer compression and creep tests

### 3.3.4 Creep tests

For this class of tests, all specimens are fully saturated with de-ionized water prior to the loading to minimize fluctuations of response due to ambient temperature or relative humidity. For instance, a small variation of temperature (Nara et al., 2013), PH level (Wiederhorn, 1974) or suction (Oldecop and Alonso, 2007, Brzesowsky et al., 2014, Ovalle et al., 2015) can lead alterations of the subcritical crack growth rate, and consequently resulting in untrustworthy data interpretation. Water is slowly injected to the samples inside an aluminum tubing. To avoid leakage between the bottom loading piston and aluminum tubing, a vacuum grease is used as sealant. Once water leakage is ruled out, the specimen is rained through a funnel into water-filled aluminum tubing and densified by gentle tamping and vibration. After water fully impregnates the densely packed specimen for about 10 minutes, the sample is then compressed at a constant strain rate of 0.022 mm/sec up to the desired creep stress level through the miniaturized test cell. The test is performed under drained condition, thus preventing the development of excess pore water pressure. When the applied stress reaches the desired creep stress, the actuator feedback is then switched to a load-controlled mode to maintain the sustained load up to 24 hours, often observed to be a time interval sufficient to develop the most substantial fraction of creep strains (e.g., Brzesowsky et al. (2014)). The results from these tests are discussed and summarized in Chapter 6.

## 3.4 One-dimensional Consolidation Test Apparatus

### 3.4.1 Description and design

One-dimensional compression tests have been carried out by using a fully automated load frame system (LoadTrac-II) manufactured by Geocomp Corporation. The LoadTrac-II load frame houses a micro-stepper motor, load cell, displacement transducer, and built-in controller (Figure 20). A

90 kN load cell is mounted on a rigid steel beam above the load platen to measure the axial force on a specimen composed of granular materials. The position of the platen is measured through a 76 mm LVDT sensor with a resolution of 1.3 micron while the micro-stepper motor moves the platen at 2000 steps per revolution (one step is equivalent to about 0.053 micron). The load cell and LVDT sensors are connected to the four-channel controller in which the digitized information is transferred to the computer that processes the measurements and converts them into engineering units. The controller supplies the excitation power to each sensor and the setting of analog output signals prior to converting them to the digital data. It uses a firmware-controlled signal conditioning to filter the low-level analog output and a 16-bit A/D converter for the high-level signal. The sensor readings are then transformed to an integer between 0 and 65000 that is referred to as the number of counts. Subsequently, the count readings are translated to engineering units through calibration factors.

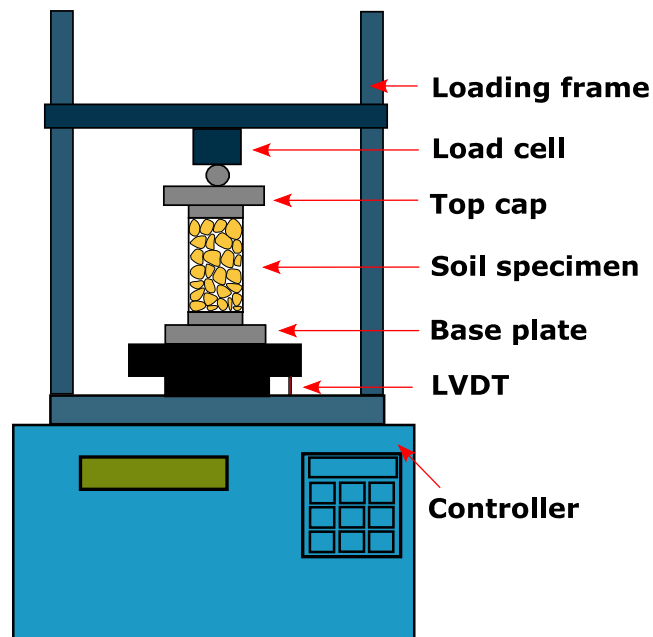


Figure 20. Schematic of the LoadTrac-II load frame for consolidation tests

### 3.4.2 Oedometer test

To set up a specimen, the sample container attached above the base plate is initially prepared for deposition. A 30-mm inner diameter of the steel bushing is placed inside the sample container. One of the specimen caps is then placed at the bottom of the container to ensure a flat and even surface for particle-to-platen contacts. A prescribed amount of the material is dry pluviated by funnel into the steel container, densifying them at multiple particle layers through tamping and vibration until the desired void ratio is obtained. Another specimen cap is then placed on the top of the prepared soil assembly. Afterwards, the loading piston is carefully placed onto the top surface of the specimen. When test setup is completed, the specimen mold is mounted onto the platen of LoadTrac-II load frame (Figure 21). In this step, excessive jolts or vibrations must be avoided to minimize any disturbances on the sample. The top cap should be properly seated on the sample specimen, and thus confirming its alignment at the center of the loading system.

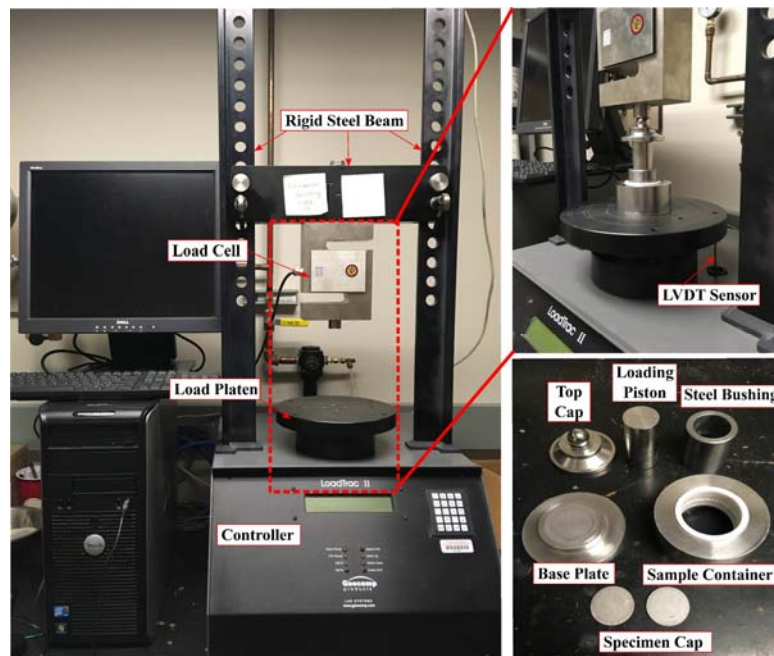


Figure 21. Setup for the oedometer test using the LoadTrac-II load frame

It needs to ensure that the values for load cell and LVDT sensors are zeroed prior to performance of each test. Furthermore, the calibration offsets must be updated for each test. After assigning data about the initial specimen conditions (i.e., initial diameter, height, and sample weight), the test can be initiated. The stepper motor enables to move the platen upward until the top cap of the specimen mold contacts the load cell. After the small gap between the load cell button and top cap is closed, the stepper motor would automatically stop. Lastly, all alignments, correction values and offsets should be checked prior to the test. The soil sample is then compressed at a constant strain rate of 0.00167 %/sec (i.e., quasi-static condition) up to a vertical pressure,  $\sigma_v = 100$  MPa. After the completion of testing, the axial displacement in the system is reset to zero by using the load frame keypad. The platen then moves to the lowest position, and the tested specimen can be stored. The results from these tests are further discussed and summarized in Chapter 4.

### 3.4.3 Creep test

For creep test setup, the base plate is first prepared for deposition (Figure 22). A 6.6 mm thick with a diameter of 84 mm porous stone is placed over the plate. A sample container is placed over the porous stone and firmly tightened with three screws. A 30-mm diameter stainless steel bushing is then pushed inside the container. A nearly 30-gram of geomaterials is dry pluviated by funnel into the stainless steel bushing, densifying them at multiple particle layers through tamping and vibration until the desired void ratio is obtained. A specimen cap is then placed on the top of the prepared soil assembly. Afterwards, the loading piston is carefully placed onto the top surface of the specimen. When test setup is completed, the specimen mold is mounted onto the platen of LoadTrac-II load frame. De-ionized water is slowly injected to the soil specimen flowing through the pipe connected to the base container. After the specimen is fully saturated for about 10 minutes,

the sample is compressed at a strain rate of 0.43 %/sec up to the desired creep stress state through the load frame. The test is performed at open drainage condition, indicating no excess porewater pressure generated throughout the experiment. When the applied stress reaches the desired creep stress, the actuator feedback is switched to a load-controlled mode to maintain it for up to 24 hours. This procedure is repeated at various creep stress levels for individual soil specimens. The results from these tests are discussed and summarized in Chapter 5.

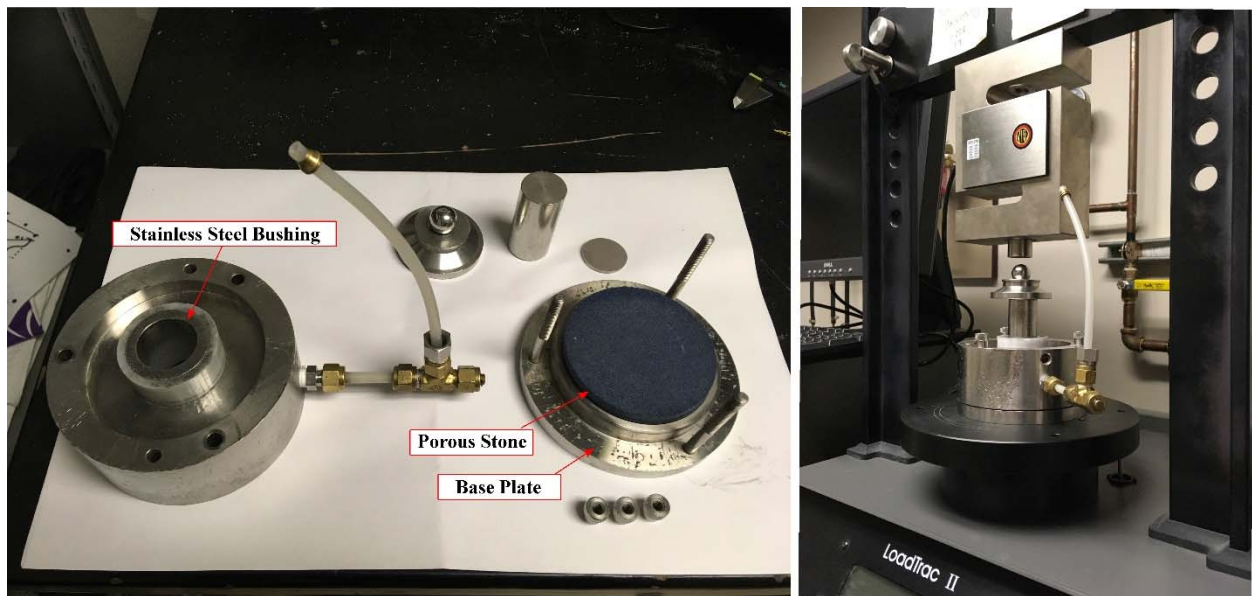


Figure 22. Setup for the creep test using LoadTrac-II load frame

## CHAPTER 4: COMPRESSION OF CRUSHABLE GRANULAR SOILS

### 4.1 Introduction

Particle breakage plays a key role on the compressibility of granular materials (McDowell et al., 1996, Nakata et al., 2001b, Zhang et al., 2016) and affects the performance of structures such as rockfill dams and deep foundations (Oldecop and Alonso, 2001, YANG et al., 2010). Identifying the microscopic origin of particle fracture and its role on soil properties are indeed essential for the design and monitoring of numerous engineering systems. For these reasons, significant efforts have been devoted to study grain breakage at particle and assembly scale with a variety of experimental techniques (Kuwajima et al., 2009, McDowell, 2002, Wang et al., 2002). Evidence from such works has shown that the breakage of particle assemblies correlates well with the characteristics of their grains (e.g., size, shape, and mineralogy). For example, coarse-grained soils exhibit low crushing resistance compared to finer materials because of the accentuated fragility of their particles (McDowell, 2002, Nakata et al., 2001a). Similarly, the variation of the failure mechanism in grains of different shape implies that samples made of angular grains display a smooth transition from elastic to plastic compaction, while those made of spherical particles exhibit a much sharper yielding (Nakata et al., 2001b). Experimental studies performed by Billam (1971), as well as Sadrekarimi and Olson (2010) have also shown that the amount of breakage caused by shearing increases with the size and angularity of the particles, as well as with the degree of uniformity.

From a modeling standpoint, numerous studies have examined the relation between energy input and comminution (Lade et al., 1996, Ovalle et al., 2013, Shahnazari and Rezvani, 2013),

suggesting a link between particle breakage and energy supply. These analyses, however, were conducted in terms of macroscopic quantities, thus providing limited links with grain-scale properties. More recently, the development of breakage mechanics (Einav, 2007a, Einav, 2007b) has enabled a direct analysis of the multiscale mechanics of crushing thanks to its ability to track the evolution of the grain size distribution. This theory establishes yielding criteria and evolution laws based on an energy measure that plays a similar role to that of the energy release rate in fracture mechanics (Einav, 2007c), thus offering a way to link energy input, comminution and stress-strain response. A recent study by Zhang et al. (2016) has exploited this link by defining a number of analytical models expressing the yielding of crushable solids in terms of the size and shape of their grains. This chapter is motivated by these results, and it aims to investigate the feedback between grain-scale properties and macroscopic compression through a coordinated set of experiments and simulations. In particular, two materials with distinct grain-scale properties (i.e. spherical glass beads and angular quartz sands) have been tested at particle and assembly level to assess the accuracy of different hypotheses for the storage of elastic energy (e.g., linear, Hertzian or conical contacts) and the mode of fracture (e.g., central split or contact fracture). In the following, the theoretical background (Section 4.2), as well as the materials and procedures employed in the experiments (Section 4.3) are described. The results of diametral compression tests on individual particles are then presented, by assessing them against predictions obtained for a range of fracture models (Section 4.4). Finally, the results of oedometric compression tests conducted on assemblies made by the same particles are used to examine the performance of different scaling laws, as well as to assess their predictive capabilities in the context of continuum breakage simulations (Section 4.5).

## 4.2 Theoretical Background

### 4.2.1 Particle-scale fracture models

The brittle failure of individual particles is often quantified by the characteristic strength,  $\sigma_{pc}$ , measured through diametral compression (Jaeger, 1967):

$$\sigma_{pc} = \frac{F_f}{d_p^2} \quad (4.1)$$

where  $F_f$  is the force at particle failure, while  $d_p$  is the particle diameter. Alternative approaches to describe the resistance of a particle rely on energy measures, such as the volume specific energy released by a single particle (Tavares and King, 1998),  $E_{pc}$ , computed by integrating the load-displacement curve up to the failure load  $F_f$ , as follows

$$E_{pc} = \frac{1}{V_p} \int_0^{\Delta_f} F d\Delta \quad (4.2)$$

where  $\Delta_f$  is the axial displacement at failure and  $V_p$  is the particle volume. Experimental and analytical investigations have shown that particles subjected to diametral loading exhibit major brittle fracture either at the center of the grain (Shipway and Hutchings, 1993) or at particle contacts (Hiramatsu and Oka, 1966). Figure 23 depicts schematically such different modes of fracture, illustrating how irregularities at the surface of the grains can favor failure at inter-particle contacts, while more regular geometries may promote major crack growth in proximity of a central plane, in which tensile failure is expected to occur. For both failure modes, Zhang et al. (2016) derived the expressions of failure load ( $F_f$ ) and energy released by a crushed grain ( $E_{pc}$ ) as a function of the particle size (see ‘‘Appendix A-C’’ for a summary of the equations). Power law expressions based on linear elastic fracture mechanics show indeed that a negative slope of 0.5 on a double-logarithmic  $\sigma_{pc} - d_p$  plane is expected for central splitting, whereas a negative slope of

1.5 is found if the particle fails at the contacts. On the other hand, since the specific energy input,  $E_{pc}$  is obtained by integration of the contact response up to failure, the resulting  $E_{pc} - \sigma_{pc}$  relations only depend on the contact behavior and can be used to determine the most appropriate contact law. In this context, it was shown that flat, spherical and conical contact models correspond to slopes of 2.0, 1.66 and 1.5 on a double logarithmic  $E_{pc} - \sigma_{pc}$  plane, respectively. Finally, it was shown that the relationship between  $E_{pc}$  and grain diameter,  $d_p$  is influenced by both failure mode and contact law, resulting in a wider range of size effects. Hereafter, the validity of such relations will be explored through compression tests conducted on two types of particles: spherical glass beads and angular quartz sands.

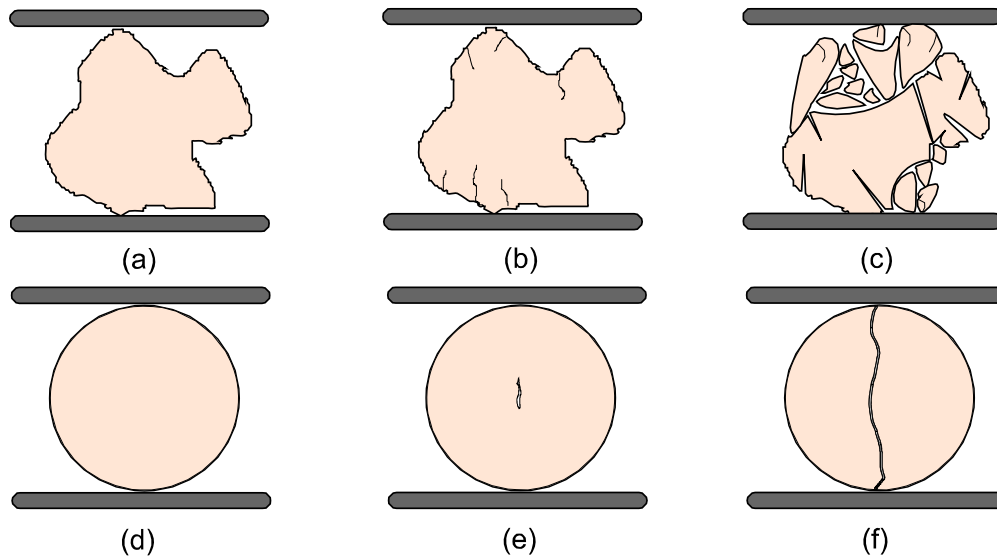


Figure 23. Schematics of two typical fracture modes: (a)-(c) contact failure due to local asperity damage; central splitting due to high tensile stresses on the median plane (d)-(f); (a) and (d): initial stage; (b) and (e) loading stage; (c) and (f): final stage

#### 4.2.2 Continuum breakage models

In analogy with fracture mechanics (Griffith, 1921), the breakage mechanics theory proposed by Einav (2007a) accounts for the evolution of the grain size distribution (GSD) of a granular material

subjected to confined comminution by postulating that macroscopic yielding occurs when the breakage energy (i.e., the energy released upon an infinitesimal shift of the GSD) reaches a critical threshold,  $E_c$ . The yielding condition considering both breakage and frictional processes can be expressed as:

$$\frac{E_B}{E_c}(1-B)^2 + \left(\frac{q}{Mp'}\right)^2 \leq 1 \quad (4.3)$$

where  $E_B = -\frac{\partial\Psi}{\partial B}$  is the breakage energy;  $\Psi$  is the elastic strain energy;  $B$  is the breakage index and  $E_c$  is the critical breakage energy (Einav, 2007a). The latter parameter  $E_c$  plays a crucial role in that it reflects the dissipative capacity of crushable materials. Most notably, it involves local and collective terms due to crushing (Nguyen and Einav, 2009), thus bearing a conceptual relation with the energy released by single grains,  $E_{pc}$ . To simulate the pressure-dependent elasticity and compute the values of breakage energy  $E_B$  in Eq (4.3), Nguyen and Einav (2009) used the following expression of strain energy potential:

$$\Psi_r^M(\varepsilon_v^e, \varepsilon_s^e, B) = (1 - \mathcal{G}_M B) \left[ \frac{p_r}{\bar{K}(2-m)} \Lambda^{\frac{2-m}{1-m}} + 1.5 p_r \bar{G} \Lambda^{\frac{m}{1-m}} (\varepsilon_s^e)^2 \right] \quad (4.4)$$

where  $\Lambda = \bar{K}(1-m)\varepsilon_v^e + 1$ , and the reference pressure,  $p_r$  is assumed to be 1 kPa.  $\bar{K}$  and  $\bar{G}$  are non-dimensional elastic constants to be calibrated based on the pre-yielding deformation response. The power law coefficient,  $m$ , can be used to reflect the macroscopic implications of different contact laws (e.g.,  $m = 0$  for linear contacts,  $m = 0.33$  for Hertzian contacts and  $m = 0.5$  for conical contacts). Combining yield criterion, elastic potential and hyperelastic relations ( $p = \partial\Psi / \partial\varepsilon_v^e$ ;

$q = \partial\Psi / \partial\varepsilon_s^e$ ), the yield stress upon oedometric compression can be approximated as Zhang and Buscarnera (2014):

$$\sigma_y' = \frac{3}{1+2K_o} \left[ \frac{E_c \left( 1 - \frac{\eta_{K_o}^2}{M^2} \right)}{\mathcal{G}_M \left( \frac{p_r \zeta_{K_o}^{2-m}}{K(2-m)} + \frac{\eta_{K_o}^2 \zeta_{K_o}^{-m}}{6p_r G} \right)} \right]^{\frac{1}{2-m}} \quad (4.5)$$

where  $\eta_{K_o} = 3(1 - K_o) / (1 + 2K_o)$  and

$$\zeta_{K_o} = \frac{1}{2p_r} + \sqrt{\left( \frac{1}{2p_r} \right)^2 - \frac{\bar{K}m\eta_{K_o}^2}{6\bar{G}p_r^2}}$$

in which the at-rest earth pressure coefficient,  $K_o$ , can be estimated with the standard Jaky's formula (Jaky, 1944). The grading index,  $\mathcal{G}_M$ , quantifies the distance between initial GSD and ultimate GSD, and can be evaluated based on the following expression, which assumes a uniform initial grading and an ultimate fractal GSD (Buscarnera and Einav, 2012):

$$\mathcal{G}_M = 1 - \frac{3}{2} \left( \frac{3-\alpha}{5-\alpha} \right) \left( \frac{d_M^4 - d_m^4}{d_M^6 - d_m^6} \right) \left( \frac{d_M^{5-\alpha} - d_m^{5-\alpha}}{d_M^{3-\alpha} - d_m^{3-\alpha}} \right) \quad (4.6)$$

where  $d_m$  is the minimum grain size,  $d_M$  is the maximum grain size, and  $\alpha$  is the fractal dimension of the GSD at the ultimate state (here assumed as  $\alpha = 2.7$ ).

### 4.2.3 Bridging microscopic and macroscopic processes

Considering the isotropic compression of a granular specimen, the assembly will first experience a nearly reversible compaction stage that can be approximated as elastic. Upon continuous loading, grains accumulate elastic energy through deformation at inter-particle contacts. Crushing events begin to occur when the energy stored in a sufficient number of grains exceeds a given threshold, thus causing the redistribution of contact forces and permanent compaction. These events manifest macroscopically in the form of plastic yielding (i.e., the sharp increase of the compressibility of the specimen) and in the ability to sustain larger compressive stresses (i.e., clastic hardening). In terms of macroscopic energy storage, the release rate of the total Helmholtz free energy of the system at yielding is denoted by the critical breakage energy  $E_c$ . Considering the links between local energy threshold  $E_{pc}$  at particle scale and the REV threshold  $E_c$ , Zhang et al. (2016) proposed the following linear scaling relation between these two energy measures:

$$E_c = \xi(1-n)E_{pc} \quad (4.7)$$

where  $n$  is the porosity of the assembly and  $\xi$  is a scaling factor. Such scaling law has been indirectly validated with several datasets on quartz sands reported in the literature (Zhang et al., 2016), finding that an approximated scaling factor of 0.25 provides a satisfactory agreement with experimental results reported by Nakata et al. (2001b) and McDowell (2002). More recently, Cil and Buscarnera (2016) conducted discrete element simulations to quantify the range of values viable for the scaling factor,  $\xi$ , obtaining values between 0.09 and 0.43 for a range of deterministic and probabilistic fracture models. The experimental program discussed here has the purpose to

corroborate these findings by testing directly the applicability of the abovementioned scaling law with reference to granular systems exhibiting wide range of size and shape characteristics.

### **4.3. Testing Materials and Procedures**

For this study, diametral tests and oedometer tests were performed on angular Q-ROK#1, #2, and #4 sands as well as spherical small, medium, and large glass beads. The material characteristics, as well as the testing procedures are described in Chapter 3.

### **4.4. Interpretation of Experimental Results: Particle-scale**

#### *4.4.1 Contact elasticity*

The parameters of the contact models are calibrated based on the load-displacement curves of 90 Q-ROK sand particles and 90 glass beads subjected to diametral compression. Inter-particle contact elasticity depends on the geometry of the contact zone. Here, three contact geometries are considered, namely flat (corresponding to a linear model), spherical (corresponding to an Hertzian model) and conical (see details in “Appendix B”). All contact models require the Young’s modulus  $E$  of the solid, as well as additional parameters specific for each law (e.g., the Poisson’s ratio  $\nu$  of the solid for Hertzian and conical models, the ratio between contact radius and grain radius  $a_c/R < 1.0$  for the linear model, and the tangent of the angle of contact  $A_s$  for the conical model). Figure 24 reports representative force-displacement curves of Q-ROK sand and glass beads, along with calibrated force-displacement curves for the selected contact laws. Due to its angularity, the Q-ROK sand particle exhibits local asperity damage and consecutive fragmentation events prior to the peak,  $F_f$ , at which the global failure is attained. The glass bead, on the other hand, exhibits a smooth nonlinear elastic response until it fails. The area under the load-displacement curves not

only reflects the dissipation due to surface area creation by fracture, but it may also include kinetic energy terms related to the sudden rupture of a particle.

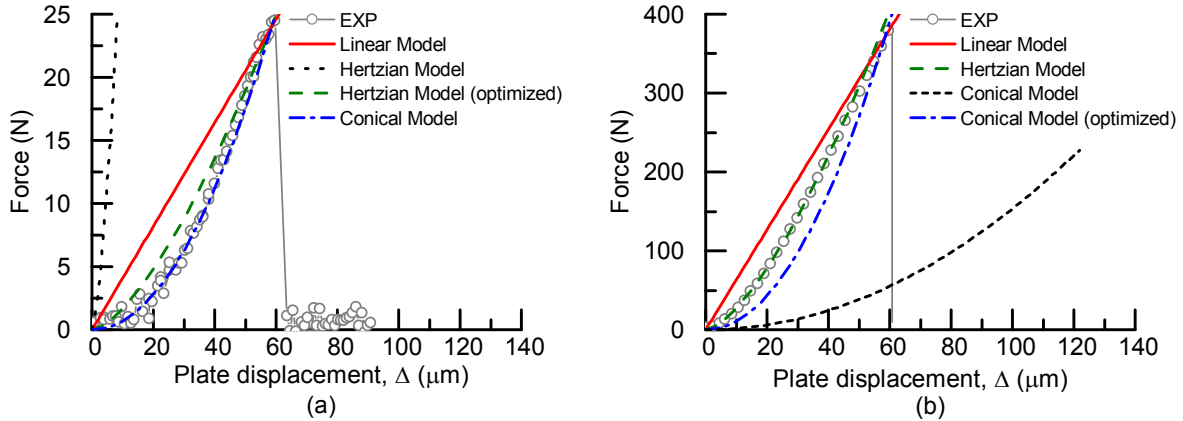


Figure 24. Examples of crushing tests for individual particles: (a) Q-ROK sand ( $d_p = 1.07\text{mm}$ ; with calibrated contact elasticity parameters:  $E = 95.6\text{ GPa}$ ,  $E_{\text{optimized}} = 4.90\text{ GPa}$ ,  $\nu = 0.077$ ,  $a_c/R = 0.072$  and  $A_s = 7.5$ ); (b) glass beads ( $d_p = 1.09\text{mm}$ ; with calibrated contact elasticity parameters:  $E = 70.0\text{ GPa}$ ,  $\nu = 0.30$ ,  $a_c/R = 0.316$  and  $A_s = 1.0$  and  $A_{s_{\text{optimized}}} = 0.020$ ). Calibrated parameters specific for the selected example curves, thus not coincident with those in Table 3, where averaged values based on a total number of 90 particles of Q-ROK sand and glass bead have been considered

When these processes occur in a matrix, the released energy is dissipated by particle rearrangement, force redistribution and frictional interactions. As a result,  $E_{pc}$  can be regarded as a reference measure of grain-scale energy losses based on which the links between local and collective crushing can be explored. Figure 24a also shows that the Hertzian model based on the typical elastic parameter for quartz (i.e.,  $E = 95.6\text{ GPa}$ , (Zhang et al., 1990)), significantly overpredicts the initial stiffness of the Q-ROK particle, thus underestimating the strain energy stored at the onset of failure (see  $E_{pc} - \sigma_{pc}$  relationship in Figure 25a). This result can be attributed to the variability of the local contact geometry caused by the angularity of Q-ROK sand particles. Thus,  $E$  has to be optimized to accurately represent the load-displacement curve up to the peak (i.e.,  $E = 4.0\text{ GPa}$  in Figure 24a). By contrast, the load-displacement curve of glass beads can be captured satisfactorily by the Hertzian law (Figure 24b) based on standard elastic parameters (i.e.,  $E = 70.0\text{ GPa}$  and  $\nu = 0.30$ , similar to those reported by Agnolin et al. (2009). Figure 24b also illustrates the

performance of the conical contact, by showing that an indentation based on  $A_s = 1.0$  (intermediate between flat and perfectly sharp contact) underestimates the stiffness of the glass bead. It is indeed necessary to optimize  $A_s$  to a much smaller value ( $A_s = 0.020$ ) to match the force-displacement curve, thus confirming the accuracy of the Hertzian model for particle contacts characterized by a relatively blunt geometry. Table 3 summarizes the average values of the calibrated parameters of the contact models resulting from the fitting of all load-displacement curves.

Table 3. Summary of averaged values of calibrated contact model parameters and fracture model parameters

| Parameter        |                              | Q-ROK Sands | Glass Beads |
|------------------|------------------------------|-------------|-------------|
| Elasticity model | $E$ (GPa)                    | 7.95        | 70.0        |
|                  | $\nu$                        | 0.077       | 0.30        |
|                  | $a_c/R$                      | 0.098       | 0.297       |
|                  | $A_s$                        | 17.7        | 0.055       |
| Fracture model   | $G_{IC}$ (J/m <sup>2</sup> ) | 0.95        | 0.95        |
|                  | $a'$                         | 16          | 23          |
|                  | $b'$                         | 112         | 120         |

As discussed above, the trends in the  $E_{pc} - \sigma_{pc}$  plane can be shown to be independent of the particle failure mode, thus providing a means to define the most accurate contact model for each material. A total of 180 particle crushing test results are plotted in Figure 25, together with model calibrations based on Eqs. (4.14), (4.16), (4.18) of Appendix B. While it is apparent that the  $E_{pc} - \sigma_{pc}$  relationship of Q-ROK sand is best captured by the conical law, the optimized Hertzian model also provides a satisfactory match. Similarly, for the case of glass beads the  $E_{pc} - \sigma_{pc}$  relationship is captured accurately by both the Hertzian model based on standard elastic constants and the optimized conical contact law. For simplicity, the trend lines associated with the non-optimized Hertzian model (Q-ROK sand) and conical model (glass beads) have not been reported in Figure 25(a), (b), respectively. It can indeed be shown that they display the same inclination of their

optimized counterparts, but an inaccurate match of the data points due to their inability to reproduce correctly the force-displacement curves.

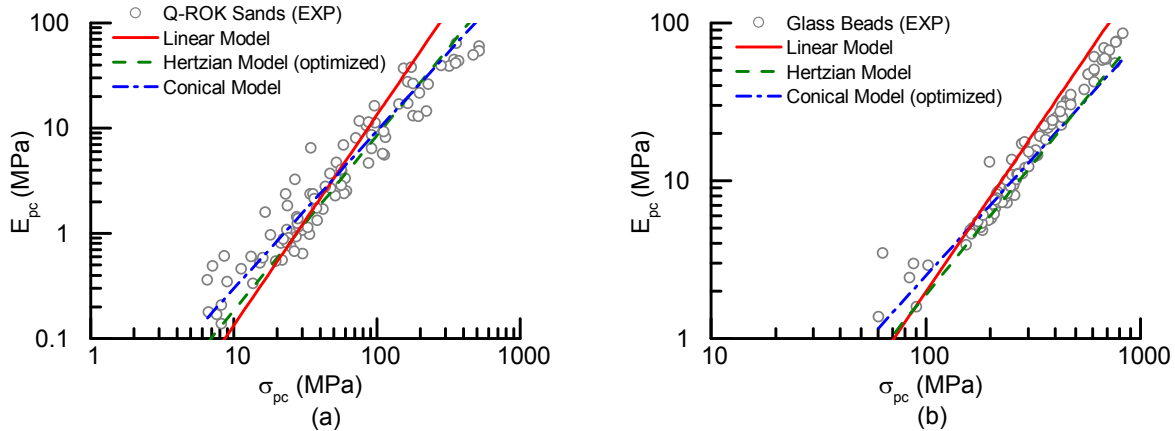


Figure 25. Energy-particle strength relationship for (a) Q-ROK sands and (b) glass beads with calibrated model predictions based on different elastic contact models

#### 4.4.2 Particle fracture mechanism

Two types of particle failure modes are considered in this study: (1) penny-shaped cracks initiating fracture at the center of the grain (*bulk fracture*); and (2) edge cracks oriented perpendicularly to the maximum tensile stress in the vicinity of grain-to-grain contacts (*surface fracture*). Analytical expressions of the failure load due to both fracture patterns are derived by Zhang et al. (2016) and are presented in Eqs. (4.11) and (4.12) of Appendix A. Table 3 summarizes the model predictions for Q-ROK sands and glass beads calibrated from Figure 26, which displays the relationship between particle size and average characteristic strength of Q-ROK sand particles and glass beads. The nominal strength of both sets of particles displays significant size dependence. Specifically, an increase in particle strength with decreasing particle size is more pronounced in Q-ROK grains compared to glass beads, thus implying a higher sensitivity to size effects in case of angular particles. As a result, the size-dependent strength of Q-ROK particles and glass beads is captured

by surface fracture and bulk fracture laws, respectively, thus suggesting that Q-ROK sand grains, due to the higher contact forces caused by their asperities are more likely to fracture at their surface, while glass beads are more likely to accumulate sufficient tensile stresses along the median plane and fail through central splitting.

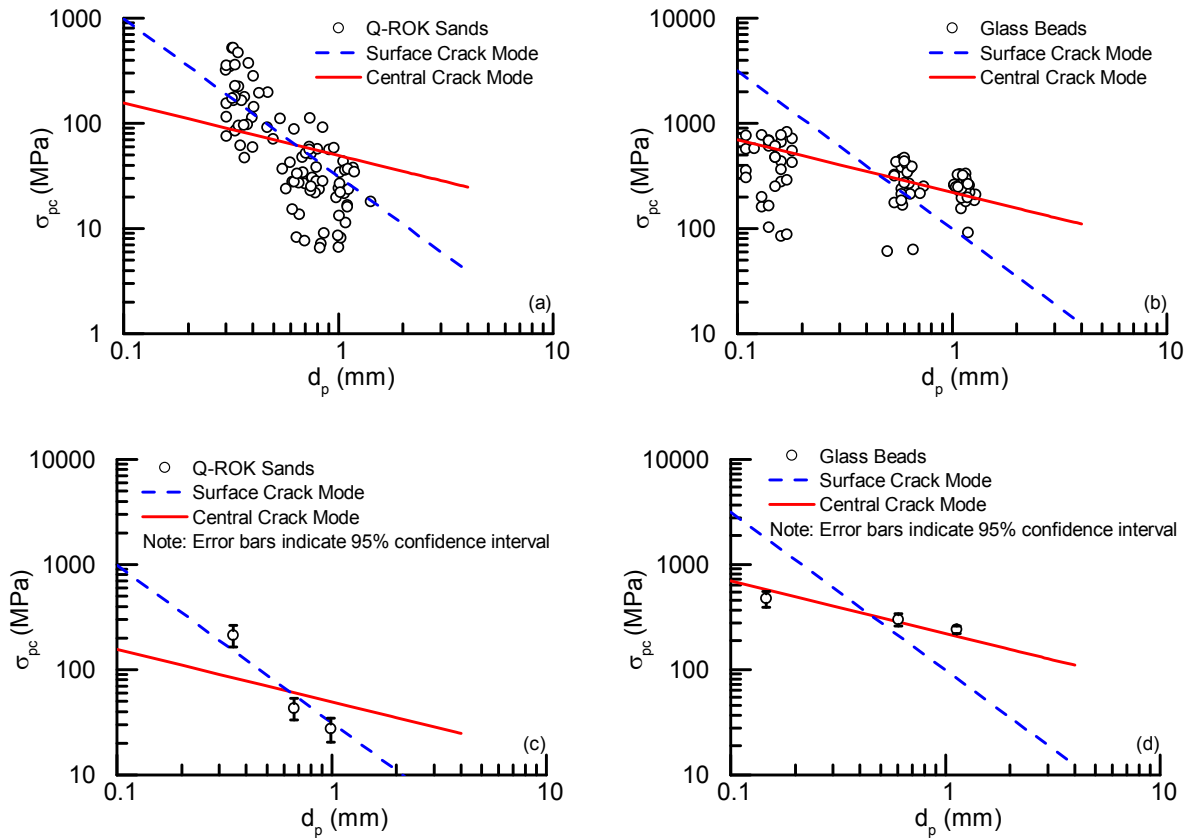


Figure 26. All particle strength obtained from diametral compression of (a) Q-ROK sand particles and (b) glass beads. The data cloud represents the characteristic particle strengths computed for each batch of particles on the basis of 30 experiments. Averaged particle strength with 95% confidence interval of (c) Q-ROK sands and (d) glass beads. The average values have been used to analyze the observed dataset for each batch of particles.

Figure 27 reports the size-dependence of the average value of energy stored at the onset of fracture,  $E_{pc}$ , for Q-ROK sand particles and glass beads, along with model results for four combinations of elastic and failure models (Eqs. 4.19-22 of Appendix C). Only the optimized versions of the contact

laws discussed in the previous paragraphs have been used in order to provide the most accurate estimate of  $E_{pc}$  at failure. The figure indicates that lower levels of volume-specific strain energy are necessary to cause failure in larger particles. It can be noticed that the combination of the optimized Hertzian contact law with the surface fracture model best captures the measured  $E_{pc}$  of Q-ROK sands, thus confirming once again that the fracture of angular particles tends to be controlled by surface fracture.

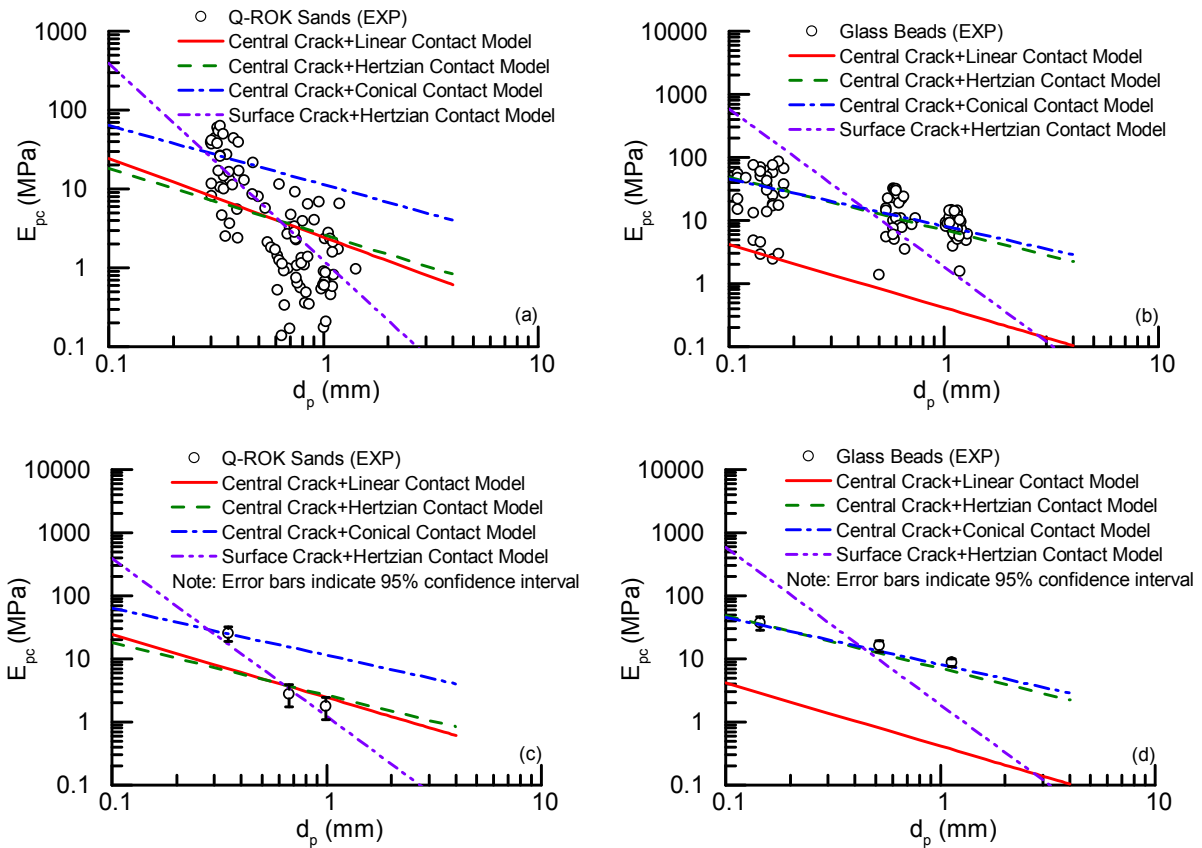


Figure 27. Values of volume-specific energy at fracture ( $E_{pc}$ ) plotted as a function of particle diameter for (a) Q-ROK sand particles and (b) glass beads, along with prediction of four combinations of contact and fracture models. The data cloud represents the values of  $E_{pc}$  computed for each batch of particles on the basis of 30 experiments. Averaged  $E_{pc}$  with 95% confidence interval of (c) Q-ROK sands and (d) glass beads. The average values have been used to analyze the observed dataset for each batch of particles.

By contrast, the combination of the bulk fracture law with either Hertzian or optimized conical contact provide the best predictions of the  $E_{pc} - d_p$  data for glass beads, thus corroborating the conclusion that their failure tends to initiate at the center of the particles. Although these conclusions are not based on the visual observation of fracture patterns, but rather on the chosen framework of interpretation, such findings provide an indirect confirmation that particle angularity plays an important role in the fracture behavior of individual grains thus potentially impacting the stress-strain deformation characteristics of granular systems subjected to high pressures.

#### 4.5. Interpretation of Experimental Results: Specimen-scale

##### 4.5.1 Macroscopic yield stress and critical breakage energy

The results of oedometric compression tests for six specimens of Q-ROK sand and glass beads with particles sizes ranging from small to coarse are reported in Figure 28.

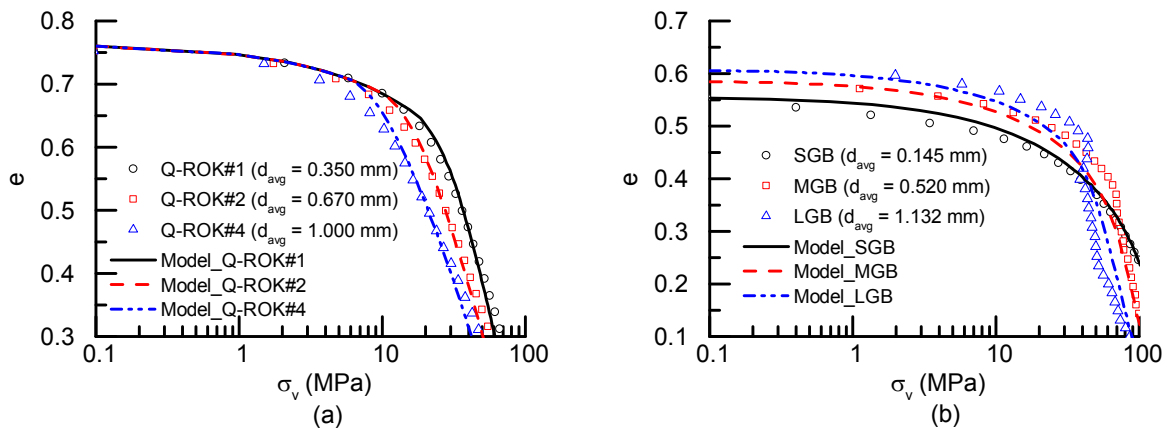


Figure 28. Oedometric compression tests results and model simulations based on the breakage mechanics model for: (a) Q-ROK sands and (b) glass beads

It can be noticed that Q-ROK#1 and SGB exhibit the largest values of macroscopic yield stresses, thus implying that assemblies made of smaller grains are less susceptible to particle fracturing. It

can also be noted that the sample consisting of large glass beads (LGB) exhibits a sharper increase of post-yielding compressibility in the  $e - \log \sigma_v$  plane compared to all other materials, which can be attributed to (i) larger particle size to specimen diameter ratio, (ii) nearly spherical particles and (iii) a very uniform initial GSD, all factors that when combined may enable the uniform occurrence of major particle splitting events across the sample volume without prior distributed asperity fragmentation.

The oedometric compression curves in Figure 28 have also been simulated through the breakage mechanics model. For this purpose, the grading index,  $\mathcal{G}_M$  has been estimated by Eq. (4.6) assuming  $\alpha = 2.7$  and  $d_m = 0.01$  mm. By contrast, the stress ratio at frictional failure,  $M$  has been computed as:

$$M = \frac{6 \sin \phi}{3 - \sin \phi} \quad (4.8)$$

where  $\phi$  is the interparticle friction angle of the considered granular material (here assumed to be  $38^\circ$  and  $22^\circ$  for Q-ROK sands and glass beads, respectively (Cho et al., 2006)) The coupling angle,  $\omega$ , that controls the relative proportion of dissipation by plastic compaction and grain breakage has been chosen based on the post-yielding compressibility, while the macroscopic critical breakage energy,  $E_c$ , has been optimized by matching the yield stress exhibited by the measured data (here defined for simplicity as the intersection between the logarithmic compression curve at high stress and the elastic compression curve (Cil and Buscarnera, 2016)). Table 4 reports the calibrated model parameters that fit the compression response of Q-ROK sands and glass beads. These results reveal that the critical breakage energy  $E_c$  is size-dependent (i.e, that assemblies consisting of large grains tend to have smaller  $E_c$ , thus implying that they are more susceptible to collective breakage). By

relating the calibrated values of critical breakage energy,  $E_c$ , to those defined for single particles,  $E_{pc}$  (Figure 27) it is possible to estimate the scaling constant  $\zeta$  (Eq. 4.7) associated with either glass beads or Q-ROK sands. It is found that the scaling factors for glass beads are all equal to 0.35, while those for Q-ROK sands range from 0.10 to 0.34 (with an average of 0.21, close to the value used by Zhang et al. (2016) for different sands). While in both cases these values fall within the range predicted by Cil and Buscarnera (2016) through DEM analyses, such analyses suggest that even small variations in particle angularity may cause non-negligible fluctuations of the scaling factors, which reflect the complex energetics of collective crushing in case of particles with irregular geometry. Moreover, inevitable variations of shape characteristics when passing from small to large sand particles, as well as differences in degree of uniformity (rather uniform in case of Q-ROK#2 and Q-ROK#4, but slightly polydisperse in case of Q-ROK#1) may have caused variations in packing and force distribution more pronounced with respect to those of glass bead samples, thus causing stronger macroscopic fluctuations of the scaling factor,  $\zeta$ .

Figure 29 reports the data in the  $E_c - d_p$  plane, comparing them against the size-dependent trends computed through four combinations of elastic models and failure laws. The figure confirms that surface fracture and optimized Hertzian contact elasticity offer the best approximation of the size-dependent critical breakage energy of Q-ROK sands, whereas the combination of a bulk fracture law with either Hertzian contact or optimized conical contact is the most successful in explaining the role of the particle size in glass beads. In agreement with particle-scale analyses (Figure 26), these results suggest that the collective crushing of assemblies made of angular grains (e.g., Q-ROK sand) tends to be primarily controlled by surface fracture mechanisms, whereas the trends exhibited by samples consisting of highly regular particles (e.g., glass beads) can be approximated by fracture laws based on central splitting.

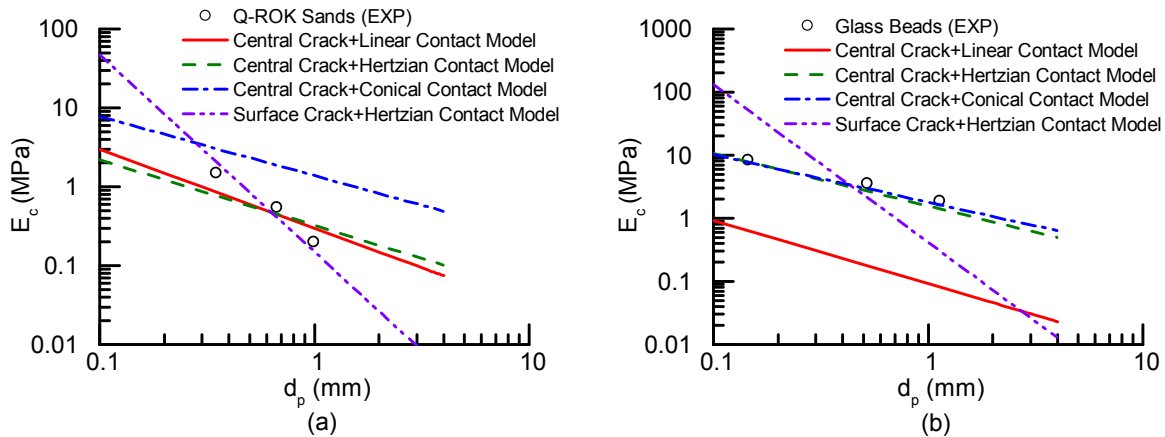


Figure 29. Critical breakage energy,  $E_c$ , as a function of particle diameters for (a) Q-ROK sand and (b) glass beads with the performance of four combinations of contact models and fracture models. The trend lines are predicted on the basis of calibrated particle-scale models (Figure 27) and averaged values of the scaling factor  $\zeta$  in Eq. (4.7) ( $\zeta = 0.35$  for glass beads and  $\zeta = 0.21$  for Q-ROK sands)

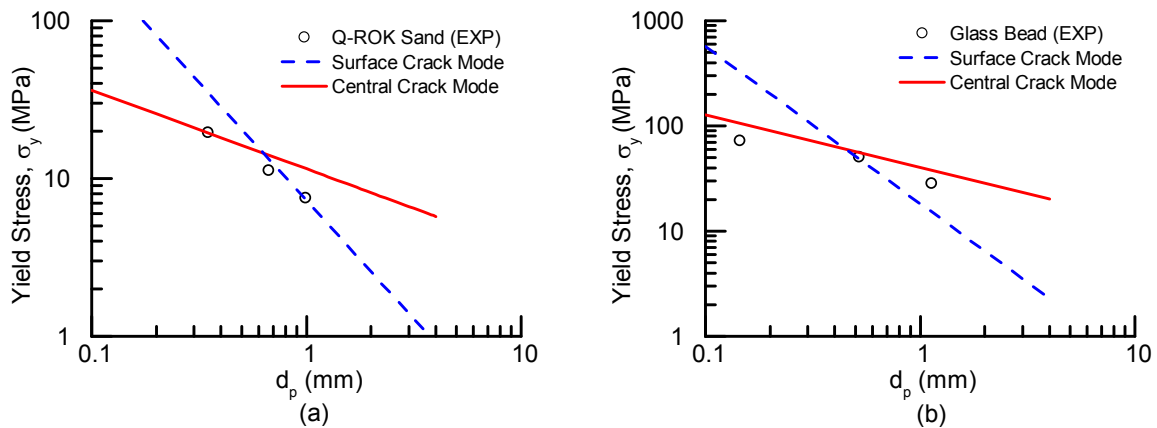


Figure 30. Average particle size and macroscopic yield stresses relationship of (a) Q-ROK sands; and (b) glass beads with the assessment of the performance of two considered fracture models

Similar conclusions emerge also from Figure 30, where the macroscopic yield stresses measured for the two classes of granular materials are plotted against the particle diameter and compared with the trends predicted by the theory by using Eqs. (4.5-7) and the optimized scaling factors in Table 4. It must be noted, however, that the latter interpretation is rather more complex, in that it is affected by system effects (see for instance Eq. (4.5), which includes parameters such as the stiffness of the packing and the earth pressure coefficient). Hence, the presence of data points

between the two theoretical trend lines might also reflect feedbacks between skeleton response, inter-particle coordination and local grain fracture, as well as a simultaneous presence of multiple fracture modes across the sample (Zhang et al., 2016).

Table 4. Summary of the calibrated parameters used for the simulations based on the breakage mechanics model

| Material | $d_{avg}$ (mm) | $e_o$ | $n$   | $d_m$ (mm) | $d_M$ (mm) | $\mathcal{G}_M$ | $M$  | $\bar{K}$ | $\bar{G}$ | $\omega$ (°) | $\zeta$ | $E_{pc}$ (MPa) | $E_c$ (MPa) |
|----------|----------------|-------|-------|------------|------------|-----------------|------|-----------|-----------|--------------|---------|----------------|-------------|
| QROK#1   | 0.350          | 0.76  | 0.430 | 0.01       | 0.84       | 0.734           | 1.55 | 8500      | 5100      | 15           | 0.10    | 25.60          | 1.500       |
| QROK#2   | 0.670          | 0.76  | 0.430 | 0.01       | 0.84       | 0.734           | 1.55 | 8500      | 5100      | 15           | 0.34    | 2.810          | 0.550       |
| QROK#4   | 1.000          | 0.76  | 0.430 | 0.01       | 2.00       | 0.754           | 1.55 | 8500      | 5100      | 15           | 0.20    | 1.770          | 0.200       |
| SGB      | 0.145          | 0.55  | 0.355 | 0.01       | 0.25       | 0.684           | 0.86 | 13000     | 14180     | 45           | 0.35    | 37.28          | 8.416       |
| MGB      | 0.520          | 0.58  | 0.369 | 0.01       | 0.84       | 0.734           | 0.86 | 13000     | 14180     | 45           | 0.35    | 16.20          | 3.577       |
| LGB      | 1.132          | 0.61  | 0.377 | 0.01       | 1.42       | 0.747           | 0.86 | 13000     | 14180     | 45           | 0.35    | 8.710          | 1.898       |

#### 4.5.2 Breakage evolution

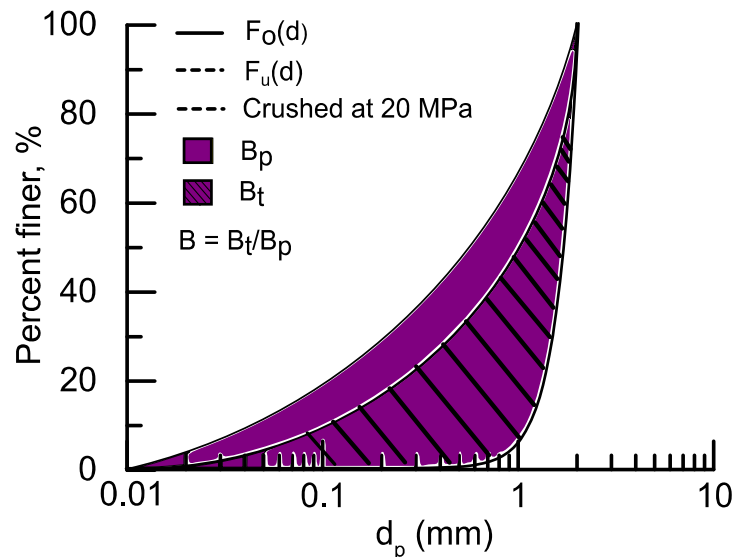


Figure 31. Illustration of the determination of the current breakage value,  $B$  for Q-ROK#4 sand at 20 MPa stress

Besides yielding characteristics, an important aspect of macroscopic comminution is the evolution of the GSD. The calibration of the breakage model parameters discussed in the previous section

enables the discussion of this aspect by tracking the values of breakage,  $B$  (Einav, 2007a) emerging from experiments and simulations. The breakage index can indeed be quantified as:

$$B = \frac{B_t}{B_p} \quad (4.9)$$

where  $B_p$  is the area between the initial and ultimate GSD and  $B_t$  is the area between the initial and the current GSD. Figure 31 illustrates an example of such computation with reference to the GSD at initial ( $F_0$ ), ultimate ( $F_u$ ) and current states ( $F$ , here for coarse Q-ROK sand at  $\sigma_v = 20$  MPa). In order to fit the shape of the abovementioned GSD curves, the approach proposed by Zhang and Buscarnera (2014) has been used, according to which initial and ultimate cumulative distributions can be expressed through Eq. (4.10), using  $\alpha = -1$  for  $F_0$  and 2.7 for  $F_u$ .

$$F_0 = F_u = \frac{x^{3-\alpha} - d_m^{3-\alpha}}{d_M^{3-\alpha} - d_m^{3-\alpha}} \quad (4.10)$$

Figure 32 reports the evolving magnitudes of particle breakage for Q-ROK sands and glass beads, as well as model simulations indicating that specimens with smaller particles exhibit lower values of  $B$  compared to assemblies made of larger particles under the same stress. The simulations capture satisfactorily the trends exhibited by both Q-ROK sands and glass beads, thus indicating that the breakage model calibrated with parameters inspired by grain-scale fracture laws can predict satisfactorily the evolution of particle crushing for both types of material.

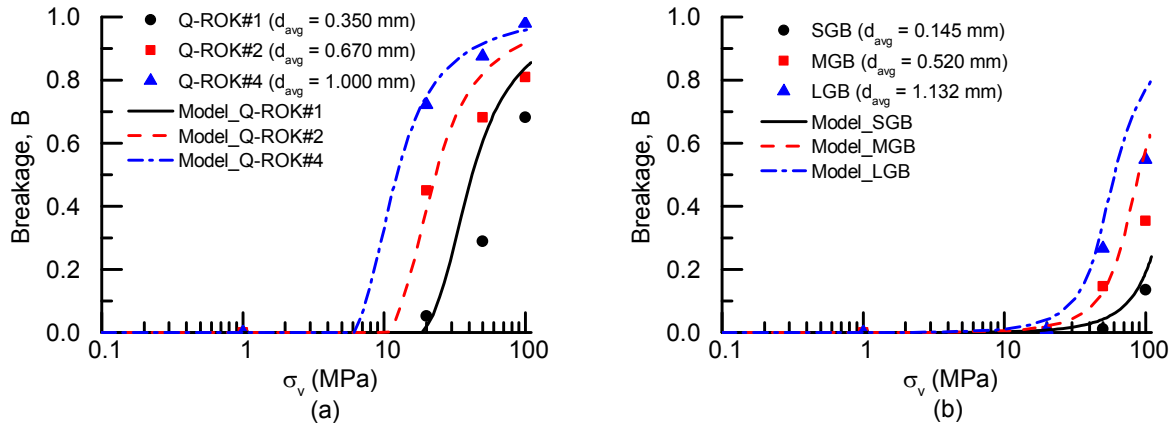


Figure 32. Evolution of  $B$  measured in the experiments (symbols) and computed through model data simulations (lines) for (a) Q-ROK sands and (b) glass beads

#### 4.6. Concluding Remarks

The role of particle shape and size on the crushing response of granular materials was investigated through experimental and theoretical analyses at both particle and assembly scales. The results showed that shape and size are two critical factors affecting the energetics of local grain crushing, as well as the macroscopic crushability of a sample. Particularly, the use of a range of contact models and fracture laws for the interpretation of the measurements obtained for spherical glass beads and angular quartz sands showed that both the energy storage prior to fracture and the mode of particle failure were controlled by the shape characteristics of the grains. The key findings of the study can be summarized as follows:

1. By calibrating a range of elastic contact models against force-displacement curves obtained from diametral compression tests it was shown that the mechanism of energy storage prior to fracture was well approximated by a Hertzian contact law in case of glass beads, while conical contact model was required to mimic accurately the data trends measured in the presence of the non-negligible particle angularity of Q-ROK sands.

2. Considerable size-dependence of the particle strength, as well as of the energy stored in single grains at the onset of fracture was found in both classes of particles. While the size-dependent trends of highly angular Q-ROK sands were successfully captured by a surface fracture law assuming failure initiation at edge cracks, a bulk fracture model reflecting particle split in proximity of the median plane was found to explain satisfactorily the size-dependent properties of glass beads.
3. The analysis of grain size-dependent properties at the macroscopic scale displayed trends similar to those measured at the grain scale (i.e., the effect of local size dependencies was preserved in the granular continuum). In particular, the grain size-dependence of both the energy threshold for macroscopic comminution and the yielding stress at the onset of collective crushing were explained successfully through bulk fracture laws (e.g., in case of glass bead samples) and surface fracture models (e.g., in case of angular Q-ROK sands).
4. The energy-scaling factors estimated from experiments conducted at particle and assembly scale were found to fall within the range obtained by previous studies based on continuum-scale analyses and DEM simulations. While negligible variations of the scaling factors were found in glass beads of different size, stronger fluctuations were obtained in case of angular particles, thus suggesting a complex role of grain angularity on the energetics of breakage.

While the experiments conducted in this work focused on a relatively narrow interval of grain sizes and shapes (thus warranting further analyses to assess the grain-scale effects emerging from wider variations of particle geometry), they represent a starting point to disclose the link between local grain crushing and comminution, thus offering conceptual guidance for the interpretation of testing programs conducted on materials different than those explored here.

## CHAPTER 5: TIME EFFECTS ON THE COMMINATION OF SANDS

### 5.1 Introduction

The deformation of crustal solids over time plays an important role in a number of problems, from the precursory stages preceding the rupture of seismogenic faults (Becken et al., 2011) to the deterioration of the reservoir quality due to hydrocarbon production and consequent delayed subsidence (Hettinga et al., 2002). It is recognized that under upper crustal conditions micro-cracking is the main mechanism for rock deformation (Wong and Baud, 2012). Although the stress state is a leading factor of fracture initiation, pore fluids such as water are the cause of spontaneous crack extension under a constant stress, a process usually referred to as *subcritical fracture growth* (Atkinson, 1984). These mechanisms have been extensively studied in the brittle regime, i.e. under the concurrent action of tensile fracture and frictional slip (Brantut et al., 2012). However, the recent evidence for porous granular rocks reveals that a similar phenomenology is found under the predominantly compressive stresses typical of cap plasticity (Heap et al., 2015). From a microscopic standpoint, in fact, the compaction of granular solids is controlled by extensive grain-scale cracking and comminution (Baud et al., 2004), thus implying that granular rocks are also susceptible to porosity loss over time. Similar delayed deformations have been observed in unconsolidated granular materials, for which the effect of grain-bridging cement is deliberately removed to study a skeleton consisting of brittle particles (Takei et al., 2001, Sohn et al., 2017). In this context, numerous works emphasized the dependence of the rate of creep and intra-grain cracking on environmental conditions, using again subcritical crack growth as a framework for interpretation (Oldecop and Alonso, 2007, Brzesowsky et al., 2014). Despite the ability of these arguments to link conceptually particle-scale and continuum-scale processes, challenges still exist

to establish a quantitative connection. In fact, attempts of measuring in a repeatable manner the subcritical crack growth properties of grains resulted in excessive data scatter due to the high variability of individual (Lade and Karimpour, 2010), thus preventing a direct connection of the properties responsible for delayed particle failure and those quantifying macroscopic creep.

Here, it is hypothesized that the variability of the grain-scale processes involved in the delayed compaction of granular solids can be bypassed if the effect of micro-cracking is interpreted collectively, i.e. from measurements of delayed comminution in a multitude of grains. However, in order to link more explicitly the macroscopic measurements with the physics of subcritical crack growth, it is desirable that any continuum-scale variable used for interpretation and simulation purposes bears a connection with the underlying process of energy storage and release responsible for particle-scale fracture. The latter step can be regarded as critical to derive continuum theories able to provide detailed insight on the underlying micro-scale processes. With this goal in mind, the analyses presented hereafter will rely on the *Breakage Mechanics* framework (Einav, 2007a), i.e. a constitutive approach connecting the energetics of collective crushing to the evolution of the Grain Size Distribution (GSD) of a granular solid. Specifically, the analyses will use an augmented version of Breakage Mechanics recently proposed by (Zhang and Buscarnera, 2018). Such enhancement is rooted on a mathematical analogy between delayed tensile fracture (Figure 33a-c) and delayed comminution (Figure 33d-e), by which it is possible to extend the original rate-independent theory to a rate-dependent (viscous) formalism, thus obtaining a kinetic depiction of breakage evolution from which the spontaneous change of the GSD was expressed in a form similar to the classic growth kinetic theories (Rice, 1978, Maugis, 1985).

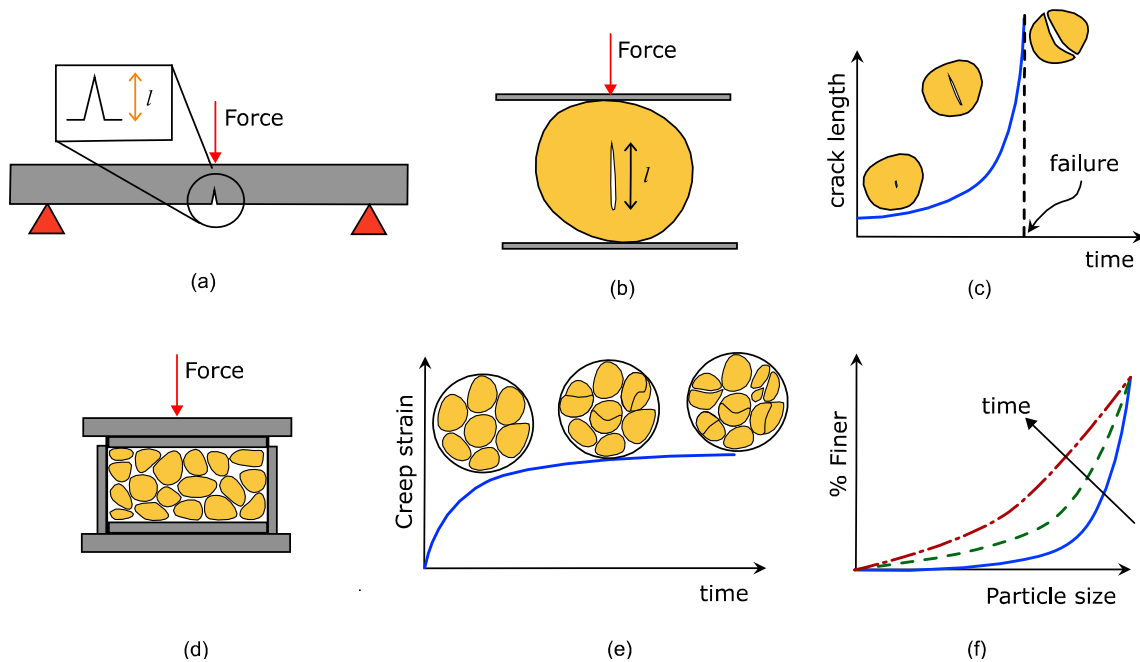


Figure 33 Schematics of (a-c) delayed fracture in brittle systems and (d-f) delayed breakage in a granular continuum; (a) typical configuration of deep-notch bending tests; (b) example of single particle crushing test; (c) propagation of pre-existing crack; (d) example of oedometric creep test; (e) creep deformation due to delayed breakage; (f) evolution of particle gradation– the percent of fine fragments increases with time.

In this chapter, a coordinated set of laboratory experiments and model simulations is presented to explore the relation between delayed particle failure and the macroscopic creep, as well as to test the ability of the abovementioned framework to replicate the measured trends of concurrent creep and breakage growth. In the following, the tools used for interpretation/simulation (Section 5.2) and the materials and methods used for laboratory testing (Section 5.3) will be described. Subsequently, the results of oedometric creep measurements will be illustrated (Section 5.4), along with the consequent stages of data interpretation and model simulation (Section 5.5).

## 5.2 Theoretical Background

The term subcritical crack growth indicates the slow and spontaneous propagation of flaws in a brittle solid at stress concentration levels lower than those responsible for instantaneous fracture. Such phenomenon has been observed in various types of rocks and is highly sensitive to factors

such as humidity and temperature (Atkinson and Meredith, 1987). Among the kinetic models for subcritical crack growth, the Charles equation (Charles, 1958) is one of the most widely used for geomaterials (Oldecop and Alonso, 2007). A similar model based on the same material constants but including a stress corrosion limit (i.e., a lower threshold of stress intensity factor below which crack growth is not possible) was proposed by Maugis (1985) and adapted by Zhang and Buscarnera (2017) to a thermodynamic formalism. Specifically, it is shown that the Maugis equation can be expressed in terms of the energy release rate, as follows:

$$\dot{l} = \dot{l}_o \left\langle \frac{G_I}{2\gamma} - 1 \right\rangle^{n/2} = \dot{l}_o \xi_c^{n/2} \quad (5.1)$$

where is  $G_I = -\partial\Psi/\partial l$  is the energy release rate (i.e., the derivative of the Helmholtz free energy potential,  $\Psi$ , with respect to the crack length,  $l$ ). The symbol  $\langle \rangle$  represents the Macaulay brackets and indicates lack of crack growth ( $\dot{l}=0$ ) below a specified energy threshold. From equation (5.1) it is readily apparent that this model uses the classic Griffith criterion (Griffith, 1921) as an initiation limit, based on which  $\gamma$  indicates the surface energy of the solid. This crack growth kinetic model can be condensed into a power law expressed in terms of a dimensionless *fracture overstress function*,  $\xi_c = G_I/2\gamma - 1$ , and two model constants (a reference crack growth velocity,  $\dot{l}_o$ , and the stress corrosion index,  $n$ , which for quartz typically range from 15 to 60; (Oldecop and Alonso, 2001, Atkinson, 1984)).

The simplicity of this model allows a mathematical analogy with crushable continua made of particles susceptible to subcritical crack growth (Zhang and Buscarnera, 2017). Such analogy can be constructed in energy terms by noting that, according to the Breakage Mechanics framework, the macroscopic yield surface for pure breakage can be expressed as follows:

$$y = \frac{E_B}{E_c} (1 - B)^2 - 1 \leq 0 \quad (5.2)$$

where  $B$  is a breakage variable reflecting the evolution of the GSD (i.e., evolving from  $B = 0$  for unbroken states to  $B = 1$  for fully comminuted states),  $E_B = -\partial\Psi/\partial B$  is the breakage energy (i.e., the elastic stored energy released upon an infinitesimal variation of GSD) and  $E_c$  is a critical energy threshold associated with collective crushing (which, as illustrated by Zhang et al. (2016), can be linked to the fracture properties of the particles).

The yield function (5.2) can be specialized by introducing a Helmholtz free energy potential,  $\Psi$ . With reference to axisymmetric conditions, a standard example is linear elasticity (Nguyen and Einav, 2009; Zhang and Buscarnera, 2017):

$$\Psi(B, \varepsilon_v^e, \varepsilon_s^e) = \frac{(1 - \mathcal{G}B)}{2} \left[ K (\varepsilon_v^e)^2 + 3G (\varepsilon_s^e)^2 \right] \quad (5.3)$$

where  $\varepsilon_v^e$  and  $\varepsilon_s^e$  are volumetric and deviatoric elastic strains, while  $K$  and  $G$  indicate the bulk and shear elastic moduli. The symbol  $\mathcal{G}$  indicates instead a statistical grading index computed on the basis of the initial and ultimate GSD (here an ultimate fractal grading is used with a power law coefficient  $\alpha=2.7$ ; (Zhang and Buscarnera, 2014)). Similarly, for pressure-dependent (nonlinear) elasticity, the Helmholtz free energy function is given by:

$$\Psi(B, \varepsilon_v^e, \varepsilon_s^e) = (1 - \mathcal{G}B) \left[ \frac{P_r}{\bar{K}(2 - m)} \Lambda^{\frac{2-m}{1-m}} + \frac{3}{2} P_r \bar{G} \Lambda^{\frac{m}{1-m}} (\varepsilon_s^e)^2 \right] \quad (5.4)$$

where  $\bar{K}$  and  $\bar{G}$  are non-dimensional elastic constants;  $m$  describes the pressure dependence of the elastic stiffness (here assumed equal to 0.33, as typical for Hertzian elasticity);  $P_r$  is a reference pressure (here assumed equal to 1 kPa) and  $\Lambda = \bar{K}(1 - m) \varepsilon_v^e + 1$ .

By starting from the yield criterion (5.2), Zhang and Buscarnera (2017) derived a simple energy-based breakage growth equation for pure comminution, which was expressed as follows:

$$\dot{B} = \dot{B}_0 \xi_B^{n/2} \quad (5.5)$$

where  $\xi_B$  is a *breakage overstress function* given by:

$$\xi_B = \left\langle \frac{E_B}{E_c} (1-B)^2 - 1 \right\rangle \quad (5.6)$$

It is readily apparent that equation (5.5) uses the violation of the breakage yield criterion (hence, the use of the term *overstress* for  $\xi_B$ ; (Perzyna, 1966)) as an initiation threshold for the evolution of the GSD, here underpinned by positive values of the breakage growth rate,  $\dot{B}$ . This establishes an analogy with equation (5.1), where crack growth is governed by a fracture initiation criterion expressed in energy terms. The analogy is completed by a power law for the breakage evolution equation (5.5), where  $\dot{B}_0$  is a reference breakage rate and  $n$  plays a role similar to the stress corrosion index.

For more realistic analyses of geomaterials exhibiting concurrent breakage and plasticity, this simplified description can be enriched through a coupled breakage-plastic dissipation formulation (Nguyen and Einav, 2009), which leads to the following yield surface:

$$y = \frac{E_B}{E_c} (1-B)^2 + \left( \frac{q}{Mp'} \right)^2 - 1 \leq 0 \quad (5.7)$$

in which  $q = \sigma'_a - \sigma'_r$  is the differential stress,  $p' = (\sigma_a + 2\sigma_r)/3$  is the mean effective confinement and  $M$  is a frictional strength coefficient. Updated inelastic flow rules can be therefore defined by introducing an augmented breakage overstress function:

$$\xi_B = \left\langle \frac{E_B}{E_c} (1-B)^2 + \left( \frac{q}{Mp'} \right)^2 - 1 \right\rangle \quad (5.8)$$

as well as by using the following evolution laws:

$$\dot{B} = \frac{\partial w}{\partial E_B} = \dot{B}_0 \cos^2 \omega \xi_B^{\xi n/2} \quad (5.9a)$$

$$\dot{\varepsilon}_v^p = \frac{\partial w}{\partial p} = \dot{B}_0 \frac{E_B}{p} \sin^2 \omega \xi_B^{\xi n/2} \quad (5.9b)$$

$$\dot{\varepsilon}_s^p = \frac{\partial w}{\partial q} = \dot{B}_0 \frac{E_c}{(1-B)^2} \frac{q}{M^2 p^2} \xi_B^{\xi n/2} \quad (5.9c)$$

where  $w$  is a flow potential, and  $\omega$  is a coupling angle linking volumetric plastic dissipation (i.e., plastic pore collapse) and breakage dissipation (i.e.,  $0^\circ \leq \omega \leq 45^\circ$  indicates prevalent breakage dissipation, whereas  $45^\circ \leq \omega \leq 90^\circ$  indicates dissipation dominated by plastic compaction).

Regardless of the specific initiation threshold, the evolution laws in (5.5) and (5.9) are consistent with the typical formalism of viscoplasticity, i.e. they imply growth of the inelastic state variables as soon as a yield criterion is violated (i.e., whenever applied stresses and stored energy are such that  $y > 0$ ). As a result, higher  $\xi_B$  implies faster breakage rate, which in a coupled model leads to concurrent breakage growth and creep strains (Figure 34). This time-dependent breakage growth equation has been tested against datasets on quartz sands reported in the literature (Zhang and Buscarnera, 2017), finding a satisfactory agreement with creep tests reported by Takei et al. (2001) and Lade and Karimpour (2015). However, due to lack of systematic measurements of time-evolving GSDs, the evaluation of the model performance was primarily focused on the stress-strain response. Therefore, this study has the purpose to test the model hypotheses with reference to the simultaneous evolution of particle gradation and creep strains.

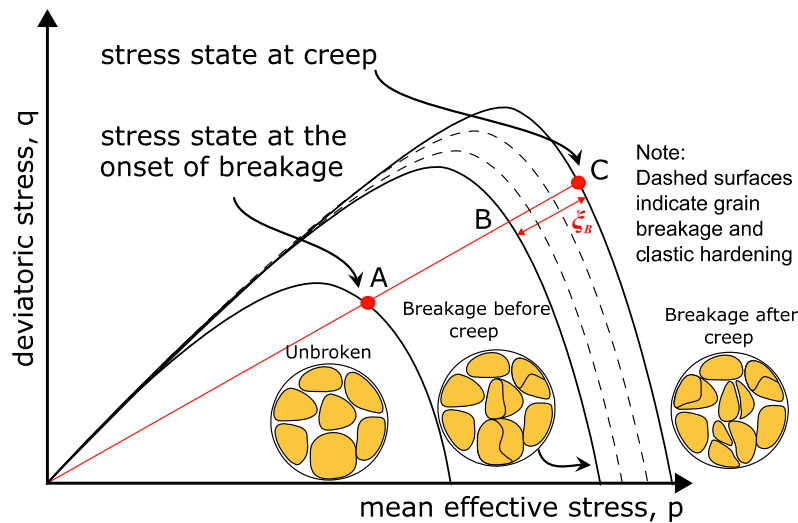


Figure 34 Schematic of breakage initiation in the  $p$ - $q$  plane. Point A indicates the first violation of the yield criterion (i.e.,  $y = 0$ ). The difference between B and C indicates the initial overstress at the onset of creep (C indicates the stress state at the onset of creep, while B marks the position of the yield surface at that same state). Dashed lines indicate gradual growth of the yield surface due to clastic hardening (i.e., delayed particle fragmentation leading to higher comminution resistance), which stops when the surface reaches point C (i.e., when both breakage growth rate and creep strain rate vanish).

### 5.3 Test Materials and Procedures

For this study, oedometric creep tests were performed on Q-ROK#1, Q-ROK#2, Q-ROK#4 and Ottawa sands by using the LoadTrac-II load frame. Material descriptions and testing procedure are described in Chapter 3.

### 5.4 Results and Data Analysis

#### 5.4.1 Measurement of concurrent creep and breakage evolution

Figure 35 shows the results of 24-hour creep tests conducted on the selected granular materials at varying vertical stress. The resulting delayed compaction (reflected by decreasing values of void ratio) was negligible at low stress levels, i.e. below the macroscopic yield stress,  $\sigma_{yield}$ , of each

material. Such yielding threshold was defined in accordance with conventional procedures based on the identification of the point of maximum curvature of the compression curve, and was found to be 26 MPa, 15 MPa, 7 MPa, and 29 MPa for Q-ROK#1, #2, #4 and Ottawa sands, respectively. Upon increasing stress (i.e., for  $\sigma_{creep} > \sigma_{yield}$ ), permanent delayed strains were observed in all specimens. Given the link between yielding and crushing in compacted granular materials (Nakata et al., 2001b, Zhang et al., 2016), this result suggests that creep was an outcome of delayed breakage resulting from sufficiently high levels of elastic stored energy within individual particles, leading to delayed grain fracture, particle rearrangement and porosity loss.

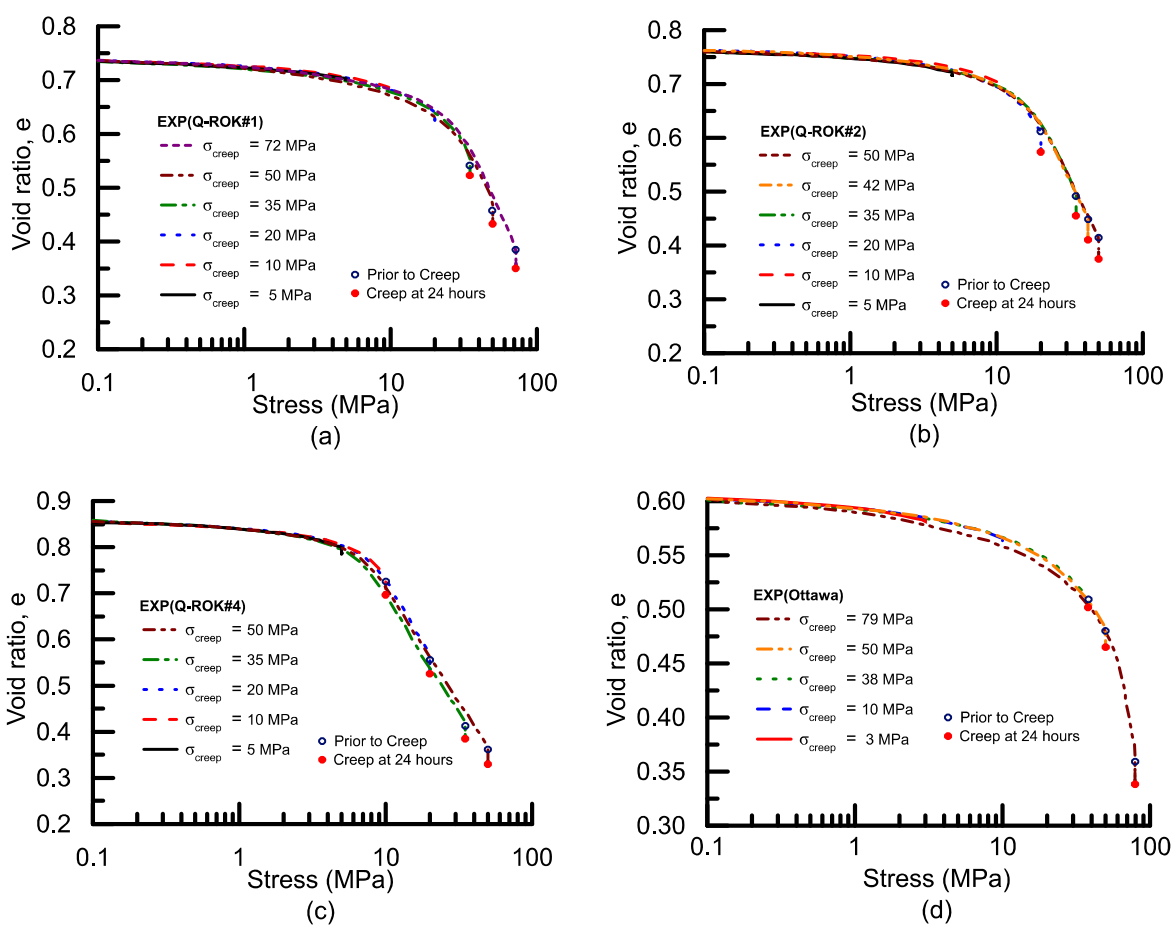


Figure 35. 24-hour creep compression for (a) Q-ROK#1, (b) Q-ROK#2, (c) Q-ROK#4, and (d) Ottawa sands at various stress levels. Open symbols indicate the initial state prior to creep. Closed symbols indicate the end of the creep test.

The concurrent accumulation of deformation and comminution was quantified by tracking the GSD at different values of elapsed creep time. Figure 37 reports the GSD curves of the tested materials here measured through sieving at the initial, pre-creep and post-creep states. The area between pre- and post-creep GSDs indicates the extent of particle breakage originated because of spontaneous grain breakage over time (Figure 36). Two normalized stress levels above the yielding stress (i.e.,  $\sigma/\sigma_y = 1.33$  and  $2.73$ ) were selected to ensure breakage at the onset of creep, as well as to assess the role of the applied stress on the accumulation of deformation over time. Figure 37 shows distinct upward shifts of the GSD curves indicating an increase of fine particles. Particularly, the alteration of the GSD curves was noticeable at  $\sigma/\sigma_y = 2.73$ , thus confirming the increase of fragments at high stress levels. After 24-hour elapsed creep time, the measured GSDs further moved upwards compared to their location prior to creep, thus indicating that delayed particle breakage was active during the elapsed time interval.

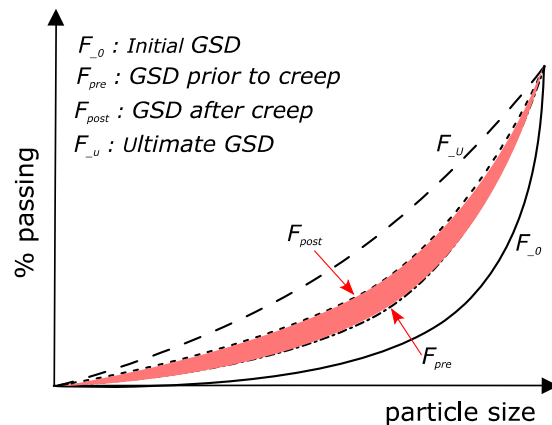


Figure 36 Graphical representation of delayed breakage growth. The shaded area represents the breakage cumulated over time.

Figure 38 quantifies the spontaneous accumulation of comminution in terms of breakage index,  $B$  (Einav, 2007a). Larger grain sizes were found to cause higher values of  $B$  (i.e., breakage was more intense in Q-ROK#4 sand than Q-ROK#2 and Q-ROK#1 because of the accentuated fragility of

coarse particles). The shape was also found to affect the magnitude and the rate of breakage, as readily apparent by comparing creep measurements in samples consisting of angular and rounded grains with similar average grain size (e.g., values of  $B$  in Q-ROK#2 sand were greater than those of rounded Ottawa sand). Such observation is consistent with those in Figure 35, where plastic volume changes displayed size- and shape-sensitivity (i.e., greater amount of volume deformation with larger or angular particles under similar stress conditions). In addition, it was observed that  $B$  in all the tested materials progressively increased with time (Figure 38). Once again, such observation suggests that delayed particle breakage is initiated above a specified stress threshold (i.e.,  $\sigma_{creep} > \sigma_{yield}$ ), eventually leading to delayed particle rearrangement.

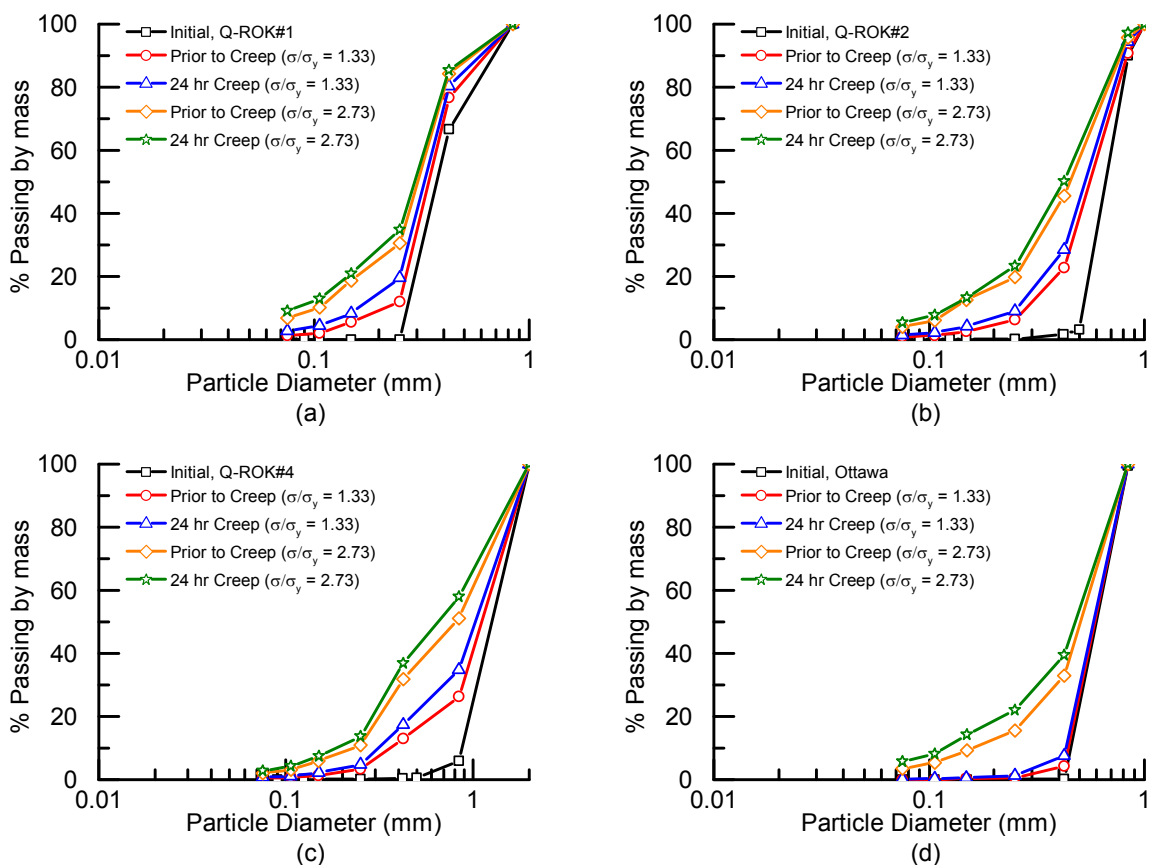


Figure 37 GSD curves measured through sieving after 24-hour creep tests at different stress levels (a) Q-ROK#1 (b) Q-ROK#2 (c) Q-ROK#4 and (d) Ottawa sands.

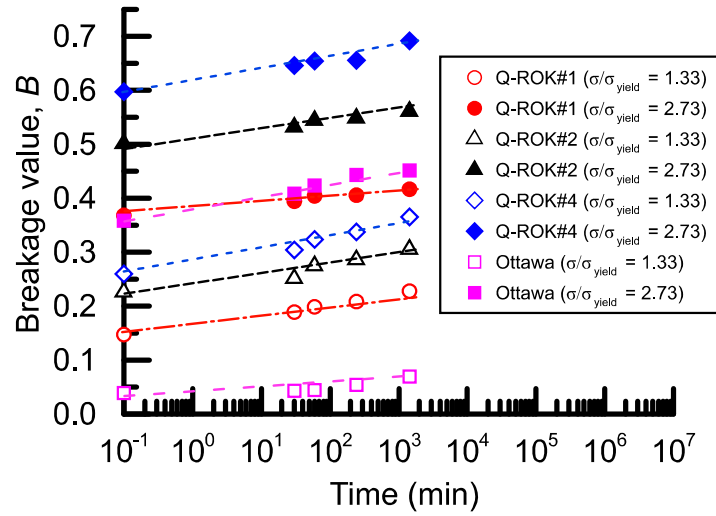


Figure 38 Evolution of breakage during creep tests at selected normalized stress levels

#### 5.4.2 Data interpretation based on the kinetics breakage theory

This section uses the breakage growth model summarized in Section 5.2 for data interpretation. This analysis is meant to identify the key features of the relation between the breakage growth rate and continuum-scale elastic stored energy, as well as to assess the degree of grain-size sensitivity of the model constants that control the rate of breakage growth. For the sake of simplicity the analysis is initially conducted by using a linear elastic formulation, i.e. by simplifying the process of elastic energy storage prior to breakage and creep. This choice allows a straightforward determination of the critical breakage energy for collective comminution under oedometric conditions, as follows:

$$E_c = \frac{\mathcal{G} \left[ \frac{(1+2k_0)}{3} \sigma_y \right]^2 \left( \frac{1}{K} + \frac{\eta_{k_0}^2}{3G} \right)}{2 \left( 1 - \frac{\eta_{k_0}^2}{M^2} \right)} \quad (5.10)$$

where  $\eta_{k_0} = 3(1 - k_0)/(1 + 2k_0)$ . In the equation above, the Poisson's ratio  $\nu$  is here assumed to be 0.30, thus having  $k_0 = \nu/(1 - \nu) = 0.43$ , a value consistent with typical results for granular materials (Yamamoto, 1996). By contrast, bulk and shear moduli  $K$  and  $G$  were estimated from standard elastic relations on the basis of the measured secant oedometric modulus up to yielding. Linear elasticity was also used to compute the breakage energy as a function of the current stress state prior to each creep stage, as follows (Zhang and Buscarnera, 2017):

$$E_B = \frac{\mathcal{G}}{2(1 - \mathcal{G}B)^2} \left[ \frac{p'^2}{K} + \frac{q^2}{3G} \right] \quad (5.11)$$

where  $p' = (1 + 2k_0)\sigma'_a/3$  and  $q = (1 - k_0)\sigma'_a$ . While the abovementioned use of linear elasticity is an approximation of the actual pre-creep response (i.e., it neglects the nonlinear evolution of  $k_0$  during radially confined compression), here it will be used to provide a first-order insight on the mechanics of delayed comminution, which will be later refined by more accurate simulations accounting for pressure-dependence and elastic nonlinearity.

Based on these considerations, Figure 39 plots a double logarithmic data of breakage growth rate for the tested granular materials, where  $\dot{B}$  is reported as a function of the breakage overstress function,  $\xi_B$ , which is calculated from equation (5.5) on the basis of (5.10) and (5.11).

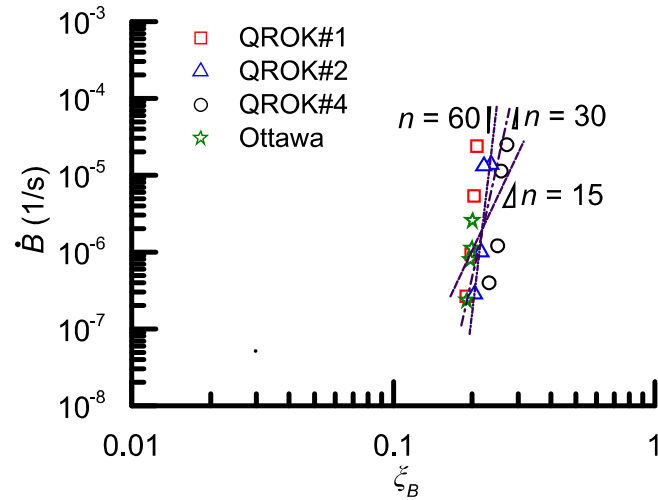


Figure 39 Plot of the breakage growth rate against the breakage overstress function for all tested sands for estimation of stress corrosion index,  $n$ . It is found that the measurements are satisfactorily fitted by the typical range of stress corrosion index reported in the literature for quartz (i.e.,  $15 \leq n \leq 60$ )

This representation resembles classic plots of subcritical crack growth velocity expressed as a function of the stress intensity factor (Charles, 1958), but is here generalized in terms of continuum variables pertaining the delayed comminution process. The magnitude of  $\dot{B}$  for each material was determined on the basis of the change of  $B$  measured between two distinct creep times, while  $\xi_B$  was computed through equation (5.8) in light of a linear elastic approximation of the breakage overstress. Figure 39 identifies some important first-order features of breakage growth. Specifically, it suggests that the measurements of breakage growth rate can be reasonably explained in terms of a power law function linking the rate of GSD evolution and the excess of elastic stored energy above the current yielding threshold. The figure also reports for illustrative purposes multiple trend lines associated with values of stress corrosion index  $n$  between 15 and 60, which cover the range typically reported for siliciclastic minerals (Atkinson, 1982). It is possible to note that the reported trend lines follow satisfactorily the cloud of data points, thus suggesting the applicability of these values also for the analysis of delayed breakage.

A similar procedure can be used to evaluate the grainsize sensitivity of the model parameters controlling rate- and time-dependence (i.e.,  $\dot{B}_o$  and  $n$ ). Also, for this purpose, linear elasticity was used. Finally, based on the estimated values of  $\zeta_B$  at each stage of creep (here once again computed on the basis of equations (5.10) and (5.11)),  $\dot{B}_o$  and  $n$  were computed by inverting equation (5.5) on the basis of measured values of breakage rate (Figure 40). Such procedure was repeated in multiple steps, by fixing alternatively either the range of the power law coefficient  $n$  (Figure 40a) or the reference breakage rate,  $\dot{B}_o$  (Figure 40b). Figure 40a reports the resulting values of  $\dot{B}_o$  for three materials characterized by similar particle shape but different size. The estimated values are reported against the particle size by assuming power law coefficients within the range usually reported for siliciclastic minerals ( $10 \leq n \leq 30$ ). The vertical error bars reflect a 68% confidence interval of the measurements, while the trendline indicates that the reference breakage growth rate estimated through this procedure decreases with an increase of the average particle size (i.e., it is grainsize dependent). By contrast, Figure 40b shows the same procedure for fixed values of  $\dot{B}_o$  within the range previously reported in light of macroscopic model calibration exercises ( $10^{-2}/s \leq \dot{B}_o \leq 10^5/s$ ). The resulting range of power law coefficient emerging from this procedure was found to be fall within the previously mentioned range (e.g., the average  $n$  associated with the error bars in Figure 40b is  $n = 22$ , which is consistent with the data points in Figure 39). Most importantly, the values estimated in Figure 40b turned not to be significantly affected by the particle size. This parametric analysis suggests that the reference breakage rate  $\dot{B}_o$  encapsulates a characteristic time of delayed comminution which varies with a characteristic internal length of the material (i.e.,  $\dot{B}_o$  needs to be adjusted for each different grain size to reflect an underlying variation of the time of individual particle breakage). By contrast, the size-independence of the power law coefficient  $n$

indicates that this parameter can be assumed as a material constant related with the stress corrosion index of the grain-forming mineral and, in lack of alternative information, possibly assumed to coincide with it. Such arguments will be used in the subsequent section, where model simulations based on the fully nonlinear and coupled breakage-plastic formulation are used to replicate the trends observed in the experiments.

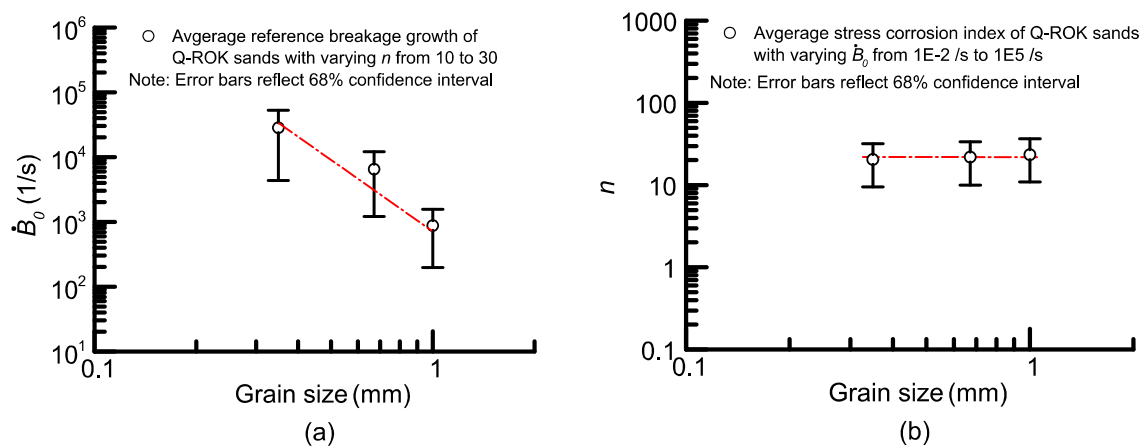


Figure 40 Parametric study assessing the grain size dependence of the model parameters  $\dot{B}_0$  and  $n$

## 5.5 Model Simulations

The breakage growth theory proposed by Zhang and Buscarnera (2017) is based on an underlying rate-independent model (Einaev, 2007b) augmented by a breakage kinetics equation resulting in a Perzyna-like overstress formulation (Perzyna, 1966). Similar to standard viscoplastic models, this approach converges to its underlying rate-independent counterpart under low deformation rates or long creep stages. As a result, a convenient two-step approach to calibrate the model parameters involves (i) the assessment of the underlying rate-independent parameters and (ii) the optimization of the remaining constants governing the creep behavior (Zhang and Buscarnera, 2017). Figure 41

summarizes the first step of this procedure by reporting the void ratios,  $e$ , at the end of the 24-hour creep measurements for all the tested sands, here used to approximate the underlying long-term rate-independent response. The continuous line represents the simulations based on a rate-independent model with the nonlinear pressure-dependent elasticity and coupled breakage-plastic dissipation (Zhang et al., 2016). The non-dimensional constants  $\bar{K}$  and  $\bar{G}$  in equation (5.4) were estimated from the first portion of the compression curves (pre-yielding behavior) and assuming a Poisson's ratio  $\nu = 0.25$ , similar to previous applications of this model to other granular materials (Zhang and Buscarnera, 2014). Finally, the stress ratio at frictional failure,  $M$ , was estimated by assuming a friction angle of  $30^\circ$  for the tested sands (Cho et al., 2006), the coupling angle,  $\omega$ , was selected to fit the post-yielding compressibility, and the critical breakage energy,  $E_c$ , was calibrated to match the yield stress. It was found that  $\omega = 15^\circ$  provides a satisfactory fit of the compression behavior of the tested sands, implying that the energy dissipation was primarily controlled by grain crushing. By contrast,  $E_c$  was found to vary with grain size and shape (i.e., for sands characterized by the same shape  $E_c$  was larger in the presence of smaller particles, while for a fixed average particle size it was larger for sands made of rounded grains; Zhang et al., (2016)).

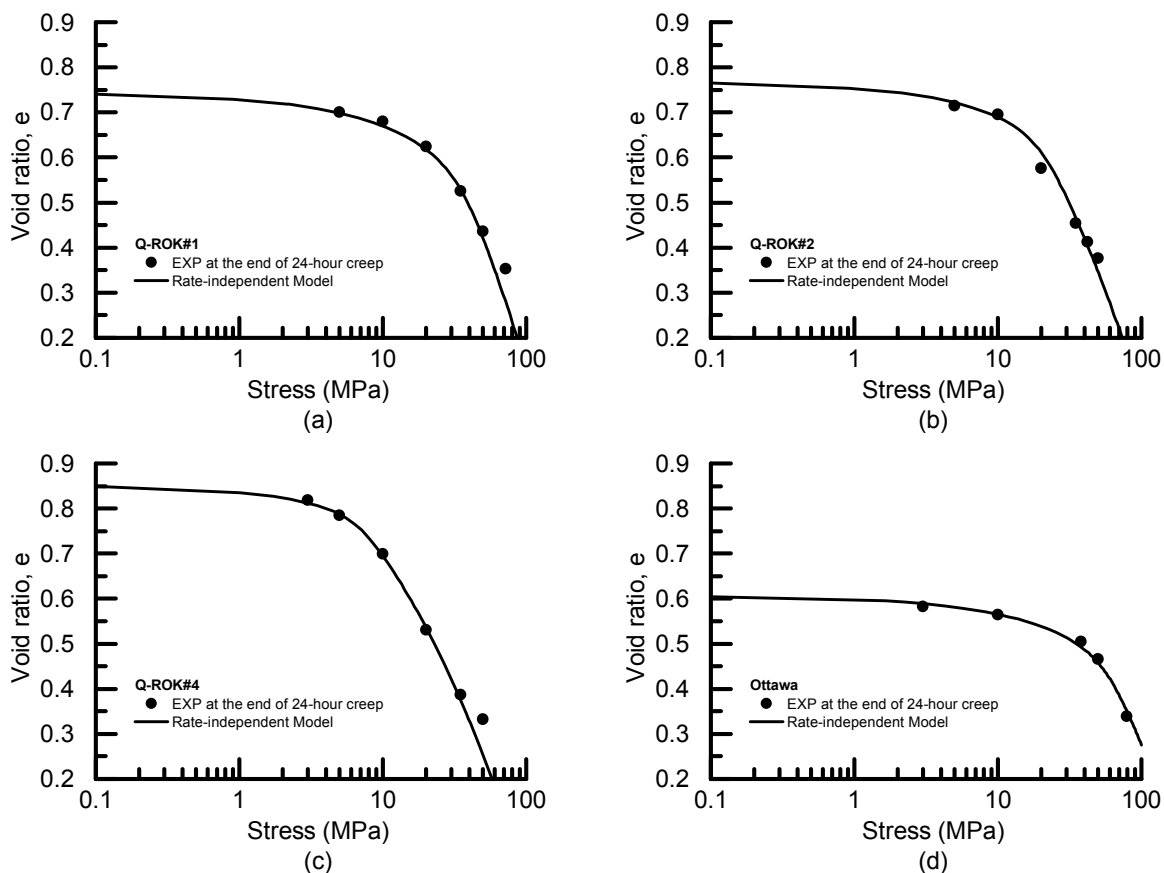


Figure 41. Measurement of 24-hour creep at various stresses with the breakage model simulations for (a) Q-ROK#1, (b) Q-ROK#2, (c) Q-ROK#4 and (d) Ottawa sand

Based on the calibrated rate-independent model parameters, creep simulations were performed. Figure 42 reports measurements of 24-hour creep deformation along with model simulations. The simulations were based on a power law coefficient  $n = 22$  for all the sands (consistently with the indications obtained from the parametric analysis in Figure 40b), while the characteristic breakage rate  $\dot{B}_0$  was optimized for each sand to account for its grain size dependence suggested by Figure 40a. Table 5 summarizes the finalized set of the continuum breakage model parameters.

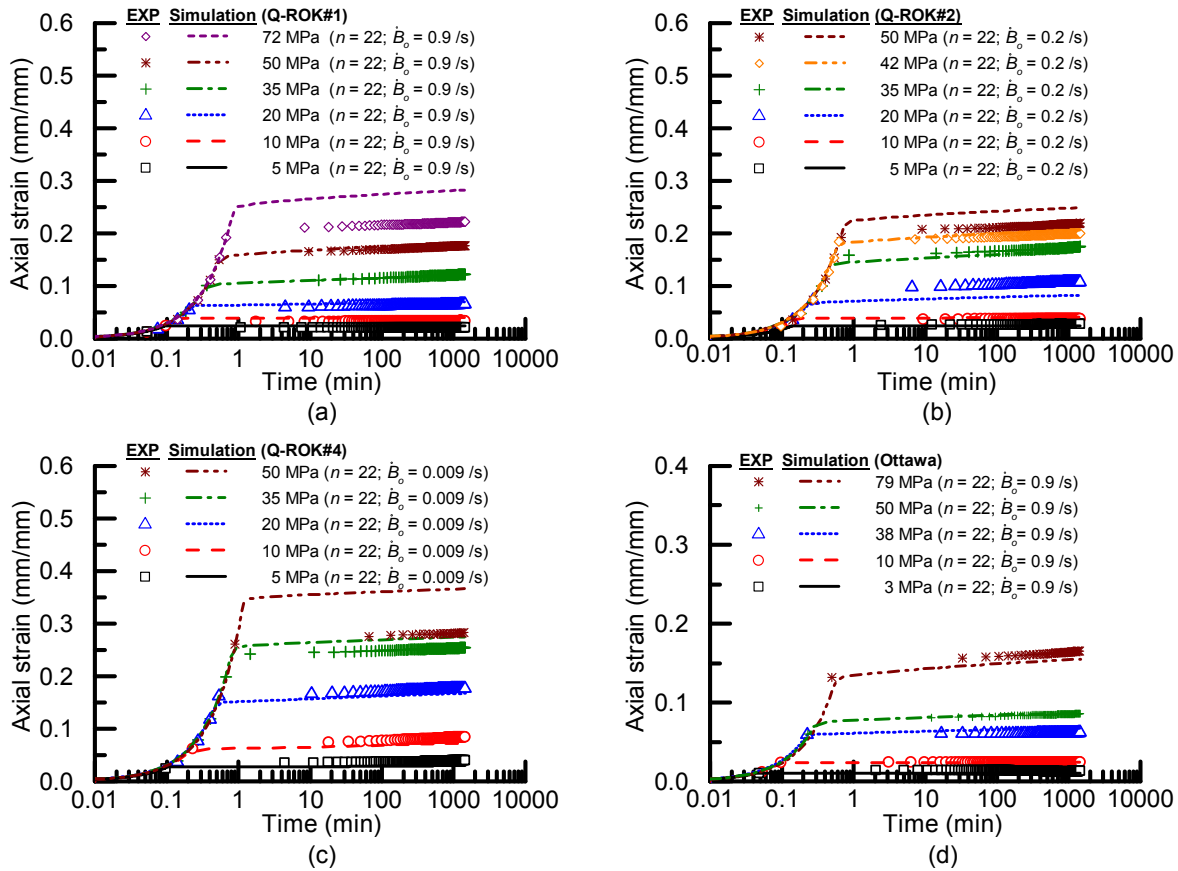


Figure 42 Measurements of 24-hour creep strains (symbols) and corresponding model simulations (lines): (a) Q-ROK#1, (b) Q-ROK#2, (c) Q-ROK#4 and (d) Ottawa sands

The simulations resulting from this procedure were in good agreement with the measurements for all considered materials and stress conditions. Particularly, both data and simulations indicated non-negligible creep at stresses beyond the reference yielding point (i.e., for  $\sigma \geq \sigma_{yield}$ ). This result corroborates the hypothesis that creep under compressive stresses is driven by delayed particle crushing and is consistent with the hypothesized connection between cap plasticity and comminution (Einav, 2007a; Zhang et al., 2016). The agreement between data and simulations also corroborates the selected value of power law coefficient  $n$ , here selected in agreement with typical values of stress corrosion index (Atkinson, 1982, Oldecop and Alonso, 2001, Zhang and Buscarnera, 2017).

Figure 44 reports the GSD of the tested sands at the end of each 24-hour creep test, while Figure 43 illustrates the corresponding the evolution of the breakage index for tests conducted at  $\sigma/\sigma_{yield} = 1.33$  and  $2.73$ . Both figures illustrate the ability of the model to replicate the changes of particle gradation occurring over time during the accumulation of creep strains. Despite the tendency of the model to overestimate the amount of breakage (i.e., the GSD curves at the end of the simulated creep time lay above their corresponding measurements), the simulations are able to successfully capture the concurrent trends of delayed comminution and deformation.

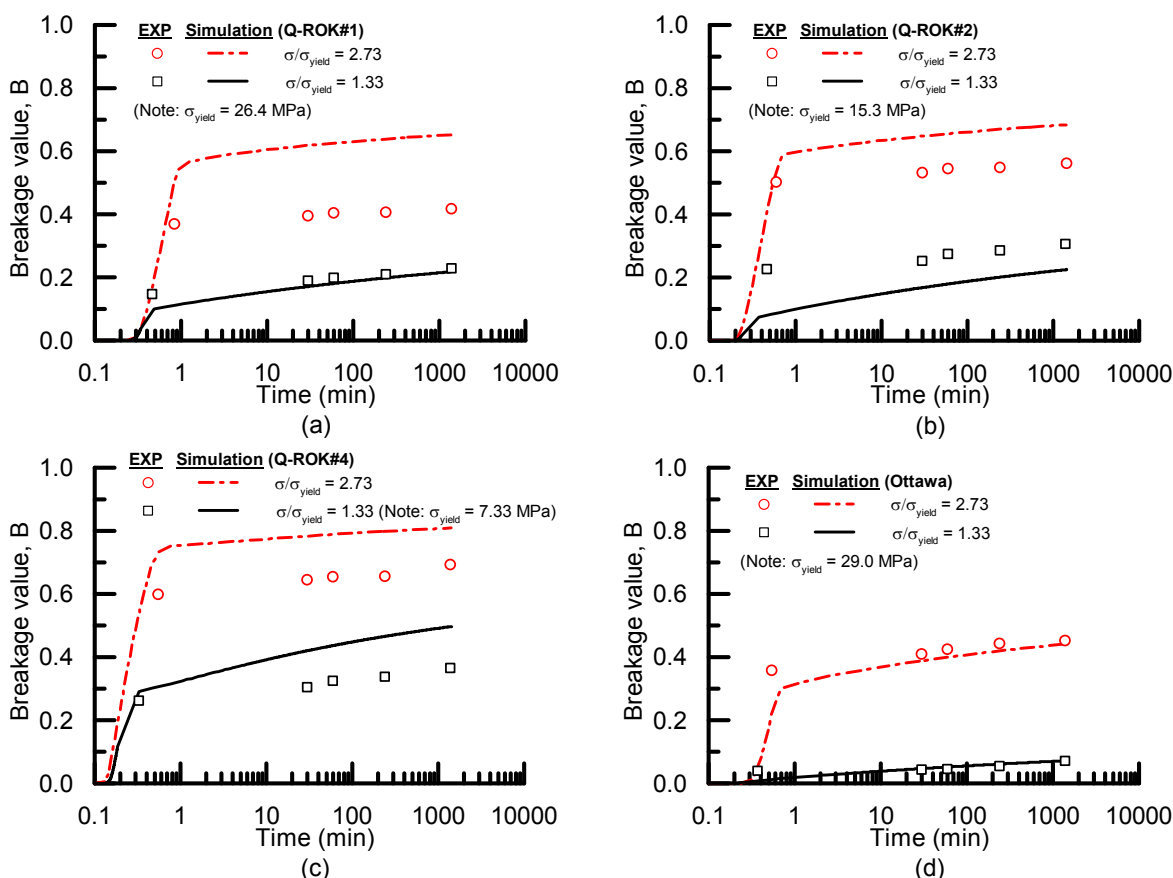


Figure 43 Measurements of the breakage value for 24-hour creep at  $\sigma/\sigma_{yield} = 1.33$  and  $2.73$  (symbols) along with the VBM simulations (lines): (a) Q-ROK#1, (b) Q-ROK#2, (c) Q-ROK#4, and (d) Ottawa sand

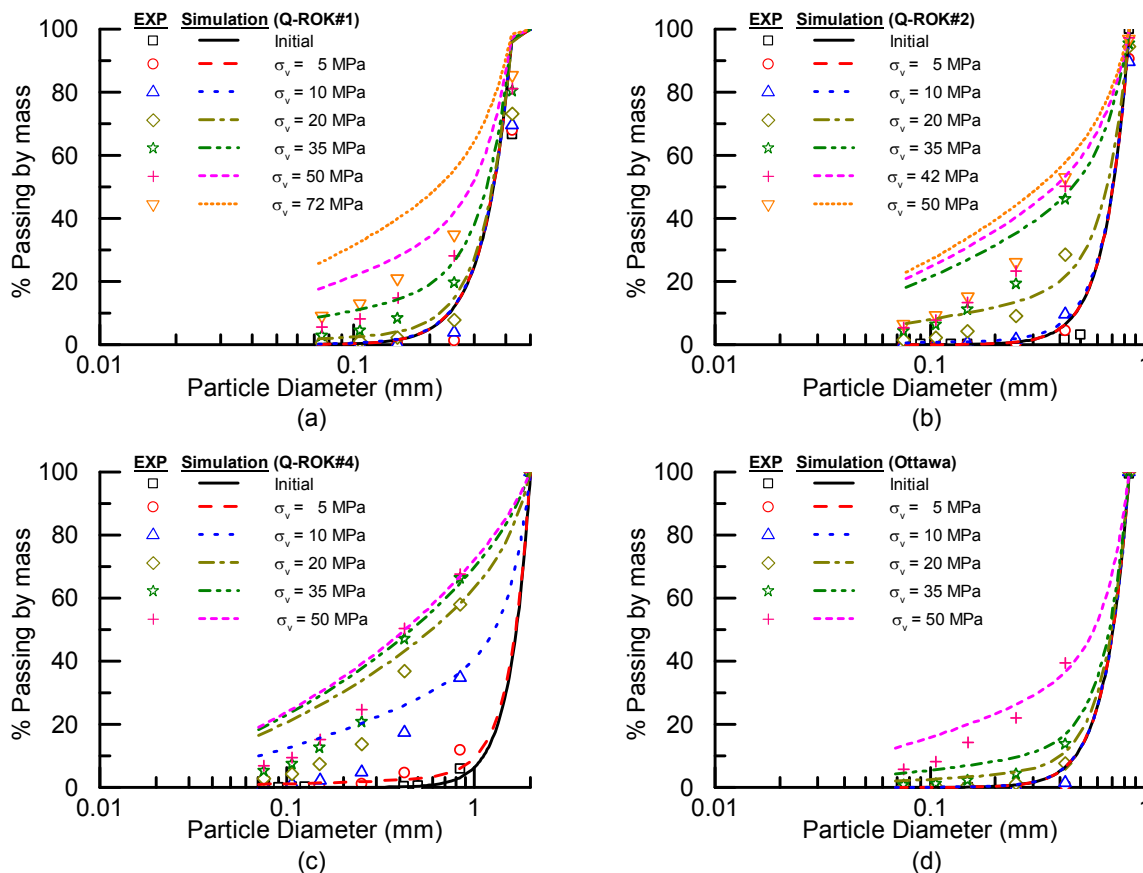


Figure 44 Evolution of particle gradation at 24-hour creep compressions (symbols) with the breakage model simulations (lines): (a) Q-ROK#1, (b) Q-ROK#2 (c) Q-ROK#4 and (d) Ottawa sands

Table 5 Summary of the viscous breakage model parameters

| Sand         | $\bar{K}$ | $\bar{G}$ | $\nu$ | $\theta$ | $w$ (°) | $M$  | $E_c$ (MPa) | $\dot{B}_0$ (1/sec) | $n$ |
|--------------|-----------|-----------|-------|----------|---------|------|-------------|---------------------|-----|
| Q-ROK#1      | 9800      | 5880      | 0.25  | 0.734    | 15      | 1.20 | 1.80        | 0.900               | 22  |
| Q-ROK#2      | 9800      | 5880      | 0.25  | 0.739    | 15      | 1.20 | 0.68        | 0.200               | 22  |
| Q-ROK#4      | 8500      | 5100      | 0.25  | 0.754    | 15      | 1.20 | 0.12        | 0.009               | 22  |
| 20/40 Ottawa | 16000     | 9600      | 0.25  | 0.734    | 15      | 1.20 | 2.50        | 0.900               | 22  |

The simulations confirm the need to adjust the value of characteristic breakage rate  $\dot{B}_0$  to account for different values of grainsize in each material. Figure 45 summarizes the grainsize dependence

of the optimized values of  $\dot{B}_o$  with respect to Q-ROK sands. The grainsize dependence is captured satisfactory by a power law function, according to which  $\dot{B}_o$  is expressed as:

$$\dot{B}_o = \dot{\bar{B}}_o \left( \frac{d_o}{d} \right)^\chi \quad (5.12)$$

where  $\dot{\bar{B}}_o$  is a reference rate,  $d_o$  is a reference grainsize and  $\chi$  is a fitting parameter. The trendline indicates decreasing values of  $\dot{B}_o$  for the larger grainsize. Since  $\dot{B}_o$  reflects the velocity of breakage growth (i.e., a larger  $\dot{B}_o$  indicates the faster comminution and consequent faster accumulation of creep strains), it determines a characteristic time of comminution process which depends on the size of the particles (i.e., it depends on an internal length scale associated with the material microstructure). Although measurements of failure time of particles embedded in a compressed granular materials are not easily accessible, this trend can be explained in light of grain-scale arguments. It is indeed arguable that, under identical local stress conditions and similar values of intra-grain crack growth velocity, larger particles require longer elapsed time to reach catastrophic failure through coalescence (i.e., until multiple micro-cracks intersect each other) or splitting (i.e., when a dominant flaw attains a length close to the particle diameter). Such characteristic breakage time,  $t_B$ , can be estimated from the inverse of  $\dot{B}_o$  (which dimensionally has units of  $s^{-1}$ ). Because  $t_B$  is inversely proportional to  $\dot{B}_o$ , a power law expression similar to equation (5.12) can be used:

$$t_B = t_B^* \left( \frac{d}{d_o} \right)^\chi \quad (5.13)$$

where  $t_B^*$  is a reference breakage time. Figure 45 reports that  $t_B$  increases with the particle sizes, thus indicating that it takes approximately 1.1 seconds for Q-ROK#1 sands to develop substantial delayed particle breakage, while Q-ROK#4 sand has a characteristic time of 111 seconds. These values should be directly connected with the actual time of failure of individual particles, in that they are reference times impacting solely the continuum behavior and resulting in durations of the creep stage which depend on the violation of the overstress function,  $\xi_B$ , and hence on the imposed stress conditions. Nevertheless, the trends in Figure 45 suggest that delayed breakage in Q-ROK#1 (characterized by finer particles, and hence shorter failure times at fixed crack propagation velocity) occurs over a shorter time frame, thus resulting in a material with weaker time-dependence. By contrast, Q-ROK#4 (characterized by larger particles, and hence longer failure times at fixed crack propagation velocity) exhibits delayed comminution and creep over a much longer time frame, thus resulting in a material with stronger time-dependence.

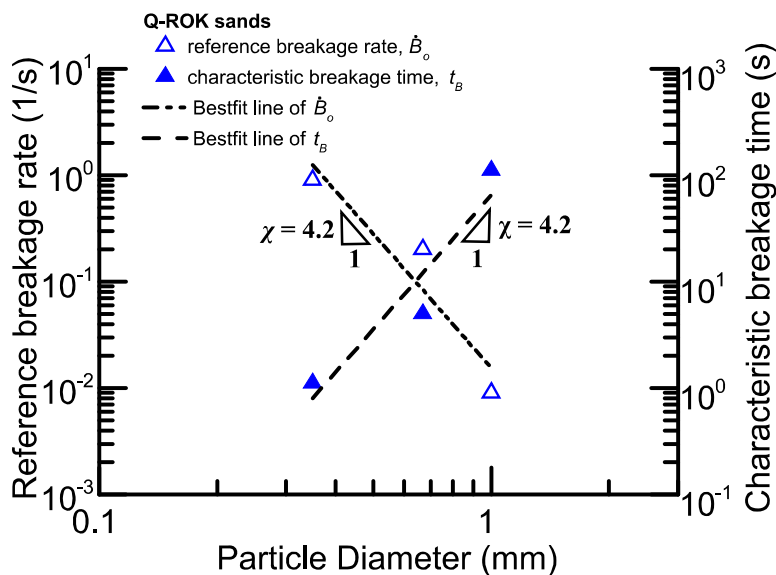


Figure 45 Measurements of the size-dependent reference breakage rate and characteristic breakage time

Another graphical strategy to quantify the rate of breakage growth is to use traditional logarithmic plots widely used in the analysis of so-called secondary compression phenomena (Mesri and Castro, 1987). This is illustrated in Figure 46, where the logarithmic delayed compression factors,  $\lambda_B$  and  $\lambda_\varepsilon$  measured from the  $B-t$  and  $\varepsilon-t$  plots are shown with reference to delayed breakage and creep strain, respectively, in a similar way to empirical secondary compression models.

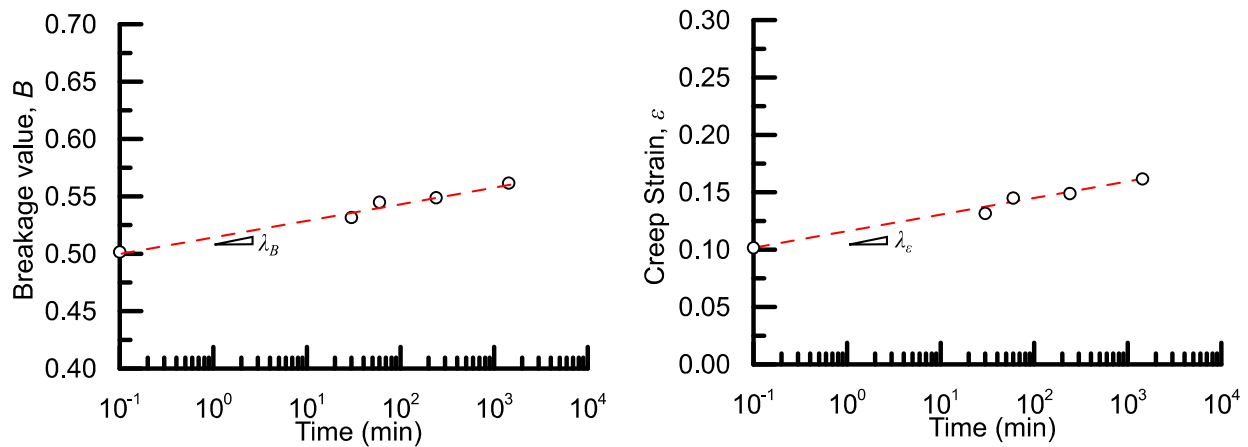


Figure 46. Illustration of logarithmic delayed deformation coefficients  $\lambda_B$  and  $\lambda_\varepsilon$  extracted from  $B$ -time and  $\varepsilon$ -time plots. These factors quantify the rates of delayed breakage growth and creep strain over time, respectively

$\lambda_B$  indicates the rate of delayed breakage during creep. Figure 47 reports a plot of  $\lambda_B$  with respect to  $\lambda_\varepsilon$ , which characterizes the rate of the accumulation of creep strain. It was found that the rates of delayed breakage growth and creep accumulation for 24-hour slightly increased with an increase particle size at both  $\sigma/\sigma_y = 1.33$  and  $2.73$ . Particularly, a noticeable variation of  $\lambda_B$  was found between smaller (Q-ROK#2) and larger grains (Q-ROK#4), showing a similar tendency with the size-sensitive reference breakage growth rates obtained from the viscous breakage model simulations (Figure 42). Such findings corroborate once again the direct relation between the rate of delayed particle crushing and the rate of creep accumulation, as well as that their rates are expected to increase with the particle size (i.e., in the presence of more fragile particles). Although

the strains appear more sensitive to changes in grain size (i.e., their value changes more passing from one soil to another), in general there is some correlation between the two indices of delayed inelasticity (i.e., larger values of  $\lambda_B$  lead to larger values of  $\lambda_\epsilon$ ).

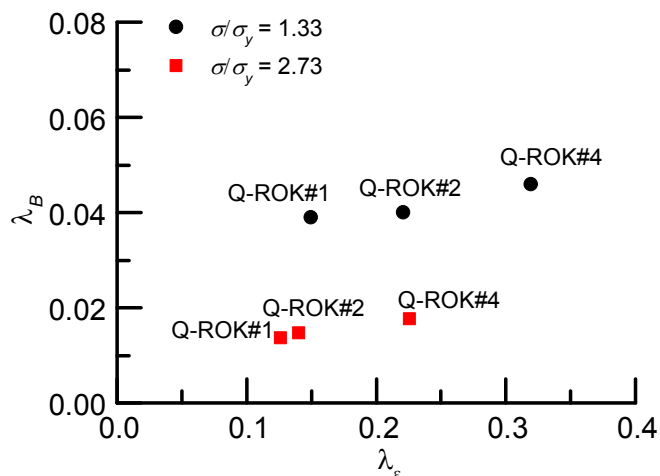


Figure 47. Comparison of the rate of creep accumulation with respect to the rate of breakage growth for all Q-ROK sands at  $\sigma/\sigma_y = 1.33$  and 2.73, exhibiting their linear size-sensitive characteristics

## 5.6 Concluding Remarks

This chapter provided a mechanical interpretation of creep in granular continua by using coordinated laboratory experiments and model simulations. Creep was hypothesized to result from subcritical crack growth in the particles constituting the material, which at the continuum level was assumed to cause delayed comminution via collective particle breakage.

Laboratory experiments on quartz sands characterized by different particle size and shape were conducted to corroborate these hypotheses. For this purpose, axial strain and grain size distribution (GSD) were tracked simultaneously as a function of stress conditions and elapsed creep time. The results revealed an evident link between grain crushing, macroscopic yielding and delayed

deformation. Specifically, while negligible variations of GSD were observed over time below the stress levels associated with collective comminution, a distinct spontaneous shift of the GSDs and delayed breakage were measured at higher stress levels. These results corroborate the hypothesis that static figure triggers local fracture of the grains, consequently contributing to the comminution and the delayed assembly deformation.

The experiments were eventually interpreted and simulated through a rate-dependent continuum model characterized by a breakage evolution law inspired by subcritical crack growth theories. The simulations showed that, similar to single crack growth, power law expressions describing the rate of breakage growth capture satisfactorily the continuum response emerging from the collective delayed fracture of the particles within an assembly. The model also allowed the assessment of the grain-size dependence of the material parameters controlling the rate of breakage. It was found that, while the characteristic time of breakage growth depends on the size of the particles (thus reflecting the longer time for crack growth to cause coalescence and splitting in bigger grains), the power law coefficient characterizing the breakage kinetic equation was essentially size independent, thus reflecting its inherent connection with the grain-forming mineral.

## CHAPTER 6: X-RAY TOMOGRAPHY FOR PARTICLE COMMINATION

### 6.1 Introduction

Granular materials play a major role in disparate fields of technology and geophysics (De Gennes, 1999, Jaeger and Nagel, 1996). A challenge concerning the mechanics of particulate geophysical materials is their response to the extreme pressures acting in the lithosphere. At high pressures, the micromechanics of granular matter is controlled by the particle strength, as well as by distributed crushing events leading to grain rearrangement. Numerous studies showed that grain-scale fracture controls the compaction of rocks during the early stages of burial (Antonellini et al., 1994, Chester et al., 2004), thus affecting the porosity and permeability of sedimentary basins (Chuhan et al., 2003). Confined comminution is crucial also for the physics of fault gouges, where rocks undergo healing/granulation cycles during which they disintegrate into individual constituents that further fragment during slip (Ben-Zion and Sammis, 2003, Marone et al., 1995, Tenthorey et al., 2003). Over the last decades much attention has been devoted to the characterization of granular solids through grain-scale imaging and multiscale models (Baud et al., 2000, Coop et al., 2004, Karner et al., 2003, Zhao and Song, 2015). X-ray microtomography has allowed the characterization of particle morphology, contacts and kinematics (Alshibli et al., 2013, Andò et al., 2012). In the context of grain crushing, experimental and theoretical works explored breakage at particle and assembly scales. At particle scale, Zhao et al. (2015) showed that high-resolution imaging allows identifying fracture initiation in single grains and quantifying the patterns of fragmentation under diametric compression. This remarkable accuracy in mapping local patterns, however, came at the cost of losing the collective mechanisms typical of packed systems. Further insight has been recently gained by assembly-scale experiments with concurrent synchrotron X-ray

microtomography (SMT) and 3D X-ray diffraction analyses (Hurley et al., 2018). It was found that stresses in grains prior to fracture vary widely across the sample, as well as that fractured grains experience forces statistically higher than those of intact grains. Despite these benefits, the use of spherical particles did not allow the effect of the initial grain shape to be explored. The latter feature can in fact alter profoundly a failure at particle scale, as is often pointed out by fracture mechanics principles (Shipway and Hutchings, 1993, Yashima et al., 1987, Zhang et al., 1990). In this context, studies by Brzesowsky et al., (2011; 2014) used Hertzian fracture to examine the link between particle strength and the size of their flaws. Zhang et al. (2016) adopted a similar strategy to derive scaling relations linking the grain-scale fracture properties to an energy threshold for comminution. Solutions for bulk fracture, contact fracture and Weibull weakest-link theory were derived to explain data at both grain and assembly scales. Following this line of inquiry, Sohn et al. (2017) performed parallel experiments in materials characterized by spherical and angular particle shape. The tests displayed similar degrees of grain-size-sensitivity in grains and assemblies, which were controlled by the shape of the grains and could be explained through shape-dependent contact laws. However, given the macroscopic nature of the experiments, direct visualization of the fracture patterns could not be achieved, thus requiring an explicit validation of the predictions. This chapter aims to fill this gap by using a concurrent characterization of compression response and grain fracture patterns within packed granular samples, as well as by providing quantitative insight about the evolution of the particle morphology during confined comminution. For this purpose, two quartz sands of different shape characteristics have been subjected to oedometric compression within a miniaturized testing setup. Initial and evolving particle morphology were tracked via 3D SMT, with the goal to identify indices associated with the mode of grain failure

which can facilitate the assessment of local fracture processes, as well as the validation of multi-scale grain-breakage theories for geophysical materials.

In addition, time effects play also a crucial role in local grain crushing mechanisms, which in turn impacts significantly the creep deformations in granular materials. To address the time-dependent behavior of granular materials, this chapter also includes evidences collected at the micro-scale, showing that breakage-induced deformations develop over time through mechanisms involving the delayed propagation of intra-granular cracks and gradual transfer of stresses across the skeleton. For this purpose, four granular soils with different particle size and shape characteristics have been used, while 3D X-ray microtomography has been employed to collect grain-scale data regarding the influence of the particle size and morphology on delayed breakage. Finally, the results of the study establish a connection between the rate of continuum breakage growth and the rate of creep strains by comparing microscopic and macroscopic results.

## **6.2 Synchrotron X-ray Microtomography**

### *6.2.1 Imaging facility at Argonne National Laboratory, IL USA*

In-situ X-ray microtomography is a non-destructive visualization technique that enables to directly disclose the internal structure of a specimen during testing. In this study, microtomography images have been acquired at either DNDCAT (Sector 5-BM-C) or GeoSoilEnviroCARS (Sector 13-BM-D) of the Advanced Photon Source (APS) in Argonne National Laboratory, Illinois, USA. Both facilities are capable to provide a high energy X-ray beam, ranging from 10 to 42 keV (5-BM-C) and 4.5 to 80keV (13-BM-D). Generally, a prepared specimen is positioned between the incoming X-ray beam source and charge coupled device (CCD)-based imaging detector system. Prior to initiating the scan, settings of the energy adsorption level, storage directory for the collection of

3D datasets, start/stop angles, angular increment, pixel size, and exposure time are necessarily defined. As the scan begins, the X-ray microtomography beam source starts to travel and penetrate the sample. Typically, the 3D distribution of microscopic constituents (e.g., solid phase and pores) can be imaged accurately at an energy level between 25 to 40 keV. A scintillator is then used to convert the transmitted and attenuated X-rays into visible light, enabling a CCD camera to record the radiographs. During illumination, the sample rotates about an axis perpendicular to incident beam through a given start/stop angle (e.g., 0 to 180°) with a given angular increment (e.g., 0.1° to 0.25°) per projection. After the scan is completed, the collections of raw tomography images have to be pre-processed and then reconstructed through an Interactive Data Language (IDL) software to obtain the 3D spatial distribution map of the X-ray attenuation of the sample that is composed of multiple stacks of 2D slices.

### *6.2.2 SMT imaging for oedometer tests*

For this study, angular Q-ROK#2 sand and round Ottawa sand were used. The material descriptions and testing procedure details are described in Chapter 3. Figure 48 illustrates a typical test setup of the miniaturized test cell mounted on the testing stage in the beamline 13-BM-D GeoSoilEnviroCARS (GSECARS) microtomography facility in the APS, Argonne National Laboratory in Illinois, USA in which SMT images were acquired. The scans were carried out by using pink beam microtomography with an exposure time of 0.008 seconds. Unlike monochromatic beams, which transmit a narrow band of radiation source from available wavelengths, this technology implies that the beam is reflected from a grazing incidence mirror, thus providing large energy bandwidth, as well as instant 3D data collection (Rivers, 2016). For this study, 1.5 mrad grazing incidence angle with 1 mm of Titanium filter was selected to ensure

optimum contrast, thus having an approximate pink beam bandwidth of 40 keV. During illumination, the sample was rotated 180° with angular increments of 0.1° per projection, resulting in the collection of 1800 radiographs. The spatial resolution of the images was 4.28 μm per pixel, which allowed the identification of fine-scale features.

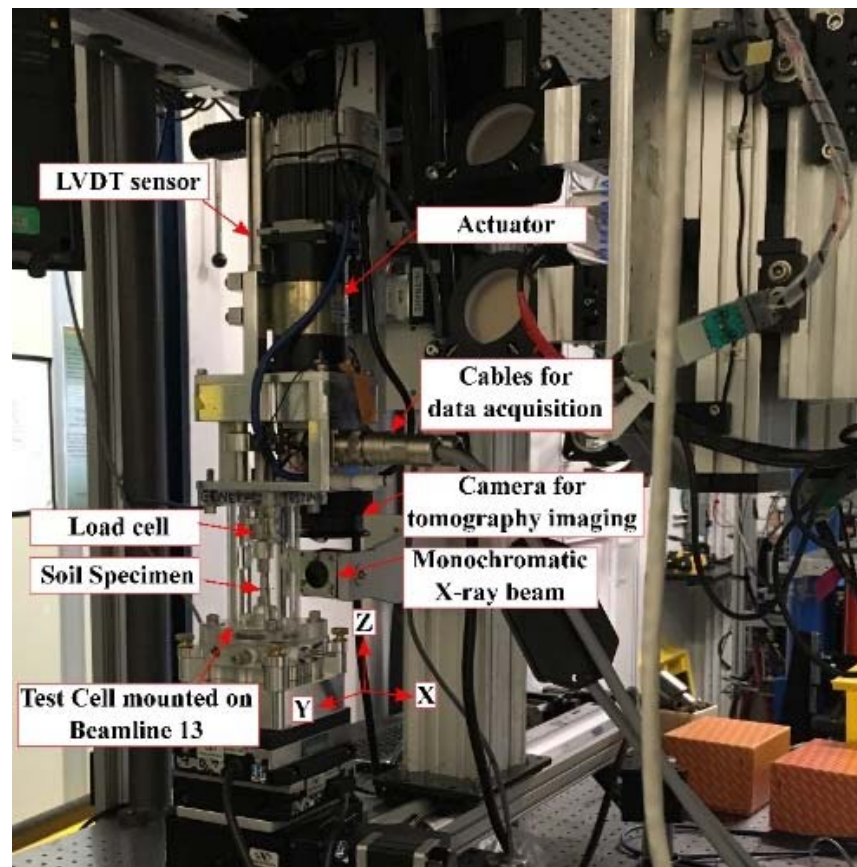


Figure 48. X-ray microtomography setup at GSECARS 13-BM-D, APS, Argonne National Laboratory

SMT images were first acquired prior to loading. After the initial scan, oedometric compression was applied at a constant displacement rate of 0.05 mm/min while preventing radial deformation. Loading was interrupted at selected stress levels and SMT scans were conducted after waiting 10 minutes for stabilization of the axial load while the loading piston was kept in place. The stress levels at which scans were conducted are given in terms of normalized stress ratios  $\sigma/\sigma_y = 0.50$ ,

1.00, 1.33, 1.66 and 2.00 for both Q-ROK#2 sand and Ottawa sand, where  $\sigma$  is the applied stress and  $\sigma_y$  is the reference comminution pressure for the considered materials (Figure 49), i.e. the stress at which distributed crushing leads to an increase of macroscopic compressibility (often referred to as a yield stress). The reference yield stress of Q-ROK#2 and Ottawa sands was found to be 15 MPa and 29 MPa, respectively, both determined in accordance with conventional soil mechanics procedures based on the identification of the point of maximum curvature in the compression curve (Pestana and Whittle, 1995). The selected range of normalized stresses was sufficiently high to generate pervasive crushing in both sands, thus comparing their local grain fracture patterns.

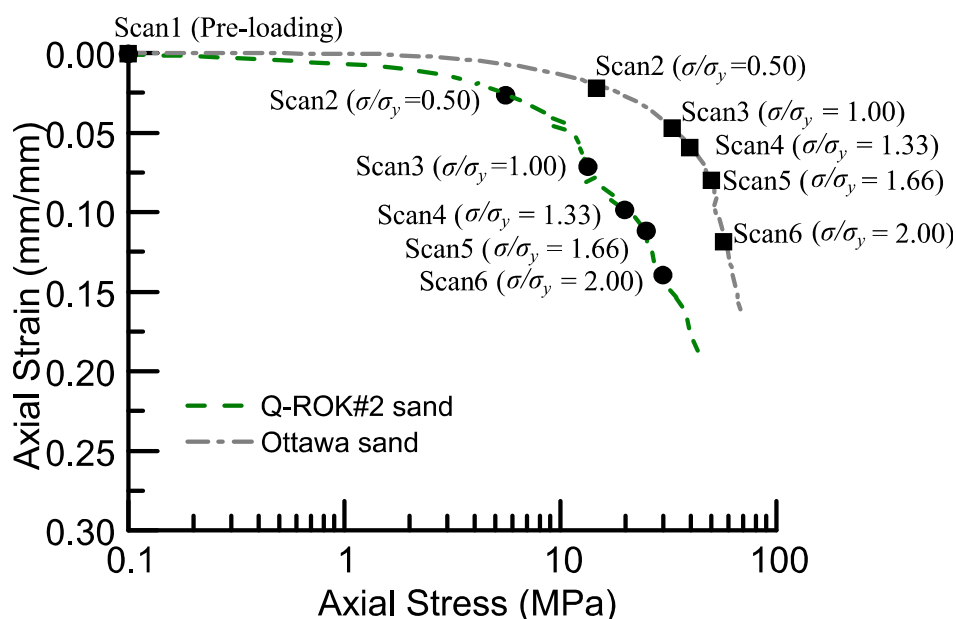


Figure 49. SMT scans performed at selected stress states during oedometer tests on Q-ROK#2 and Ottawa sands

### 6.2.3 SMT imaging for 24-hour Creep

For creep tests, Q-ROK#1, #2, and #4 sands and Ottawa sand were used. The material descriptions and testing procedure details are described in Chapter 3. Figure 50 illustrates a typical test setup of the miniaturized test cell mounted on the testing stage in the beamline 5-BM-C, DNDCAT microtomography facility in the APS, Argonne National Laboratory in Illinois, USA in which

SMT images were acquired. The beamline 5-BM-C also provides a high-quality X-ray microtomography facility for direct analyses on the small-scale specimen. The scans were carried out by using a monochromator with an exposure time of 2.5 seconds. A monochromator transmits a narrow band of radiation source from available lengths, thus providing an enhanced image resolution. During illumination, the sample was rotated 180° with angular increments of 0.12° per projection, resulting in the collection of 1500 radiographs per scan. The spatial resolution of the SMT images was 6.0  $\mu\text{m}$  per pixel, which enabled to capture fine-scale features in particles and fragments.

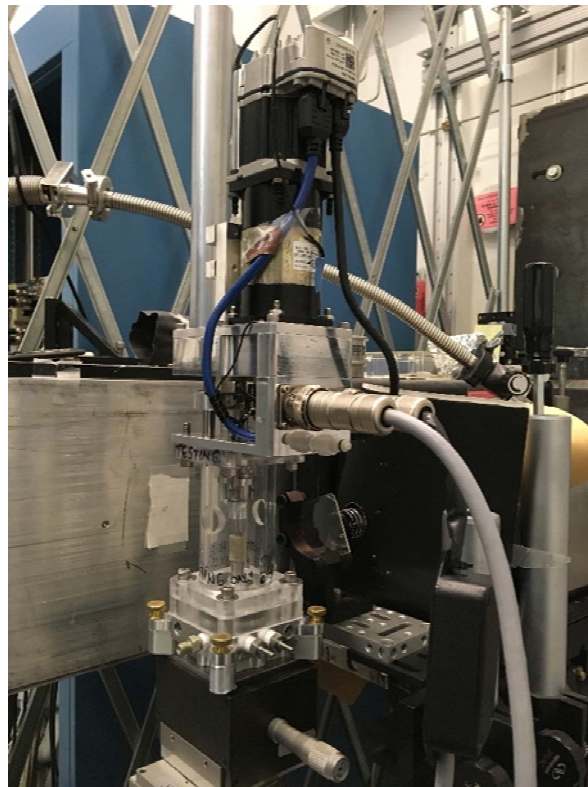


Figure 50. X-ray microtomography setup at DND-CAT 5-BM-C of the APS, Argonne National Laboratory

Initially, SMT images of the specimen were acquired prior to the application of any load. After the initial scan, oedometric compression was applied to  $\sigma/\sigma_y = 1.33$  at a constant strain rate of 0.022

mm/sec while preventing a radial strain. The yield stresses of Q-ROK#1, 2, 4 and Ottawa sands were found to be 26, 15, 7 and 29 MPa, respectively. The second scan was performed at the end of compression after waiting 10 minutes for stabilization of the axial load while the load piston was kept in place. Then, the creep experiment started by switching from strain-control to load-control mode at the given stress state, and creep displacements were measured for 24-hour (Figure 51). The constant loading was interrupted at selected creep times, 30, 60, 240 and 1440 minutes for scanning all testing sands. Since the significant creep deformation occurred during the first 24-hour (Brzesowsky et al., 2014), the selected times were sufficient to display breakage-induced accumulation of creep strains.

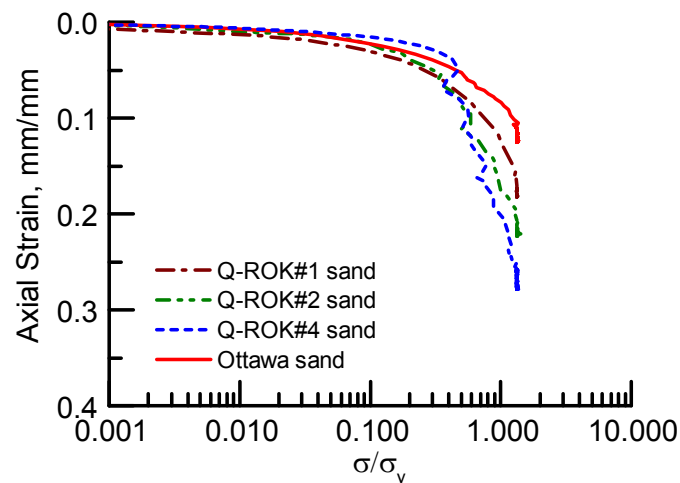


Figure 51. 24-hour oedometric creep compression curves for Q-ROK#1, #2, #4 sands and Ottawa sand

### 6.3 Analyses of SMT Images

After completion of the SMT scans, the raw tomography data were pre-processed and reconstructed through the IDL software (Rivers, 2012), including the correction for dark and white fields of raw radiographs. The reconstructed 3D images were then post-processed through the

Avizo software. The void spaces around the container and boundaries were removed from the images to minimize the data size and expedite the analyses. Most importantly, filtering, binarization, segmentation and labeling were applied to enable the quantitative analysis of the evolving microstructural properties (Figure 52). Each image was subjected to a smoothing process via the built-in anisotropic diffusion algorithm of Avizo (Bernard et al., 2011, Cil et al., 2017), thus reducing image noise and improving phase contrast at grain boundaries. Binarization was the next step for segmenting the filtered images into solid matrix and pore phase through interactive thresholding. The built-in remove-island tool was then implemented to eliminate local noise in the processed binary images. The individual particles were finally separated and identified through a watershed-based algorithm. Lastly, the sand grains were individually labeled with unique index numbers.

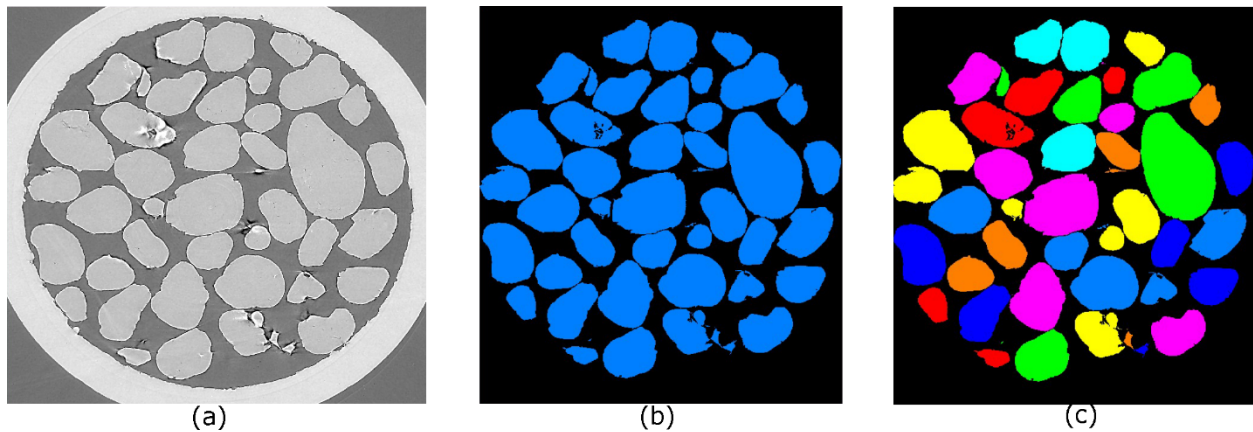


Figure 52. Example of post-processing a reconstructed X-ray microtomography image via Aivzo: (a) filtering; (b) thresholding and separation; (c) labeling of Ottawa sand

## 6.4 Results and Data Interpretation

### 6.4.1 Validation of post-processed SMT image analyses

Figure 53 reports the GSD curves of Ottawa sand prior to loading ( $\sigma_v = 0\text{MPa}$ ) and at the end of the experiment ( $\sigma_v = 80\text{MPa}$ ), both obtained from sieve analyses and post-processed SMT image

analyses. At the initial stage, the GSDs obtained from two different measurement techniques were nearly identical, indicating that image processing could generate consistent index properties of Ottawa sand which was obtained from sieve analysis. The comparison is satisfactory also at the end of the test, despite the small discrepancies at the tail of the GSD possibly due to the increase of finer materials, making more complex in particle sorting. This result signals differences in the crushing test between micro- and macro-scale. In any case, the comparison is satisfactory in that it displays similar trends and comparable measurements. This implies that whatever is the difference between micro- and macro-test, it has to be small.

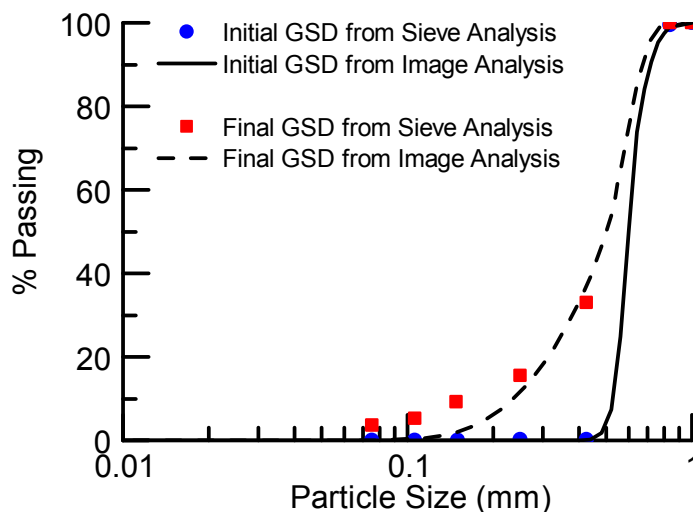


Figure 53. Grain size distribution (GSD) curves at preloading ( $\sigma_v = 0\text{MPa}$ ) and final loading ( $\sigma_v = 80\text{MPa}$ ) during the oedometric compression tests obtained through sieve analyses (symbol) and tomography image analyses (lines) techniques

#### 6.4.2 Effect of particle shape on soil crushability

Figure 49 shows the oedometric compression curves of angular Q-ROK#2 and round Ottawa sands. As is readily apparent, Ottawa sand has a slightly stiffer elastic response (i.e., less volume change prior to yielding) and higher yield stress than Q-ROK#2 sand. This is in agreement with other

studies which showed that specimens consisting of rounded particles tend to exhibit comminution at higher pressures compared to their angular counterparts (Cavarretta et al., 2017, Nakata et al., 2001b). Since particle size and mineral constituents of the two sands are similar, this result confirms that the grain morphology is the primary factor in differentiating their deformation response.

#### 6.4.3 *Impact of initial particle shape on the evolution of fragments*

The three-dimensional particle morphology can be assessed in terms of sphericity ( $S$ ) and flatness-elongation (FE) ratio (Komba et al., 2013, Lin and Miller, 2005). Sphericity describes the resemblance of an object to a sphere and varies from 0 (i.e., very angular) to 1 (i.e., spherical). It is defined as the surface area encircling a volume,  $V$ , of a sphere divided by the surface area,  $A$  of the 3D entity (Wadell, 1935):

$$S = \frac{\sqrt[3]{36\pi V^2}}{A} \quad (6.1)$$

The FE ratio reflects instead the geometry of an object in terms of the ratio between its longest and shortest linear dimensions. Hence, an increase of the FE ratio signals particles that become flatter and more elongated (Komba et al., 2013). The FE ratio is defined as:

$$FE = \frac{d_L}{d_s} \quad (6.2)$$

where  $d_s$  and  $d_L$  are the shortest and longest lengths of the grain. Figure 54 illustrates the evolution of the particle shape characteristics of the tested sands assessed on the basis of the collected SMT images.

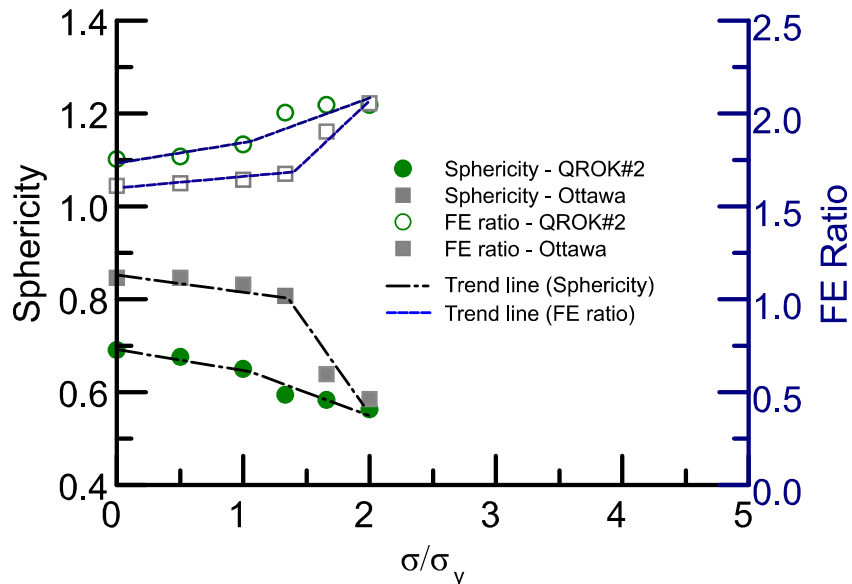


Figure 54. Evolution of the average 3D shape parameters of the tested sands during oedometric compression.

Both sands lose sphericity upon loading due to progressive particle breakage. It is also interesting to note that both Q-ROK#2 and Ottawa sands exhibited noticeable changes in morphological characteristics shortly after their yielding point. In particular, Ottawa sand displayed a sharper alteration in morphological characteristics than Q-ROK#2 sand at similar stresses, thus implying that initially round particles undergo more dramatic shape alterations compared to their angular counterparts. Most notably, at the end of the test the value of  $S$  for Ottawa sand approaches that measured for Q-ROK#2 sand, thus implying that the initial differences in grain shape tend to disappear upon continuous particle breakage. Furthermore, the FE ratio of both sands increases with loading, thus suggesting that the particles become flatter and more elongated. These results, here based on 3D SMT images, are consistent with earlier findings of Altuhafi and Coop (2011), who documented the alteration of particle shapes via 2D microscopy. Such direct visualization of the 3D microstructure therefore indicates that the ultimate morphology of intensely crushed particles tends to reach limiting values that do not depend on the shape of the particles prior to

loading, thus suggesting the possible existence of an attractor for the average grain shape of comminuted granular media (Ueda et al., 2013).

#### 6.4.4 Quantification of particle failure mode

Figure 55-56 show vertical cross-sectional grayscale images extracted from 3D SMT volume files, which display the evolution of local particle breakage in Q-ROK#2 and Ottawa sands at selected stress levels. The images confirm that Q-ROK#2 particles experienced more severe damage than Ottawa sand at similar stress conditions.

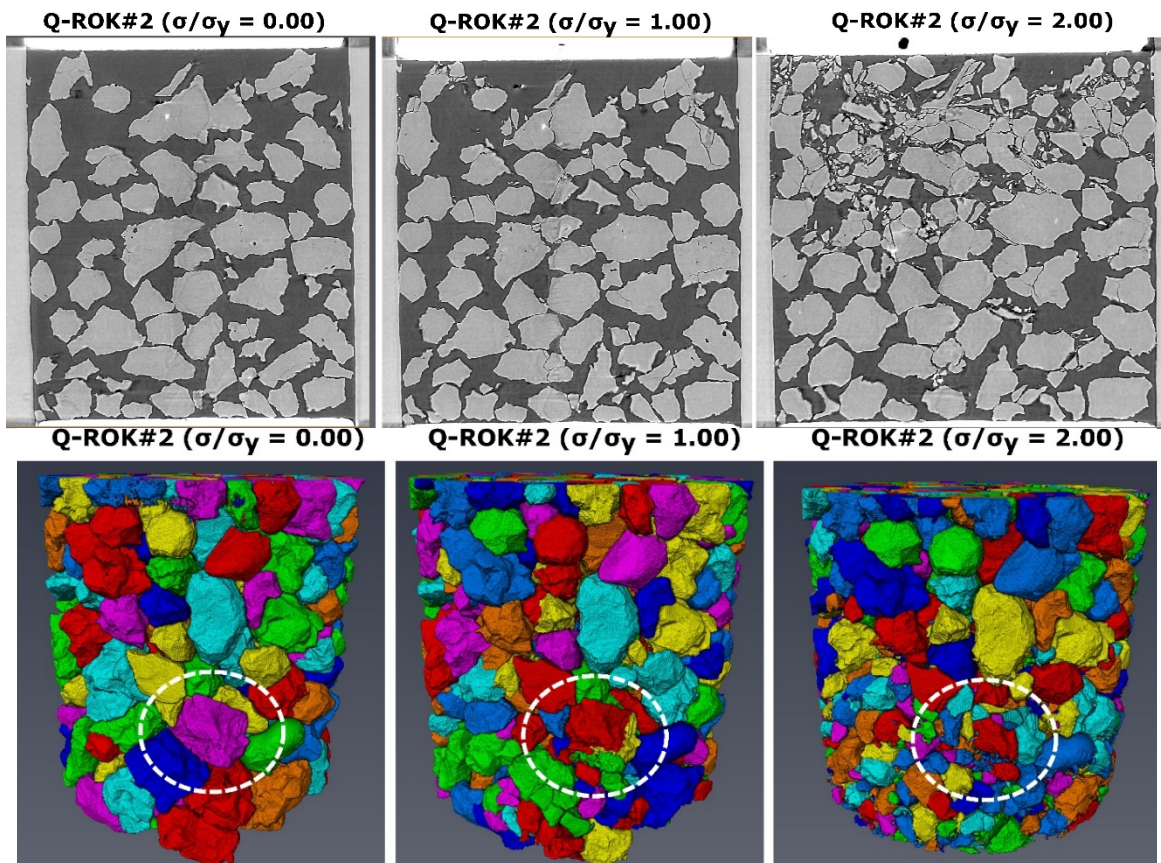


Figure 55. Grayscale vertical cross-sections (top row) from 3D SMT images of Q-ROK#2 sand with 3D renderings (bottom row) exhibiting shape-dependency of local grain failure (i.e., initially angular particles were broken into multiple fragments at the onset of crushing due to surface fracture)

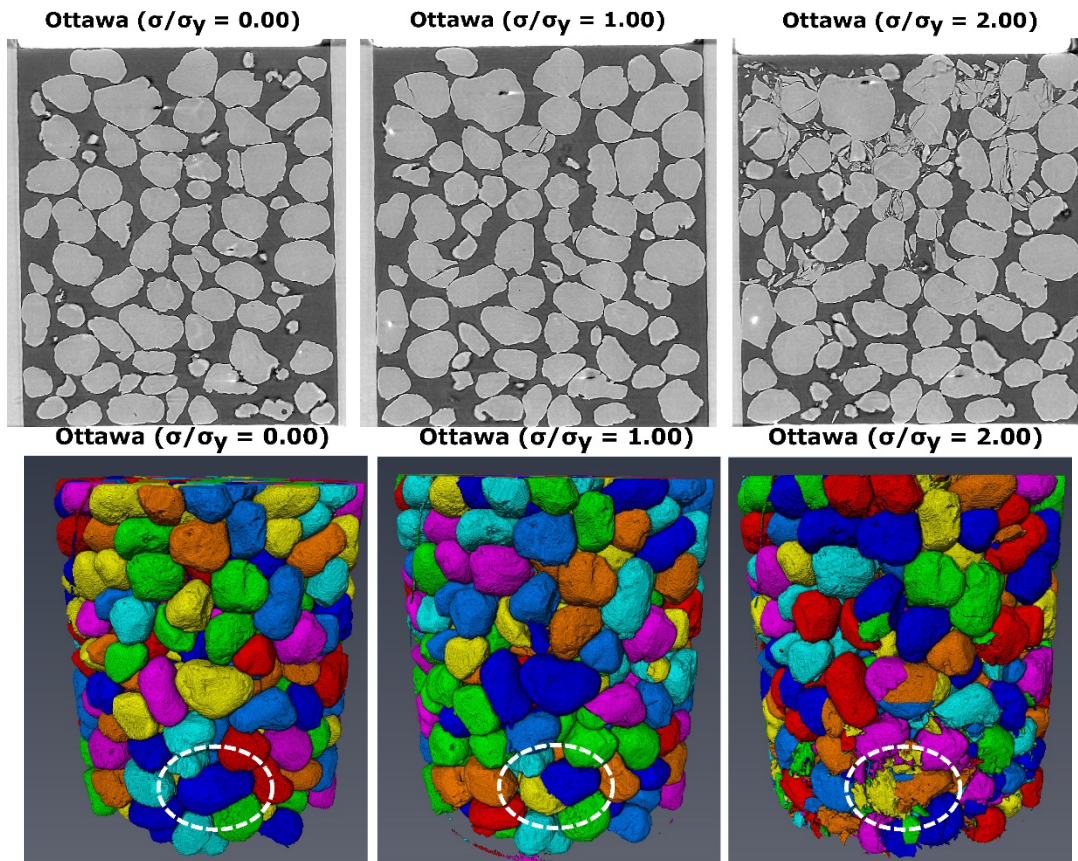


Figure 56. Grayscale vertical cross-sections (top row) from 3D SMT images of Ottawa sand with 3D renderings (bottom row), exhibiting shape-dependency of local grain failure (i.e., initially rounded particles tend to split into two at the onset of crushing and then crumble at higher pressures)

Figure 57-58 also show that both the continuum breakage index  $B$  (Einav, 2007a) and the percent fragmented particles of Q-ROK#2 sand are higher than those of Ottawa sand at comparable stresses, eventually converging to similar values upon continuous loading. Additionally, while bulk splitting events (i.e., fracture processes resulting into only two fragments) are frequently found in round Ottawa sand, especially at the onset of comminution, angular Q-ROK#2 grains tend to crush more frequently into multiple fragments at each loading stage. Such variability of the local fracture patterns further emphasizes the shape-sensitivity exhibited by the two sands. These differences vanish at higher stresses (i.e.,  $\sigma/\sigma_y = 2.00$ ), when also Ottawa grains display fracture patterns much closer to those of Q-ROK#2 particles. To quantify the influence of particle shape

on local grain fracture phenomena, two simple fracture indices are proposed, which are computed at each loading step  $j$  as follows:

$$\bar{\alpha}_f = \left( \sum_{i=1}^n N_f^i \right)_j / N_{cpj}, \quad \bar{\beta}_f = \left( \sum_{i=1}^n N_f^i \right)_{j+1} / \left( \sum_{i=1}^n N_f^i \right)_j \quad (6.3)$$

where  $i$  is the ID number of an individual particle,  $N_f^i$  the number of fragments generated by a broken particle at a given loading step, and  $N_{cpj}$  the number of original particles identified as crushed at the selected state. Index  $\bar{\alpha}_f$  quantifies the average number of cumulated fragments produced by broken grains. As such, it can be interpreted as a configurational index tracking the fate (i.e., continuous fragmentation) of initial particles as they undergo comminution. By contrast, index  $\bar{\beta}_f$  uses information available at two successive scans to provide the average number of fragments generated by each incremental loading step. As such, it estimates the average number of new fragments generated by the particles which continue to crush upon successive loading steps. Although the accuracy of  $\bar{\beta}_f$  in reflecting the characteristics of individual fracture events depends on the scan frequency (i.e., it can be expected that to some extent successive events between scans may be cumulated), it provides quantitative insight on individual breakage events, as well as on how the mechanics of grain crushing gradually evolves with the state of the material. It is worth noting that  $\bar{\alpha}_f$  and  $\bar{\beta}_f$  involve a summation across all crushed particles, and thus an averaging. As it will be shown later, these indices can in principle be computed for single particle by ignoring the summation in Eq. (6.3), thus obtaining particle-specific indicators useful to depict the statistical variability of local grain fracture patterns.

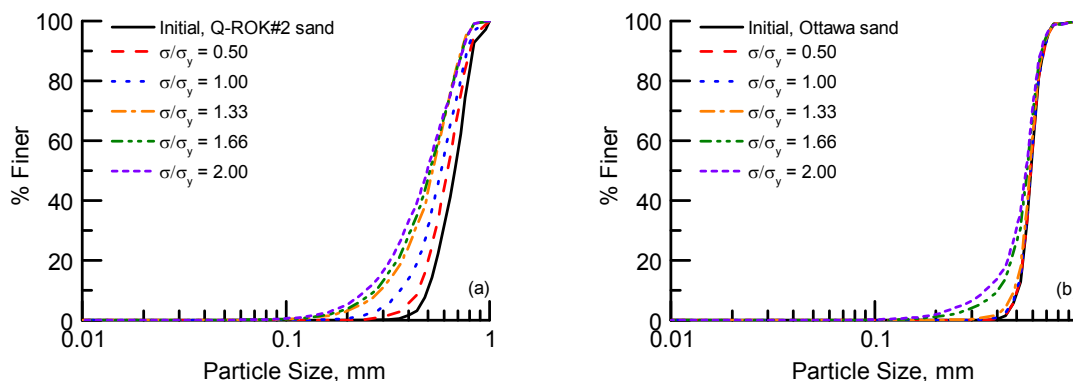


Figure 57. Evolution of GSD curves for (a) Q-ROK#2 and (b) Ottawa sands during oedometric compression, exhibiting progressive growth of finer materials with an increase of loading

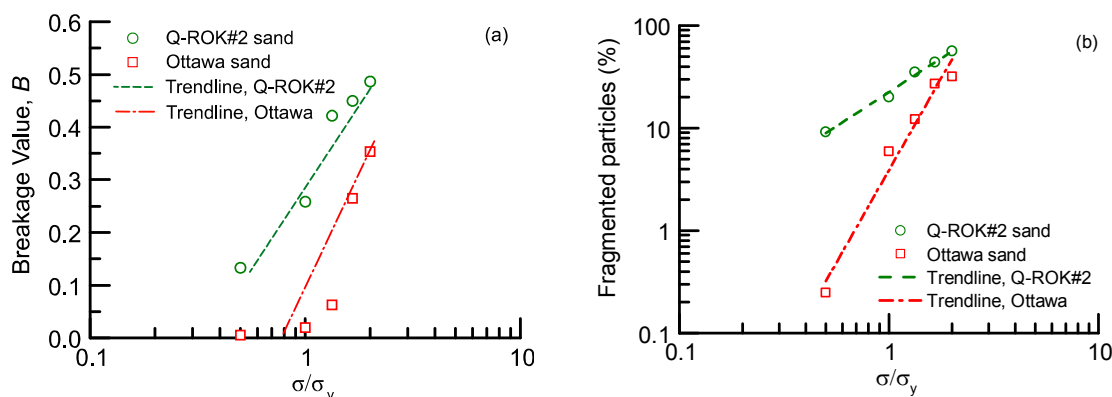


Figure 58. Evolution of (a) the breakage index  $B$  and (b) the percent of fragmented particles for Q-ROK#2 and Ottawa sands. The figures display a more marked growth of breakage index  $B$ , and percent of crushed particles for Ottawa sand.

To estimate the above quantities, the particles of Q-ROK#2 and Ottawa sands were tracked across the sample by examining sequential 3D images. Individual grains were labeled with a specific ID prior to loading and were tracked by translating horizontally a vertical cross-section across the sample until examining all particles. This process was repeated at each loading stage. The indices  $\bar{\alpha}_f$  and  $\bar{\beta}_f$  were then computed to distinguish grain splitting events (i.e., instances when  $\bar{\alpha}_f$  and  $\bar{\beta}_f$  assumed values close to 2) from contact fracture (i.e., cases when fractured grains generated

multiple fragments, as well as values of  $\bar{\alpha}_f$  and  $\bar{\beta}_f$  substantially greater than 2, which reflected concurrent damage processes concentrated at surface asperities). Figure 59a-b report the evolution of the fracture indices as a function of the applied stress. At  $\sigma/\sigma_y = 1.00$ , the values of  $\bar{\alpha}_f$  for Q-ROK#2 and Ottawa sands are 4.0 and 2.5, respectively, suggesting that most round particles split into two fragments, while most angular grains tend to generate four fragments right from the start of comminution. At the same stress, the values of  $\bar{\beta}_f$  for Q-ROK#2 and Ottawa sand are 3.0 and 2.3, respectively, thus indicating that individual breakage events in angular Q-ROK#2 sand tend to produce a higher number of new fragments. As the applied stress increases,  $\bar{\alpha}_f$  and  $\bar{\beta}_f$  grow for both sands, thus implying that breakage patterns become more complex. Furthermore, their values tend to converge towards similar values at the end of the experiments, in that round Ottawa sand exhibits more dramatic changes than those of angular Q-ROK#2 sands in the post-yielding regime. These findings suggest that the influence of the initial particle shape on the geometry of the fracture patterns tends to diminish at high pressure. Such observation is consistent with those previously discussed with reference to the evolution of particle morphology and continuum breakage indices (Figure 54 and Figure 58a).

This conclusion is further corroborated by Figure 60-61 which report the statistical distribution of particle-specific fracture indices  $\alpha_f$  and  $\beta_f$  for Q-ROK#2 and Ottawa sands at  $\sigma/\sigma_y = 0.50, 1.00, 1.33, 1.66$  and  $2.00$ . At yielding ( $\sigma/\sigma_y = 1.00$ ), more than 70 % of the computed values of  $\alpha_f$  and  $\beta_f$  is equal to 2 for Ottawa sand, while Q-ROK#2 sand is characterized by much wider populations, with values ranging from 2 to 12. This implies that during the initial stages of compression the rupture of round particles was primarily due to central splitting, while in angular grains the asperity damage and surface fracture contributed to a much richer distribution of grain

failure events. By contrast, in the post-yielding regime ( $\sigma/\sigma_y = 2.00$ ) the distributions of cumulative and incremental fracture indices in Q-ROK#2 and Ottawa sands become similar, thus confirming once again that at high pressure the effect of the initial particle shape diminishes and consequently the dominant particle failure mechanisms tend to become identical. A closer examination of the local processes provides further insight into the fracture mode of the two sands. 3D renderings of the selected Ottawa and Q-ROK#2 particles before and after breakage are shown in Figure 55-56, corroborating the shape-dependency of the comminution patterns detected by Eq. (6.3). It can thus be inferred that, similar to the grain morphology, comminution promotes the approach of local fracture patterns that do not depend on the initial shape of the particles, but that rather reflect a geometric attractor dictated by the collective response of the granular solid (Ben-Nun et al., 2010).

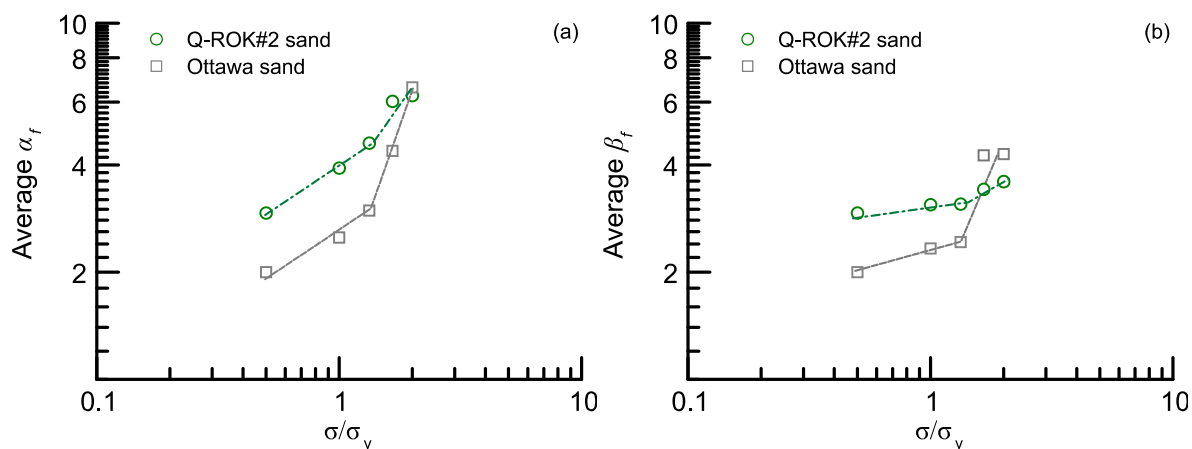


Figure 59. Evolution of (a)-(b) average fracture mode indices for individual particles

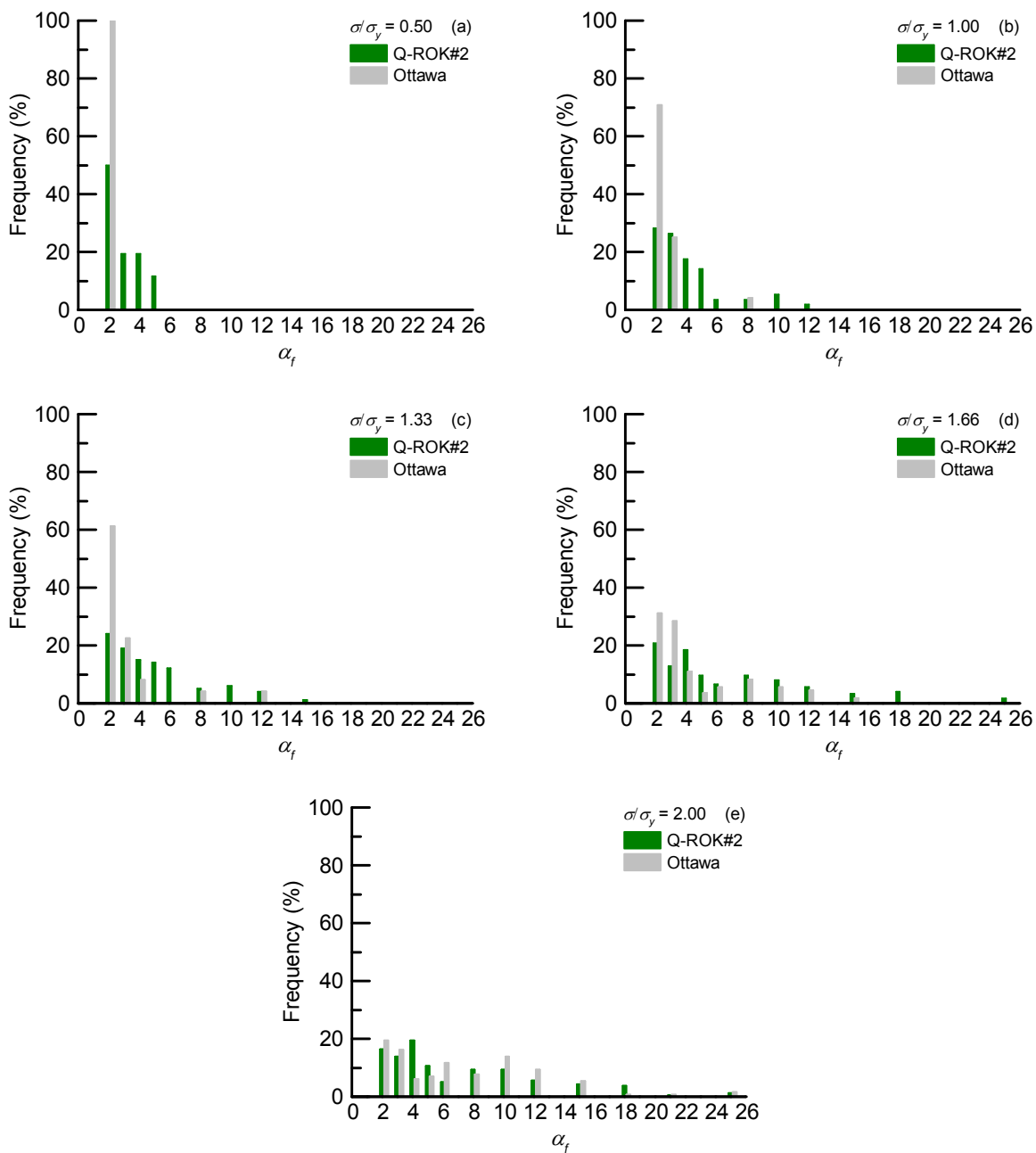


Figure 60. Statistical distribution of particle-specific cumulative fracture index,  $\alpha_f$  at  $\sigma/\sigma_y = 0.50, 1.00, 1.33, 1.66$  and  $2.00$

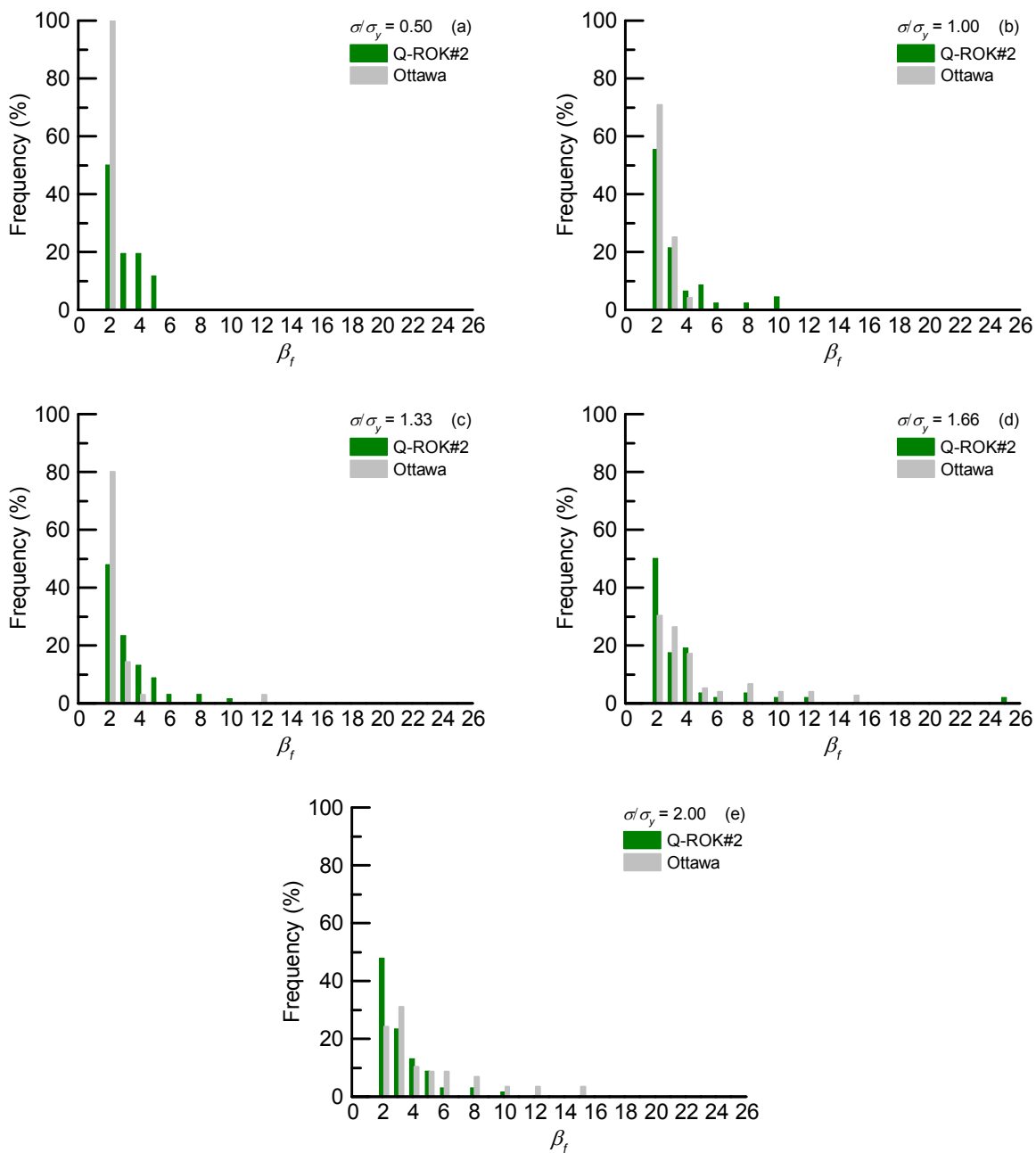


Figure 61. Statistical distribution of particle-specific incremental fracture index,  $\beta_f$  at  $\sigma/\sigma_y = 0.50, 1.00, 1.33, 1.66$  and 2.00

#### 6.4.5 Micro-Macro comparison for yielding stress and compression index

Figure 62 presents experimental measurements of the yield stress,  $\sigma_y$  and the compression index,  $C_c$  (i.e., a slope of the virgin compression curve in a plot of the void ratio against the logarithm of effective stress) of Q-ROK#2 and Ottawa sands computed at micro- and macro-scale tests. The diagonal line is an indicator of the mismatch between the results obtained for samples of different dimensions, in that the farther the data points from the line, the higher discrepancy between the tests. It is found that Ottawa sand has a slightly higher  $C_c$  value, corroborating once again that initially rounded particles show more dramatic transition in the volume deformation under the same loading condition. Good agreement in terms of  $\sigma_y$  and  $C_c$  was found between the macroscopic and miniaturized tests conducted on Q-ROK#2 sand. By contrast, a slightly higher mismatch was found for Ottawa sand. This result can be attributed to the higher stresses required to initiate fracture in rounded Ottawa sand grains, in that even minor variations in packing or statistical distribution of contact forces may result in different likelihood of crushing during continuous loading, which may lead to differences in particle rearrangement and energy dissipation more sensitive to the specimen size.

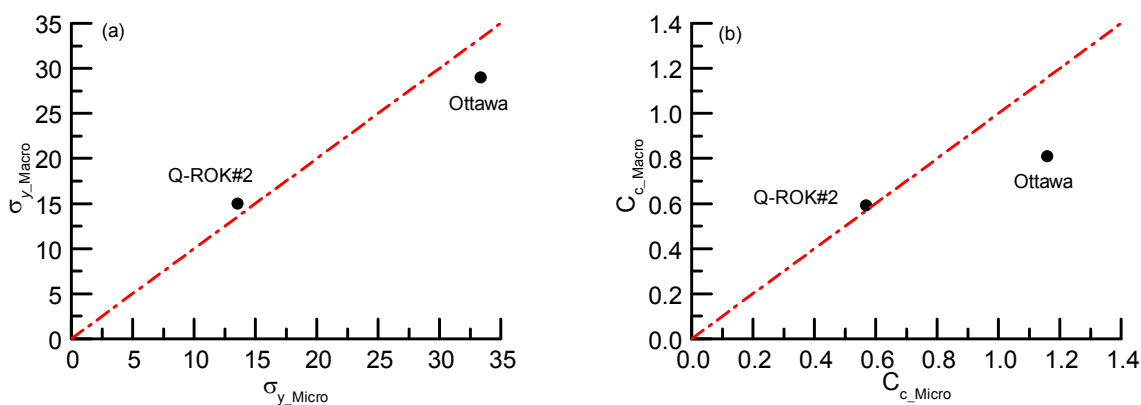


Figure 62 micro-macro comparison for (a) the yield stresses and (b) the compression indices of Q-ROK#2 and Ottawa sand

#### 6.4.6 Creep behavior of geomaterials

Figure 63 presents the accumulation of creep deformation for angular Q-ROK#1, #2, #4 sands and round Ottawa sands over 24 hours at  $\sigma/\sigma_y = 1.33$ . It was not surprising to observe that Q-ROK#4 sand showed the highest global volumetric deformation over 24-hour creeps among all Q-ROK sands, indicating that a larger particle size was more susceptible to the macroscopic volume change, as well as particle breakage at the same loading condition. The slopes ( $\lambda_\epsilon$ ) of the logarithmic trendlines of creep strains for Q-ROK#1, #2 and #4 sands in Figure 63 were found to be  $\lambda_\epsilon = 0.08$ , 0.15 and 0.31, respectively, implying that the rate of accumulation of creep deformation was size-dependent (i.e., larger particle sizes tended to experience a faster rate of creep deformation). The magnitude of the slope of rounded Ottawa sand (i.e.,  $\lambda_\epsilon = 0.25$ ) was slightly higher than that of angular Q-ROK#2 sand (i.e.,  $\lambda_\epsilon = 0.15$ ), indicating that the rate of viscous compression was higher with rounded particles. This may be due to the role of morphological characteristics as previously shown in Figure 54 and Figure 59 in that Ottawa sands has a rapid transition in both particle shape, as well as the fracture mode with a high pressure.

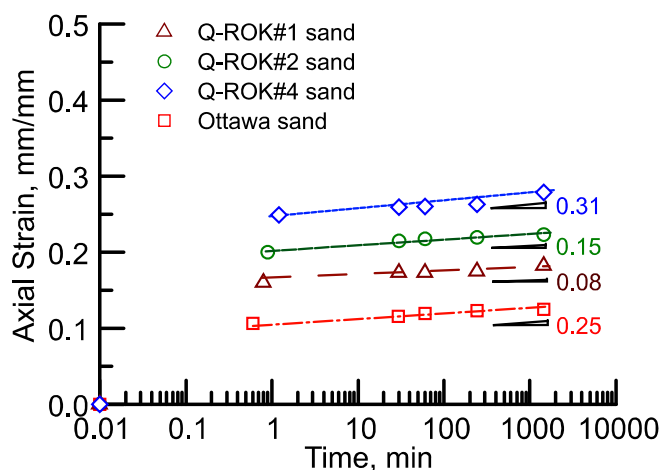


Figure 63. 24-hour creep strains for Q-ROK#1, #2, #4 and Ottawa sands at  $\sigma/\sigma_y = 1.33$ , showing that the rate of creep deformation is size- and shape-dependent (i.e., the rate of creep deformation is expected to become higher with an increase of particle size or initially rounded grains)

### 6.4.7 Particle gradation over 24-hour creep

Figure 64 presents the evolution of the GSDs of all tested sands after 24-hour creep stages. As creep continued, the GSD curves distinctly shifted upwards. This implies that static fatigue (i.e.,  $\sigma/\sigma_y = 1.33$ ) progressively induced delayed particle breakage, consequently generating fragments, and thus resulting in an increase of the percent finer.

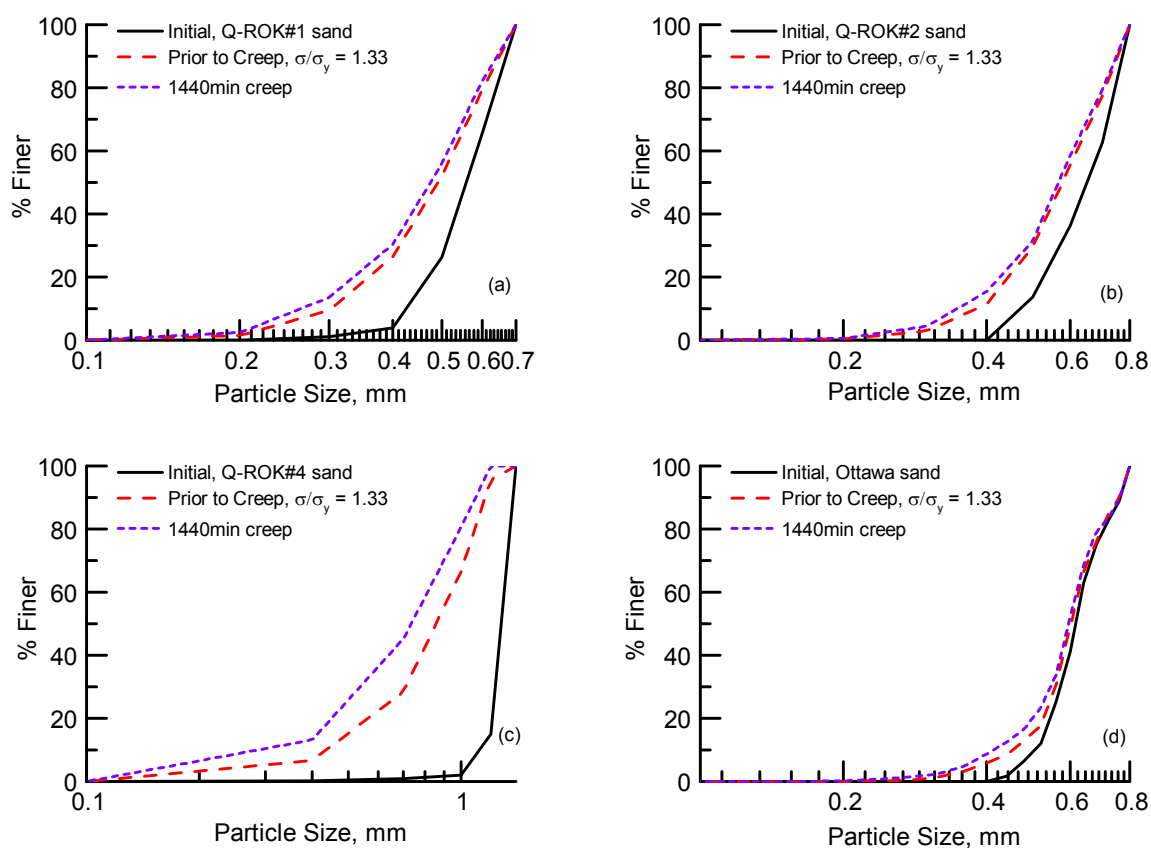


Figure 64. Evolution of GSD curves for (a) Q-ROK#1, (b) Q-ROK#2, (c) Q-ROK#4 and (d) Ottawa sands over 24-hour creep compressions at  $\sigma/\sigma_y = 1.33$

Figure 65 reports plots of the delayed particle breakage measured for 24-hour creep tests. The logarithmic slope ( $\lambda_B$ ) of the  $B$ -time plots quantifies the rate of delayed breakage growth for each sand. It is found that the rate increases with particle size among all Q-ROK sands. Moreover, as

compared with the slopes of Q-ROK#2 and Ottawa sands, it shows that delayed breakage growth rates are higher with rounded particles (i.e., the slope of Ottawa sand,  $\lambda_B = 0.103$  is nearly 10 times greater than that of Q-ROK#2 sand,  $\lambda_B = 0.016$ ). Such finding is in consistent with that measured from the macroscopic tests in Chapter 5. Thus, it implies non-negligible impact of initial particle shape on the rates of delayed breakage growth, as well as creep deformation. Figure 66-67 present direct confirmation of the subcritical crack propagation of local grains when the soil specimen was subjected to 24-hour creep compression at post-yielding regime ( $\sigma/\sigma_y = 1.33$ ).

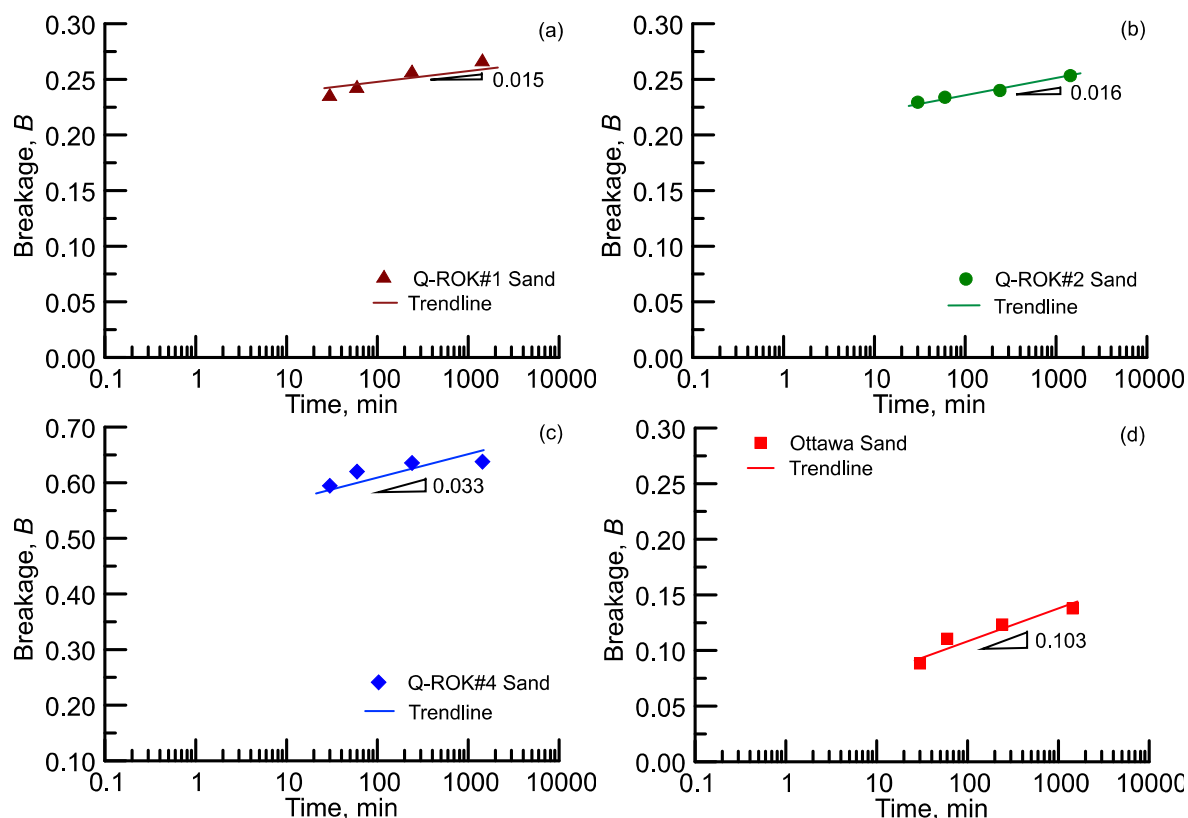


Figure 65. Evolution of delayed breakage values for (a) Q-ROK#1, (b) Q-ROK#2, (c) Q-ROK#4 and (d) Ottawa sands over 24-hour creep at  $\sigma/\sigma_y = 1.33$ , exhibiting higher breakage growth rate for larger grains or rounded particles

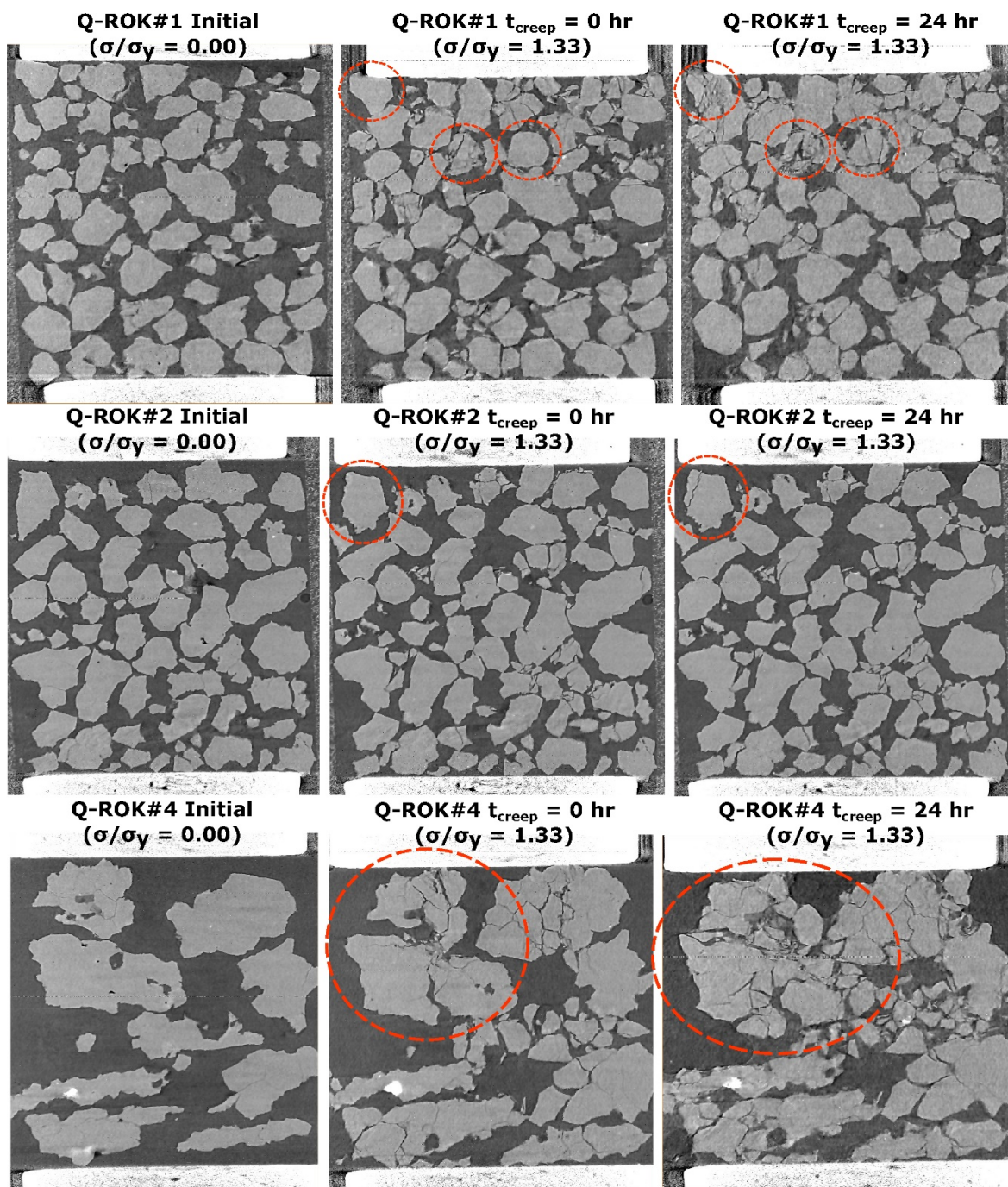


Figure 66. Grayscale vertical cross-sections from 3D SMT images of angular Q-ROK#1 (Top row), Q-ROK#2 (middle row) and Q-ROK#4 (bottom row) sands exhibiting subcritical crack propagation over 24-hour creep at  $\sigma/\sigma_y = 1.33$

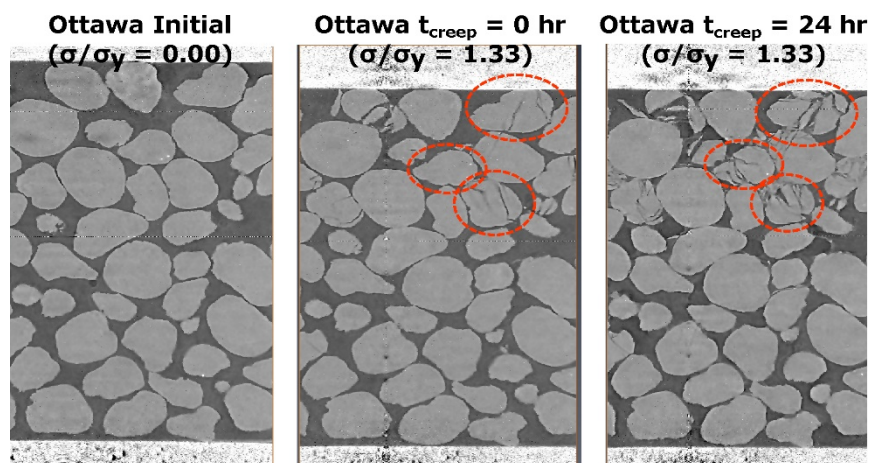


Figure 67. Grayscale vertical cross-sections from 3D SMT images of round Ottawa sand exhibiting subcritical crack propagation over 24-hour creep at  $\sigma/\sigma_y = 1.33$

Figure 68 presents the evolution of the shape of Q-ROK#2 and Ottawa sand particles during 24-hour creep compression tests. Average sphericity and FE ratio are computed by using Eq. (6.1) and (6.2), considering the dimensions of all particles measured from 3D X-ray microtomography images. It is found that initially rounded Ottawa sands suffer a dramatic morphological transition over time to an angular, flat and elongated geometry. Moreover, the shape parameters of the tested sands become similar at 24-hour creep, thus confirming the occurrence of local grains failure due to static fatigue.

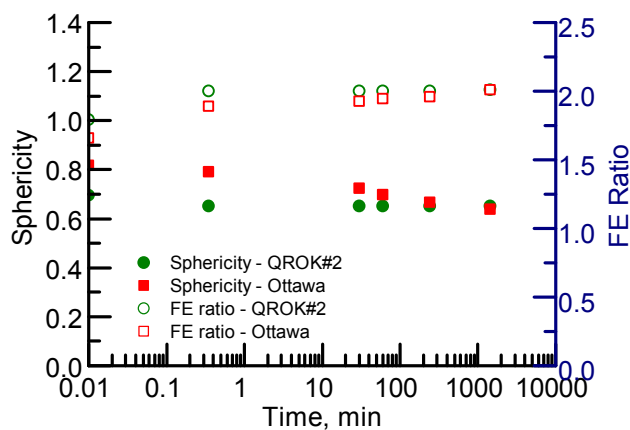


Figure 68 Alteration of the average 3D shape parameters of Q-ROK#2 and Ottawa sands during 24-hour creep ( $\sigma/\sigma_y = 1.33$ )

#### 6.4.8 Comparison between delayed breakage growth and creep strain

Figure 69 reports the measured logarithmic breakage growth rate ( $\lambda_B$ ) plotted against the logarithmic rate of creep strain ( $\lambda_\epsilon$ ) for Q-ROK sands. It is found that the accumulation of creep deformation becomes faster with increasing particle size. This observation confirms the size-dependency of viscous deformations in which larger particles are more susceptible to subcritical crack growth, and thus expecting to have higher comminution, as well as volume changes of the soil specimen. In addition, it further illustrates the correlation between delayed particle breakage and creep in granular soils.

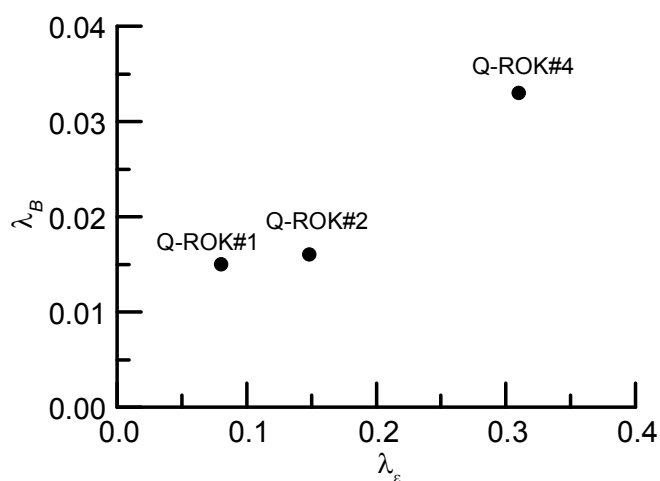


Figure 69. Relationship between the rate of creep strain and delayed breakage growth for Q-ROK sands during 24-hour microscopic creep experiments (i.e., the use of a miniaturized apparatus) at  $\sigma/\sigma_y = 1.33$

#### 6.4.9 Micro-Macro comparison for delayed breakage growth rate and creep strain rate

Figure 70a shows the relation between the rates of 24-hour creep strain ( $\lambda_\epsilon$ ) at micro- and macro-scale measurements (i.e., macro-scale test results are reported in Chapter 5) suggesting once again that the accumulation of creep deformation becomes faster with an increase of particle size. Figure 70b reports the delayed breakage growth rates ( $\lambda_B$ ) of all Q-ROK sands at two scales. Similarly, it clearly shows that  $\lambda_B$  increases with the particle size at both scales. Both metrics have non-

negligible mismatches, indicating that the macroscopic experiment displays larger inelastic changes. In other words, the miniaturized tests tend to underestimate the amount of inelasticity and breakage. It happens because the soil samples within the miniaturized tests are too small to develop a statistically representative network of particles with a spacing of force chains close to those developing in macroscopic samples. Therefore, due to the absent of the actual spacing, the development of inelasticity is inhibited during the microscopic test. Despite the imperfect matches between two-scale experimental data, these comparisons can suggest, on one hand, that both the rates of creep deformation and breakage growth are size-sensitive (i.e., a higher rate is expected with a larger particle size). On the other hand, the observation further implies that subcritical crack growth of the local particles contributes to the comminution and plastic volume change of the soil specimen, subsequently.

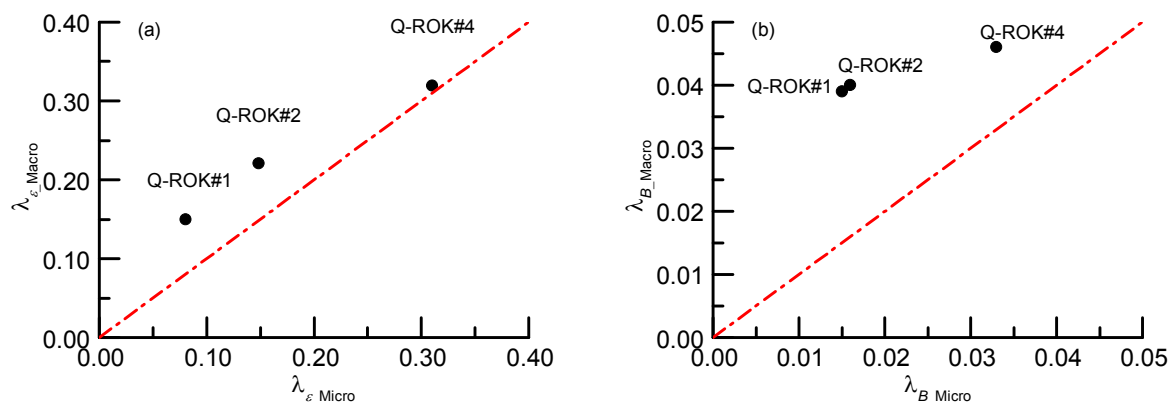


Figure 70. Micro-macro comparison for (a) the rate of creep strain and (b) delayed breakage growth rate during 24-hour creep measurements at  $\sigma/\sigma_y = 1.33$

## 6.5 Concluding Remarks

The effect of the grain shape on the comminution of granular media was assessed at particle and assembly scales via laboratory experiments. High-resolution X-ray microtomography images for

two sands consisting of particles with different initial shape were acquired in-situ during confined compression. The images were post-processed to determine the role of the initial particle shape on the compression behavior of an assembly, as well as on the evolution of the grain morphology. It was found that, while the morphology of round particles changed more severely compared to angular grains, both sets of particles reached similar shape characteristics at the end of the tests, thus suggesting the approach of common morphological attractors that do not depend on the shape of the particles prior to comminution. The concurrent inspection of particle morphology and sample deformation allowed a connection of these trends to the evolution of the grain fracture mechanisms. Two simple fracture indices were defined to identify the patterns of individual fracture events in cumulative and incremental manner, respectively. Their evolution revealed that the average number of fragments caused by the rupture of angular grains was between 4 and 6, thus suggesting the prevalence of surface cracks originated at the particle contacts. By contrast, while the initial stages of comminution in samples consisting of round particles displayed values close to 2 (i.e., failure by central split), a transition of the mode of failure was detected upon continuous loading, with the fracture indices approaching the values found for initially angular particles. These results revealed a transition of the fracture mode of the round particles which is dependent on their shape alteration. Similar to the grain morphology, this transition indicates the convergence of the fracture patterns of the two sands towards a common attractor which appeared to be controlled by the collective response of the assembly, but not by the initial shape of the grains prior to loading.

By providing the first 3D identification of the concurrent evolution of particle sorting, grain shape and local fracture mechanisms, these results shed light on the feedbacks between the continuum-scale response and the particle-scale processes involved in the comminution of geophysical solids.

On one hand, these findings provide explicit proof of earlier predictions based on micromechanics and multiscale continuum models. On the other one, they provide new data to enhance the methods currently used to explain or forecast the physics of fault gauges and the compaction of sedimentary basins, i.e. geophysical systems in which the co-evolution of grain sorting, size and shape impacts the long-term dynamics of the Earth's crust and the exploitation of natural resources.

Lastly, the impact of delayed particle breakage on the creep of granular soils was assessed at micro-scale through X-ray microtomography. Although the micro-scale experiments underestimate the inelastic creep strain and delayed breakage growth over time due to the limited network of particles with a spacing of force chains originated by small size of the sample, they can confirm directly the experimental and numerical findings reported in Chapter 5, exhibiting that the accumulation of creep deformation is associated with the delayed particle breakage.

## CHAPTER 7: DEM MODELING OF SOIL CRUSHING

### 7.1 Introduction

Previous micro-scale experiments provide an opportunity for discrete simulations of granular compaction by moving away from the idealized scheme of homogeneous continua. For this purpose, this chapter uses within a DEM approach some of the particle-scale models introduced in the previous sections of the thesis. The goal is to account for basic grain fracture processes in a discrete modeling technique and produce a virtual replica of the miniaturized experiments. Discrete element method (DEM) is a computational (or virtual) simulation technique that enables to replicate the mechanical behavior of granular materials. Unlike a continuum context in which the model is considered as a continuous material, the advantage of using DEM is that it explicitly reflects particle-scale interactions, so that the simulations enable the prediction of movements and rotations of individual particles in the 2D or 3D space (CUNDALL and HART, 1992). Therefore, DEM techniques are valuable tools along with continuum-scale models to achieve a comprehensive understanding of fundamental particle-scale behaviors, as well as of the system-scale response of geomaterials (O'Sullivan, 2011). DEM has been extensively used as a research tool in the engineering and physical sciences. Particularly, in geomechanics its application has gained much attention to investigate the micro-mechanics of granular soil compression. Since geotechnical laboratory experiments on granular soils reveal that the local failure of grains is directly associated with plastic deformations (De Souza, 1958; Coop et al., 1993; McDowell, 2002), micro-scale models have been an asset for a fundamental understanding of the collective response of crushable sands. For example, Robertson (2000) proposed a hexagonal closed-packed aggregate of bonded spheres to assess the behavior of single sand particles. Cheng et al. (2003) further

validated this approach by calibrating the response of natural silica sands in single particle compression tests as well as isotropic compression of grain clusters. Moreover, Bolton et al. (2008) used this strategy to track the evolution of the coordination number (i.e., the average number of particle-to-particle contacts) in isotropic and triaxial compression simulations, showing an increase in the number of contacts with an increase of the mean stress. Cil and Alshibli (2014) also adopted an agglomerate model to characterize the local particle crushing response in one-dimensional compression simulations. Although the extensive use of an agglomerate in grain crushing models is beneficial to understand the micro-mechanical response of soil plasticity, it may not be feasible for the simulation of a large-scale model due to computational limitations. An alternative approach to simulate grain breakage via DEM is the multi-generational approach (often referred to as *particle replacement technique*), which enables to replace crushed grains with newly generated smaller particles (Ciantia et al., 2016). This technique has been widely used in numerous works (Cil and Buscarnera, 2016, Ben-Nun et al., 2010, McDowell and de Bono, 2013) which have shown its successful applicability in geomechanics. In this chapter, the mechanical and crushing responses at particle- and assembly-scale are replicated through three-dimensional DEM simulations. The particle replacement method is used to simulate local grain crushing at sample-scale. In addition, time effects on the failure of single particle crushing are assessed in the context of DEM simulations with the goal to incorporate concepts of subcritical crack growth theory into the simulation of creep processes.

## 7.2 Technical Background

### 7.2.1 Overview of DEM

In this study, DEM simulations have been performed through the PFC3D software, developed by Itasca, Inc. The sequence of computational steps starts by defining the geometry of the system (i.e., particle coordinates and boundary condition) and contact model (O'Sullivan, 2011). Based on the selection of contact models, the specific contact properties (i.e., elastic stiffness and inter-particle frictional coefficient) have to be assigned accordingly. At a given computational timestep, the contacting particles are identified, and the particle-to-particle forces are computed with reference to the distance between the particle interactions. In addition, the translational and rotational movement of individual particles are simultaneously updated, and subsequently, the magnitude of displacement and rotation of particles are computed. It should be noted that the timestep should be small yet economical enough for the stability of the simulations.

### 7.2.2 Contact models and failure law

The contact forces in DEM simulations indicate a true stress (i.e., the stress can be updated on the basis of changing the cross-sectional area with respect to time at a given load) acting at inter-particle contacts. It is calculated by two orthogonal components (normal and tangential directions), controlling the force within the contacting points. One of the most widely used contact models in DEM simulations is the Hertzian contact model. It is a nonlinear elastic law in which the contact area is smaller than the particle size, thus expecting to have stresses concentrating in contacting points (O'Sullivan, 2011). The normal and shear stiffness can be computed by:

$$k_n = \left( \frac{2\langle G \rangle \sqrt{2 \frac{D_1 D_2}{D_1 + D_2}}}{3(1-\langle \nu \rangle)} \right) \sqrt{U_n} \quad (7.1)$$

$$k_s = \left( \frac{2 \left[ \langle G \rangle^2 3(1-\langle \nu \rangle) \frac{D_1 D_2}{D_1 + D_2} \right]^{1/3}}{2-\langle \nu \rangle} \right) |F_n|^{1/3} \quad (7.2)$$

where  $U_n$  is the sphere overlap,  $D$  is the particle diameter,  $G$  is the shear modulus,  $\nu$  is the Poisson's ratio, and  $F_n$  is the magnitude of the normal contact force. The normal contact force is computed by the following relation:

$$F_n = k_n U_n \quad (7.3)$$

The breakage of individual particles can then be simulated in a stress-based framework by using the average octahedral shear stress (*OSS*), as suggested by Bono et al. (2014):

$$q = \frac{1}{3} \left[ (\sigma_1 - \sigma_2)^2 + (\sigma_2 - \sigma_3)^2 + (\sigma_1 - \sigma_3)^2 \right]^{1/2} \quad (7.4)$$

where  $\sigma_1$ ,  $\sigma_2$ , and  $\sigma_3$  are the average principal stresses of the stress tensor,  $\sigma_{ij}$  associated with contact forces.  $\sigma_{ij}$  can be calculated as follows (Bono et al., 2014):

$$\sigma_{ij} = \frac{1}{V_p} \sum_1^{n_c} (x_i^c - x_i) F_j^c \quad (7.5)$$

where  $V_p$  is the volume of the particle,  $n_c$  is the number of contacts,  $x_i^c$  and  $x_i$  are the positions of contact points and particles, respectively, and  $F_j^c$  is the contact force.

### 7.2.3 Particle replacement configuration

During DEM simulations the criterion event is repeatedly checked at given stress intervals, typically equal to 1% of the mean particle failure stress (Cil and Buscarnera, 2016). If the *OSS* computed from Eq. (7.4) acting on an individual particle is higher than the strength threshold, then the particle is replaced by 20 new smaller particles (or fragments), which will be packed according to an Apollonian packing to which a random rotation is imposed. Figure 71 illustrates an example of single particle before and after replacement due to crushing. It should be noted that the breakage event triggers particle rearrangement and force redistribution, which in turn alters the microstructure of the specimen. Thus, specific computational cycles are required to reach equilibrium after breakage. After completing the particle crushing event, the applied loading will be continued to the following increment.

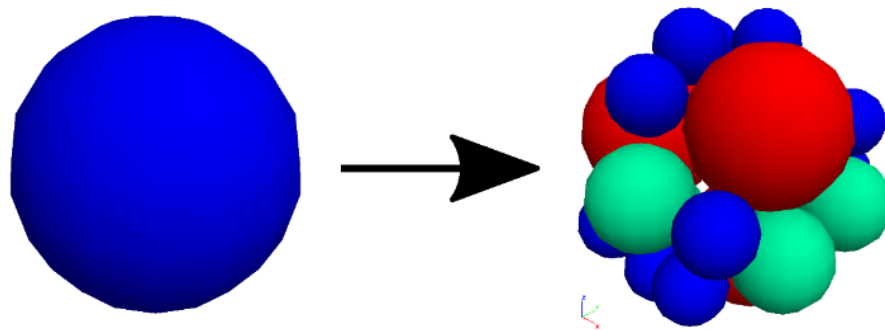


Figure 71. Initial configuration of single particle and particle replacement configuration, illustrating that an initial particle is broken and replaced by 20 new fragments arranged through an Apollonian packing

### 7.3 3D Virtual Assessment of Soil Crushing

#### 7.3.1 Single particle crushing simulation

To address the micro-mechanical interactions and fracture behavior of single particles, a failure criterion has to be defined. Here, a stress-based (or stress-limiting) failure criteria is used in the DEM simulations (Russell and Muir Wood, 2009). A simple mathematical expression of the particle failure criteria can be summarized as follows:

$$\frac{F}{d^2} \leq \sigma_{pc\_ref} \left( \frac{d}{d_{ref}} \right)^{-\eta} \quad (7.6)$$

where  $F$  is the applied load force,  $d$  is the particle diameter, and  $\sigma_{pc\_ref}$  is the mean failure stress of a reference particle size,  $d_{ref}$ . The central crack mode (i.e., a particle splits into two fragments at failure) is assumed for the simulations and therefore a power law coefficient,  $\eta$ , is assumed to 1/2 (Zhang et al., 2016, Cil and Buscarnera, 2016). For the contact elasticity, Hertzian model is used.

Figure 72 presents the DEM simulation of a single particle crushing test.

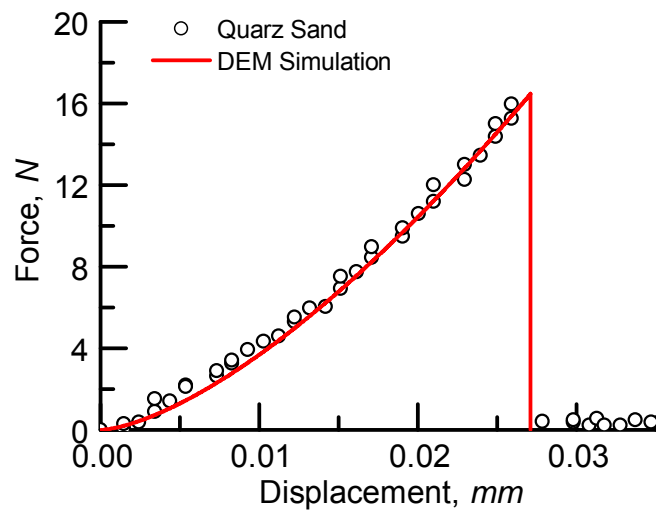


Figure 72. DEM simulation of force-displacement behavior of single particle using the stress-based failure criteria with Hertzian contact model

Table 6 summarizes model parameters valid for the typical values of natural quartz sand. The DEM simulation with the given failure criterion and nonlinear contact elasticity can satisfactorily capture the response of a rounded quartz sand, exhibiting a sudden drop of the magnitude of the force at failure. Figure 73 illustrates the virtual particle after the completion of the simulation. The colors represent the contact forces of particle (i.e., ball) and wall (loading platen).

Table 6. Summary of DEM model parameters for simulating single particle crushing

| Model Parameters            |                             | Value                  |
|-----------------------------|-----------------------------|------------------------|
| General Parameters          | $\sigma_{pc\_ref}$          | 30 MPa                 |
|                             | Particle diameter           | 670 microns            |
|                             | Reference particle diameter | 1000 microns           |
|                             | Particle density            | 2650 kg/m <sup>3</sup> |
| Hertzian Contact Properties | Shear modulus               | 12.5 GPa               |
|                             | Poisson's ratio             | 0.077                  |
|                             | Friction coefficient        | 0.00                   |

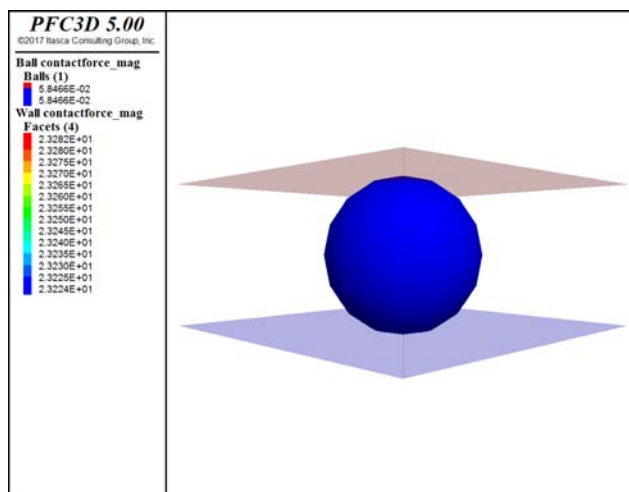


Figure 73. Example of a virtual DEM particle after a diametral compression simulation

### 7.3.2 Oedometric compression simulation

An oedometric compression test can be simulated by DEM. Initially, spherical particles are generated randomly in a cylindrical virtual container. The particle density is assigned to 2650 kg/m<sup>3</sup> which is the typical value of natural quartz sands. The packing porosity of the virtual specimen is assigned on the basis of a given initial void ratio. For this DEM simulation, the initial macroscopic porosity is set to 0.43 which is the densest possible in the virtual sample. The sample is then subjected to a computational timestep by setting to zero the inter-particle friction in order to minimize particle overlap and optimize particle rearrangement. Equilibrium of the virtual specimen is usually attained when the mean effective stress is less than 3 kPa (Cil and Buscarnera, 2016). At this point, the contact elasticity (i.e., Hertzian contact model parameters) as well as the strength of individual particles (i.e., size effect law in Eq. (7.6), where  $\eta$ , is assumed to 3/2 and 1/2 for surface crack and central splitting mode, respectively) are fixed to their final magnitudes.

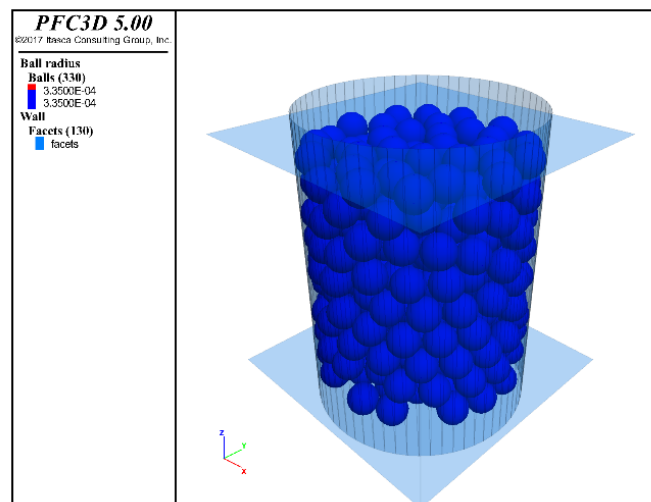


Figure 74. A virtual DEM specimen composed of monodisperse particles ( $d = 670$  micron) prior to an oedometric compression simulation. The color reflects the particle size.

The compression of the virtual specimen is then simulated by moving both top and bottom walls (i.e., loading platens). The loading is imposed by a strain-controlled mode with the maximum vertical velocity of 0.01 m/s. The local non-viscous numerical damping coefficient, which damps only accelerating motion automatically, is set to 0.70. For the simulation of oedometric compression, Hertzian contact elasticity is employed. The model parameters (i.e., shear modulus and Poisson's ratio) are determined based on the typical linear elastic properties of quartz materials (McDowell and de Bono, 2013). The failure criteria, here, is assumed to the surface crack mode ( $\eta = 3/2$ ). The inter-particle friction coefficient is assumed to 0.50, a value typically used for DEM analyses of quartz sand (Cil and Buscarnera, 2016). Table 7 shows the summary of the DEM model parameters.

Table 7. Summary of DEM model parameters for simulating oedometric compression

| Model Parameters       |                             | Value                  |
|------------------------|-----------------------------|------------------------|
| General Parameters     | Density of spheres          | 2650 kg/m <sup>3</sup> |
|                        | Particle diameter, $d$      | 670 microns            |
|                        | Initial void ratio, $e_o$   | 0.75                   |
|                        | $\sigma_{pc\_ref}$          | 44 MPa                 |
|                        | $d_{ref}$                   | 700 microns            |
| Hertzian Contact Model | Contact shear modulus, $G$  | 3.6 GPa                |
|                        | Poisson's ratio, $\nu$      | 0.077                  |
|                        | Friction coefficient, $\mu$ | 0.50                   |

Figure 75 reports the stress-strain responses and GSD evolution of the DEM virtual specimen. The results indicate that the given failure criteria and contact elasticity of DEM analysis enables to generate a stress-strain behavior and comminution response. Particularly, the DEM simulation

clearly indicates the evolution of particle gradation after loading. Although this study is performed on qualitative purpose, the further study should be focused on the model simulation for experimental measurements. The virtual DEM specimen and force chain after the oedometric compression are displayed in Figure 76. The completely fractured local particles are replaced with 20 new fragments arranged through an Apollonian packing.

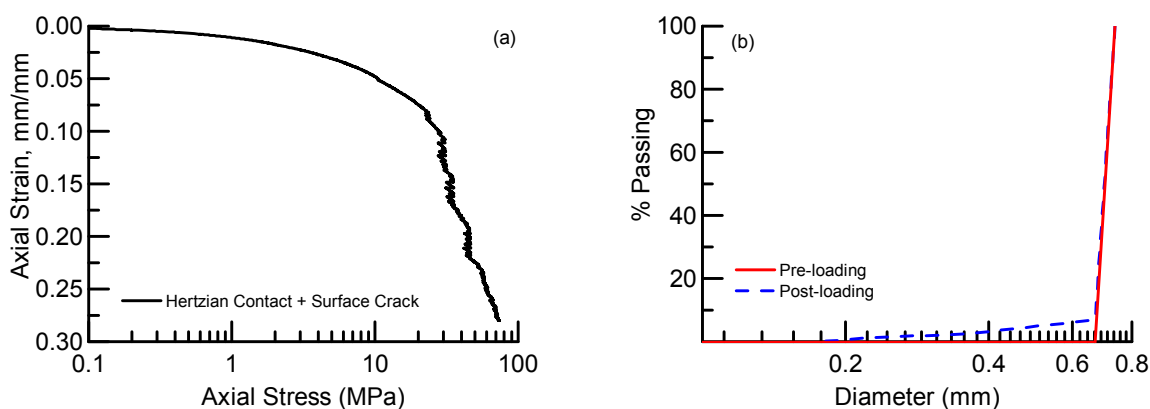


Figure 75. (a) stress-strain behavior of the DEM specimen for oedometric compression, and (b) the GSD evolution for the same virtual simulation based on the Hertzian contact law and surface crack mode

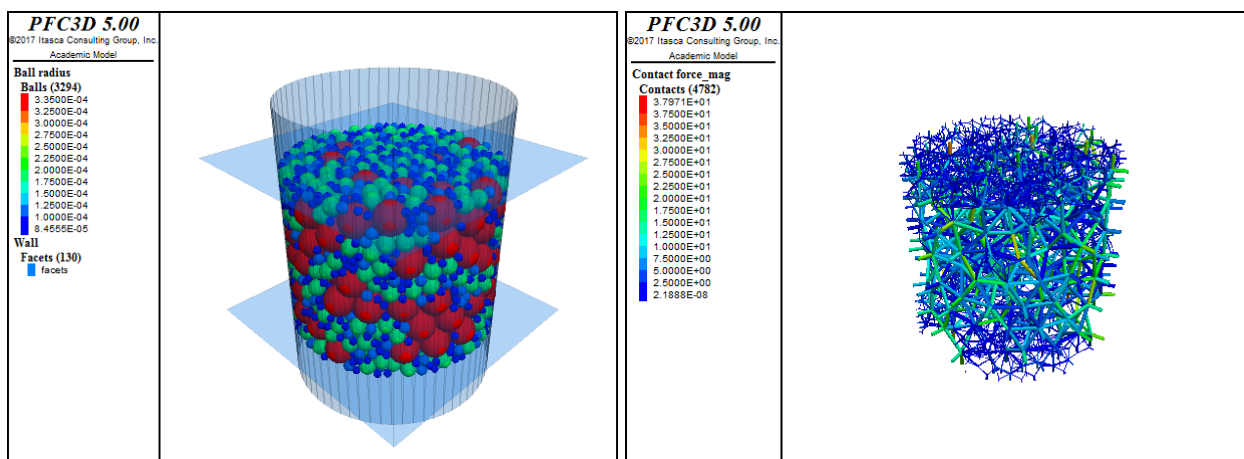


Figure 76. (left): A virtual DEM specimen made of initially uniform particle size ( $d = 670$  micron) after the oedometric compression simulation. The color reflects the particle size in radius. (Right): The force chain of inter-particle contacts after the completion of loading. The color reflects the magnitude of inter-particle contact forces

### 7.3.3 Creep simulation

Subcritical crack growth or static fatigue refers to the phenomenon in which the complete failure of a particle is triggered by the extension of flaws at values of the energy release rate lower than the critical threshold for instantaneous fracture (Atkinson and Meredith, 1987). Subcritical crack growth of a particle controls the accumulation of creep deformation of the assembly made of the same material (Chester et al., 2007) and thus it is important to understand time effects in sand. Zhang and Buscarnera (2017) proposed a simple mathematical expression for subcritical crack growth that combined two kinetic laws derived by Charles (1958) and Maugis (1985), considering a stress corrosion limit below which the growth of a crack ceases.

$$\dot{l} = \dot{l}_0 \left\langle \frac{G_I}{2\gamma} - 1 \right\rangle^{n/2} \quad (7.7)$$

where  $G_I$  is the energy release rate for tensile fracture and  $\gamma$  is the surface energy related to the onset of crack propagation at a specific environmental condition.  $\dot{l}_0$  is a reference crack velocity;  $n$  is a subcritical crack growth coefficient. Assuming a through crack within a plate under tension and plane stress condition, Griffith postulated the following relation between energy release and imposed stress state:

$$G_I = \frac{\sigma^2 \pi a}{E} = \frac{\sigma^2 \pi l}{2E} \quad (7.8)$$

where  $\sigma$  is the tensile stress;  $a$  is the half crack length,  $l$ ; and  $E$  is the Young's modulus. Substituting Eq. (7.8) into Eq. (7.7), the following expression is obtained:

$$\dot{l} = \dot{l}_0 \xi_c^{n/2} \quad (7.9)$$

where  $\xi_c = \frac{\sigma^2 \pi l}{4E\gamma} - 1$  is a fracture overstress function (Zhang and Buscarnera, 2017). Therefore, a time-to-failure,  $t_f$ , of single particle can be expressed as following (A detail mathematical derivation is expressed in Appendix D):

$$t_f = \frac{l_0}{\dot{l}_0} \left( \frac{4E\gamma}{\sigma^2 \pi l_0} \right)^{1-n/2} \left[ - \left( \frac{\sigma^2 \pi l_0}{4E\gamma} - 1 \right)^{1-n/2} \right] \quad (7.10)$$

Figure 77 shows the result of a DEM simulation of subcritical crack growth based on Eq. (7.9).

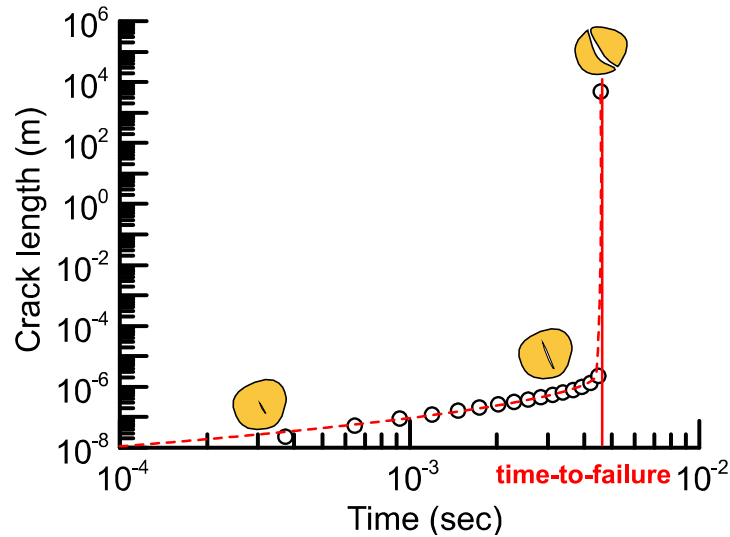


Figure 77. Result of 3D DEM simulation (symbols) for single particle under static fatigue plotted with the trendline of the crack propagation (line). The crack growth progressively continued until a sudden increase of the crack length at which the particle completely fractured.

The model parameters are assumed based on the typical range of quartz minerals (Table 8). It should be noted that the main objective here is to evaluate the particle-scale subcritical crack

growth model through a three-dimensional DEM simulation. Thus, DEM analyses are considered as a virtual platform to examine the time-to-failure of the grain. Hertzian elasticity is assumed for contacts. An initial flaw size is set to 6.7 micron which is 1/100 smaller than the particle size. The vertical velocity is set to 0.1 m/s until the applied stress reaches  $\sigma_v = 50$  MPa. Afterwards,  $\sigma_v$  is kept constant until the particle completely fails (i.e., a sudden increase of crack length at which the flaw size becomes greater than the particle diameter). As shown in Figure 77, the 3D DEM simulation provides a satisfactory computation of the time-to-failure on single particle susceptible to static fatigue.

Table 8. Summary of DEM model parameters for simulating subcritical crack propagation of single particle

| Model Parameters               |                                        | Value                  |
|--------------------------------|----------------------------------------|------------------------|
| General Parameters             | Density of spheres                     | 2650 kg/m <sup>3</sup> |
|                                | Particle diameter, $d$                 | 670 microns            |
|                                | Reference particle diameter            | 1000 microns           |
|                                | Creep stress                           | 50 MPa                 |
| Hertzian Contact Model         | Contact shear modulus, $G$             | 10 GPa                 |
|                                | Poisson's ratio, $\nu$                 | 0.25                   |
|                                | Friction coefficient, $\mu$            | 0.50                   |
| Subcritical Crack Growth Model | Initial crack growth rate, $\dot{l}_0$ | 1E-8 m/s               |
|                                | Young's modulus, $E$                   | 8000 MPa               |
|                                | $n$                                    | 22                     |
|                                | $\gamma$                               | 0.495 J/m <sup>2</sup> |
|                                | Initial crack size                     | 6.7 microns            |

The particle-scale subcritical crack growth law is also implemented in a sample-scale model, thus enabling DEM simulations of the macroscopic delayed stress-strain response of virtual specimens. Prior to the application of creep stages, the virtual 3D DEM specimen is generated (Figure 74). The initial model parameters of the specimen are the same used for the oedometric compression simulation (Table 7). For the oedometric creep simulation, Hertzian elasticity is employed. The model parameters (i.e., shear modulus and Poisson's ratio) are determined based on the typical elastic properties of quartz (McDowell and de Bono, 2013). The subcritical crack growth model parameters in Table 8 are used for the macroscopic stress-strain response of the continuum-scale virtual specimen. The friction coefficient of inter-particle contact is assumed to be 0.50. An axial stress of  $\sigma_v = 10$  MPa is applied and then sustained for the entire remaining computational time. Figure 78 shows the results of a DEM simulation of macroscopic creep stress-strain response, showing qualitatively the capability of the proposed model ingredients to replicate aspects of the sample-scale macroscopic creep behavior observed in the previous chapters simply by starting from particle-scale hypotheses.

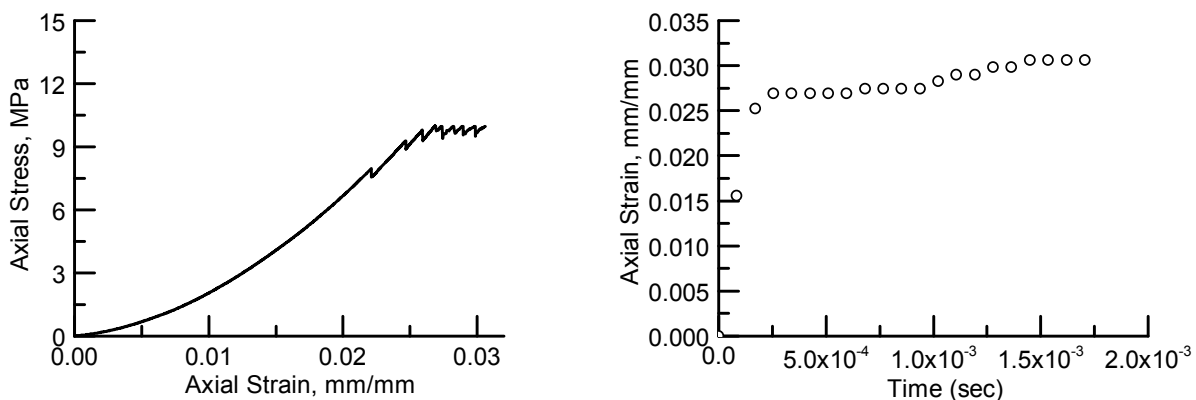


Figure 78. (left) Macroscopic creep stress-strain response and (right) accumulation of creep strain of the virtual DEM specimen using the particle-scale subcritical crack theory

Figure 79a-d visualizes the role of subcritical crack propagation at specimen-scale by displaying a crack growth indicator (i.e., a scalar flag equal to 1 when signaling the onset of crack propagation or 0, when there is no prediction of local crack growth) and the evolving intra-particle crack size at the pre-creep and post-creep compressions. Although the results are qualitatively satisfactory, a further work is necessary to apply the model in quantitative terms (i.e., a model calibration for specific measurements at both particle and sample scale).

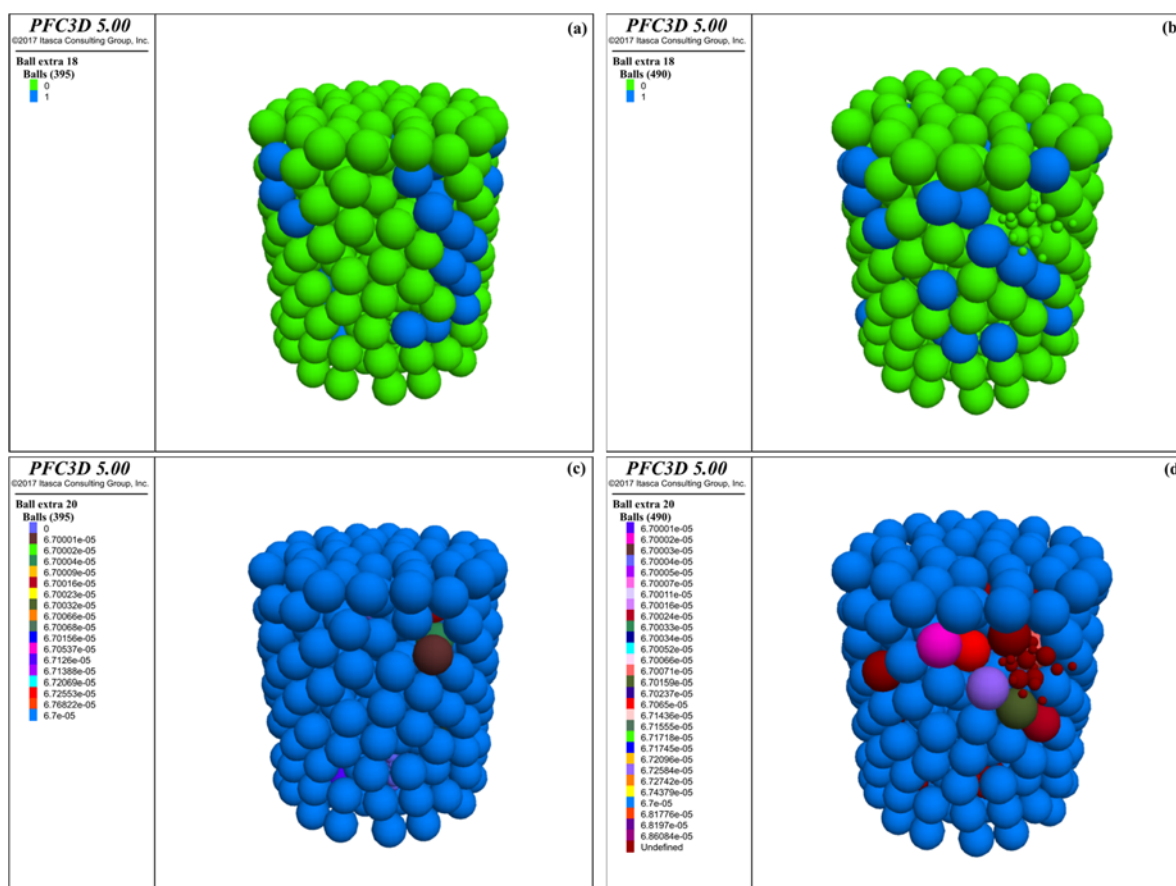


Figure 79. A virtual DEM specimen after creep compression simulation which initially composed of monodisperse particles ( $d = 670$  micron) including uniform crack sizes. (a)-(b) an indicator of crack growth sign, signaling the crack growth if the color of particle is green at pre-creep and post-creep, respectively; (c)-(d) crack size of individual grains in *meters* at pre-creep and post-creep, respectively

#### 7.4 Concluding Remarks

In this chapter, three-dimensional DEM simulations have been conducted to incorporate concepts of instantaneous and delayed particle fractures similar to those previously discussed in the context of continuum breakage models. Moreover, the particle-scale properties and stress-limiting failure laws have been considered in the context of DEM simulations of virtual specimens made of randomly distributed particles with the goal to simulate the stress-strain behavior of sand samples under oedometric conditions. The analyses are performed by using the Hertzian contact elasticity along with size-effect failure criteria. The results from the DEM simulations suggest that the micro-mechanical modeling of instantaneous and delayed local grains failure can be a useful tool to replicate several aspects of sand behavior in the context of discrete simulations.

Time effects have been also considered in 3D DEM simulations by implementing a subcritical crack growth theory at particle scale. The results provide a satisfactory qualitative prediction of the time-to-failure of individual particles subjected to a static fatigue. Furthermore, the collective response of a virtual specimen has also been predicted, showing that the proposed DEM model is capable to predict the accumulation of creep deformation and to track the local grain crushing. While these results indicate good qualitative agreement with the multi-scale crushing behavior discussed in previous chapters, further study is necessary to apply these discrete models quantitatively, and hence a future work should focus on the calibration of the proposed DEM model on the basis of experimental data available at both particle- and sample-scale.

## CHAPTER 8: CONCLUSIONS

### 8.1 Main Conclusions

In this study, a systematic laboratory testing program was undertaken under quasi-static conditions to evaluate the role of particle attributes on collective crushing mechanism occurring due to loading or time elapse. To understand particle-scale fracture behavior, diametral compression tests were conducted on particulate materials with angular grains (i.e., three Q-ROK sands with different mean grain size) and particulate materials with spherical or rounded grains (e.g., glass beads and Ottawa sand). Furthermore, oedometric compression tests were performed on the same materials to measure their collective stress-strain behaviors and macroscopic yielding characteristics. The continuum breakage mechanics theory was used to quantify the model parameters and capture the experimental observations. Furthermore, a scaling factor was evaluated to link particle- and sample-scale energy measures directly. To consider time effects, oedometric creep compression tests were carried out on four quartz sands. Using the tests, it was possible to quantify the role of the particle size and shape on the accumulation of creep compression, as well as delayed breakage growth. Moreover, the viscous breakage mechanics theory has been evaluated by fitting the model parameters for the experimental measurements. Synchrotron X-ray microtomography was adopted to provide direct confirmations on the abovementioned experimental and numerical findings. Particularly, two indices were introduced to quantify the fracture modes of crushable geomaterials with the goal of corroborating the concurrent alteration of local grain failure mechanism and morphological characteristic under continuous loading. Finally, DEM simulations were performed to corroborate the findings and provide a virtual computational platform to replicate the multi-

scale processes observed during the experiments. The main contributions of this study are highlighted as follow:

1. Particle strength and energy stored in particles at the onset of failure have been found to be size- and shape-dependent, in that they tend to decrease with the increase of the grain size or with the transition from round to angular particles.
2. The fracture mode was found to be shape-dependent, in that highly angular sands were satisfactorily captured by a surface fracture model assuming failure initiation at edge cracks, while spherical particles were well explained by the central fracture model, thus reflecting particle split in proximity of the median plane. These findings were corroborated by X-ray microtomography images. In particular, it was observed that initially rounded particles tend to initially suffer splitting processes, eventually fragmenting upon continuous loading and exhibiting shape transitions. The fracture mode of initially rounded grains was also found to be altered accordingly, passing from central split to surface failure.
3. The magnitude of breakage was computed based on the continuum breakage mechanics theory by tracking the evolution of the grain size distribution. It was found that the role of particle attributes (i.e., size and shape) play a major role on the collective breakage response, in that a specimen composed of larger or angular grains displayed higher breakage values compared to rounded particles of similar size subjected to comparable stress levels. Such finding suggested that the local grain crushing mechanism was directly associated with the collective breakage response of the specimen, which in turn impacted the volume change of the specimen.
4. Time effects were also found to be size- and shape-dependent. The rates of accumulation of creep strains and delayed breakage were found to be higher for larger grains or rounded

particles. The use of a viscous breakage mechanics model enabled the evaluation of a subcritical corrosion coefficient, providing satisfactory agreements with the experimental measurements (i.e., the accumulation of creep strain, GSD evolutions prior and after creep, delayed breakage growth). Furthermore, it was found that the stress corrosion index was constant if the material had similar mineralogical characteristics, whereas the reference breakage rate was size-sensitive (i.e., the rate diminished with an increase of particle size).

5. DEM simulations were used as a virtual computational laboratory tool to mimic the local grain crushing behavior and the collective stress-strain behavior of granular materials. The particle replacement technique enabled to model grain crushing phenomenon at failure and to successfully compute the macroscopic stress-strain response and breakage evolution. Furthermore, particle-scale subcritical crack growth theory was implemented in the model simulation to predict the time-to-failure of single particle as well as the delayed comminution of an assembly. Although this study was based on a qualitative validation of the DEM model, it provided a general framework for better understanding the collective response of creep deformation on the basis of a grain-scale fracture kinetics model.

## **8.2 Future Scope of Work**

Multiple future directions can be suggested as follow:

1. All experimental and numerical performances can be further extended to dynamic loading conditions to evaluate the particle crushing and collective comminution responses at high strain rates. The use of split Hopkinson pressure bars (i.e., pieces of equipment through which the strain rate can go up to  $10^5$  per second) is recommended to capture the role of rate effects on single particle crushing under dynamic conditions and consequently

enabling to provide a unique comparison between the grain crushing characteristics in quasi-static and dynamic conditions.

2. In the current creep measurements, the soil specimens were fully saturated with de-ionized water. To evaluate the role of environmental interactions on time effects (i.e., the delayed breakage growth and the accumulation of creep deformation) different types of fluids (i.e., oil and ethanol), or various temperature and relative humidity can be further considered to the soil samples. The expanded experimental measurements of creep behavior can be more attractive for industrial applications, particularly in the oil and gas sector.
3. All experimental tests were performed under oedometric compression conditions. A drawback of this laboratory experiment is that the radial stress cannot be measured, consequently making the interpretation stage more uncertain. Alternatively, triaxial testing can be used to measure both axial and lateral stresses during the tests, and hence providing more precise analyses, as well as a possible improvement of the model simulations.
4. The DEM simulations should be further validated by capturing the experimental measurements for oedometric compression and creep compression. Both quantitative and qualitative results will then complement the particle-scale model inspired by the fracture mechanics theory to predict the continuum breakage behavior of collective virtual materials.

## REFERENCES

- Agnolin, I., Roux, J.-N., Massaad, P., Jia, X. & Mills, P. (2009) Sound wave velocities in dry and lubricated granular packings: numerical simulations and experiments.
- Alshibli, K., Sture, S., Costes, N. C., Frank, M., Lankton, M., Batiste, S. & Swanson, R. (2000) Assessment of localized deformations in sand using X-ray computed tomography. *Geotechnical Testing Journal* **23(3)**:274-299.
- Alshibli, K. A., Druckrey, A. M., Al-Raouch, R. I., Weiskittel, T. & Lavrik, N. (2013) Quantifying Morphology of Sands Using 3D Imaging. *J. Mater. Civil Eng.*:Medium: X; Size: 04014275.
- Altuhafi, F. N. & Coop, M. R. (2011) Changes to particle characteristics associated with the compression of sands. *Geotechnique* **61(6)**:459-471.
- Andò, E., Hall, S., Viggiani, G., Desrues, J. & Bésuelle, P. (2012) Grain-scale experimental investigation of localised deformation in sand: a discrete particle tracking approach. *Acta Geotechnica* **7(1)**:1-13.
- Andò, E., Viggiani, G., Hall, S. A. & Desrues, J. (2013) Experimental micro-mechanics of granular media studied by x-ray tomography: recent results and challenges. *Géotechnique Letters* **3(3)**:142-146.
- Antonellini, M. A., Aydin, A. & Pollard, D. D. (1994) Microstructure of deformation bands in porous sandstones at Arches National Park, Utah. *Journal of Structural Geology* **16(7)**:941-959.
- Arroyo, M., Butlanska, J., Gens, A., Calvetti, F. & Jamiolkowski, M. (2011) Cone penetration tests in a virtual calibration chamber. *Geotechnique* **61(6)**:525-531.

- Arshad, M. I., Tehrani, F. S., Prezzi, M. & Salgado, R. (2014) Experimental study of cone penetration in silica sand using digital image correlation. *Geotechnique* **64(7)**:551-569.
- Atkinson, B. K. (1982) Subcritical crack propagation in rocks: theory, experimental results and applications. *Journal of Structural Geology* **4(1)**:41-56.
- Atkinson, B. K. (1984) Subcritical crack growth in geological materials. *Journal of Geophysical Research: Solid Earth* **89(B6)**:4077-4114.
- Atkinson, B. K. & Meredith, P. G. (1987) 4 - THE THEORY OF SUBCRITICAL CRACK GROWTH WITH APPLICATIONS TO MINERALS AND ROCKS. In *Fracture Mechanics of Rock*. (Atkinson, B. K. (ed)) Academic Press, London, pp. 111-166.
- Baud, P., Klein, E. & Wong, T.-F. (2004) Compaction localization in porous sandstones: spatial evolution of damage and acoustic emission activity. *Journal of Structural Geology* **26(4)**:603-624.
- Baud, P., Zhu, W. & Wong, T.-F. (2000) Failure mode and weakening effect of water on sandstone. *Journal of Geophysical Research: Solid Earth* **105(B7)**:16371-16389.
- Becken, M., Ritter, O., Bedrosian, P. A. & Weckmann, U. (2011) Correlation between deep fluids, tremor and creep along the central San Andreas fault. *Nature* **480**:87.
- Ben-Nun, O., Einav, I. & Tordesillas, A. (2010) Force attractor in confined comminution of granular materials. *Physical review letters* **104(10)**:108001.
- Ben-Zion, Y. & Sammis, C. G. (2003) Characterization of Fault Zones. *pageoph* **160(3)**:677-715.
- Bernard, D., Guillon, O., Combaret, N. & Plougonven, E. (2011) Constrained sintering of glass films: Microstructure evolution assessed through synchrotron computed microtomography. *Acta Materialia* **59(16)**:6228-6238.

- Billam, J. (1971) Some aspects of the behaviour of granular materials at high pressures. *Stress-strain Behaviour of Soils : Proceedings of the Roscoe Memorial Symposium, Cambridge University, 1971.*
- Bolton, M. D., Nakata, Y. & Cheng, Y. P. (2008) Micro- and macro-mechanical behaviour of DEM crushable materials. *Geotechnique* **58(6)**:471-480.
- Bono, J., McDowell, G. & Wanatowski, D. (2014) DEM of triaxial tests on crushable cemented sand. *Granular Matter* **16(4)**:563-572.
- Brantut, N., Baud, P., Heap, M. J. & Meredith, P. G. (2012) Micromechanics of brittle creep in rocks. *Journal of Geophysical Research: Solid Earth* **117(B8)**:n/a-n/a.
- Brzesowsky, R. H., Hangx, S. J. T., Brantut, N. & Spiers, C. J. (2014) Compaction creep of sands due to time-dependent grain failure: Effects of chemical environment, applied stress, and grain size. *Journal of Geophysical Research: Solid Earth* **119(10)**:7521-7541.
- Buscarera, G. & Einav, I. (2012) The yielding of brittle unsaturated granular soils. *Geotechnique* **62(2)**:147-160.
- Cavarretta, I., O'sullivan, C. & Coop, M. R. (2017) The relevance of roundness to the crushing strength of granular materials. *Geotechnique* **67(4)**:301-312.
- Chan, A. W. & Zoback, M. D. (2007) The role of hydrocarbon production on land subsidence and fault reactivation in the Louisiana coastal zone. *Journal of Coastal Research* **23(3)**:771.
- Chang, C. D., Mallman, E. & Zoback, M. (2014) Time-dependent subsidence associated with drainage-induced compaction in Gulf of Mexico shales bounding a severely depleted gas reservoir. *Aapg Bulletin* **98(6)**:1145-1159.
- Charles, R. J. (1958) Static Fatigue of Glass. I. *Journal of Applied Physics* **29(11)**:1549-1553.

- Cheng, Y. P., Nakata, Y. & Bolton, M. D. (2003) Discrete element simulation of crushable soil. *Geotechnique* **53(7)**:633-641.
- Chester, F. M., Chester, J. S., Kronenberg, A. K. & Hajash, A. (2007) Subcritical creep compaction of quartz sand at diagenetic conditions: Effects of water and grain size. *Journal of Geophysical Research: Solid Earth* **112(B6)**:n/a-n/a.
- Chester, J. S., Lenz, S. C., Chester, F. M. & Lang, R. A. (2004) Mechanisms of compaction of quartz sand at diagenetic conditions. *Earth and Planetary Science Letters* **220(3)**:435-451.
- Cho, G.-C., Dodds, J. & Santamarina, J. C. (2006) Particle shape effects on packing density, stiffness, and strength natural and crushed sands. *Journal of Geotechnical and Geoenvironmental Engineering* **132(5)**:591-602.
- Chuhan, F. A., Kjeldstad, A., Bjørlykke, K. & Heg, K. (2003) Experimental compression of loose sands: relevance to porosity reduction during burial in sedimentary basins. *Canadian Geotechnical Journal* **40(5)**:995-1011.
- Ciantia, M. O., Arroyo, M., Butlanska, J. & Gens, A. (2016) DEM modelling of cone penetration tests in a double-porosity crushable granular material. *Computers and Geotechnics* **73**:109-127.
- Cil, M. & Buscarnera, G. (2016) DEM assessment of scaling laws capturing the grain size dependence of yielding in granular soils. *Granular Matter* **18(3)**:1-15.
- Cil, M. B. & Alshibli, K. (2014) 3D Evolution of Sand Fracture Under 1D Compression. *Geotechnique* **64(5)**.

- Cil, M. B. & Alshibli, K. A. (2015) Modeling the influence of particle morphology on the fracture behavior of silica sand using a 3D discrete element method. *Comptes Rendus Mécanique* **343(2)**:133-142.
- Cil, M. B., Xie, M. & Packman, A. I. (2017) Solute mixing regulates heterogeneity of mineral precipitation in porous media: Effect of Solute Mixing on Precipitation. *Geophysical Research Letters* **44(13)**.
- Coop, M. R., Sorensent, K. K., Freitas, T. B. & Georgoutsos, G. (2004) Particle breakage during shearing of a carbonate sand. *Geotechnique* **54(3)**:157-163.
- Cundall, P. A. & Hart, R. D. (1992) NUMERICAL MODELLING OF DISCONTINUA. *Engineering Computations* **9(2)**:101-113.
- Cundall, P. A. & Strack, O. D. L. (1979) A discrete numerical model for granular assemblies. *Geotechnique* **29(1)**:47-65.
- De Gennes, P. G. (1999) Granular matter: A tentative view. *Reviews of Modern Physics* **71(2)**:S374-S382.
- Desrues, J., Chambon, R., Mokni, M. & Mazerolle, F. (1996) Void ratio evolution inside shear bands in triaxial sand specimens studied by computed tomography. *Geotechnique* **46(3)**:529-546.
- Einav, I. (2007a) Breakage mechanics—Part I: Theory. *Journal of the Mechanics and Physics of Solids* **55(6)**:1274-1297.
- Einav, I. (2007b) Breakage mechanics—Part II: Modelling granular materials. *Journal of the Mechanics and Physics of Solids* **55(6)**:1298-1320.
- Einav, I. (2007c) Soil Mechanics: Breaking Ground. *Philosophical Transactions: Mathematical, Physical and Engineering Sciences* **365(1861)**:2985-3002.

- Esna Ashari, S., Das, A. & Buscarnera, G. (2018) Model-Based Assessment of the Effect of Surface Area Growth on the Permeability of Granular Rocks. *Journal of Engineering Mechanics* **144(5)**:04018023.
- Falagush, O., Mcdowell, G. & Yu, H. (2015) Discrete Element Modeling of Cone Penetration Tests Incorporating Particle Shape and Crushing. *International Journal Of Geomechanics* **15(6)**.
- Fonseca, J., O'sullivan, C., Coop, M. R. & Lee, P. D. (2012) Non-invasive characterization of particle morphology of natural sands. *Soils and Foundations* **52(4)**.
- Freiman, S. W. (1984) Effects of chemical environments on slow crack growth in glasses and ceramics. *Journal of Geophysical Research: Solid Earth* **89(B6)**:4072-4076.
- Griffith, A. A. (1921) The Phenomena of Rupture and Flow in Solids. *Philosophical Transactions of the Royal Society of London. Series A, Containing Papers of a Mathematical or Physical Character* **221**:163-198.
- Hall, S. A., Bornert, M., Desrues, J., Pannier, Y., Lenoir, N., Viggiani, G. & Bésuelle, P. (2010) Discrete and continuum analysis of localised deformation in sand using X-ray  $\mu$ CT and volumetric digital image correlation. *Geotechnique* **60(5)**:315-322.
- Heap, M. J., Brantut, N., Baud, P. & Meredith, P. G. (2015) Time-dependent compaction band formation in sandstone. *Journal of Geophysical Research: Solid Earth* **120(7)**:4808-4830.
- Hettema, M., Papamichos, E. & Schutjens, P. (2002) Subsidence delay field observations and analysis. (Longuemare, P. (ed)), Paris, vol. 57, pp. 443-458.
- Hiramatsu, Y. & Oka, Y. (1966) Determination of the tensile strength of rock by a compression test of an irregular test piece. *International Journal of Rock Mechanics and Mining Sciences and Geomechanics Abstracts* **3(2)**:89-90.

- Hurley, R. C., Lind, J., Pagan, D. C., Akin, M. C. & Herbold, E. B. (2018) In situ grain fracture mechanics during uniaxial compaction of granular solids. *Journal of the Mechanics and Physics of Solids* **112**:273-290.
- Jaeger, H. M. & Nagel, S. R. (1996) Granular solids, liquids, and gases. *Reviews of Modern Physics* **68(4)**:1259-1273.
- Jaeger, J. C. (1967) Failure of rocks under tensile conditions. *International Journal of Rock Mechanics and Mining Sciences and Geomechanics Abstracts* **4(2)**:219-227.
- Jaky, J. (1944) The coefficient of earth pressure at rest. *J. of the Society of Hungarian Architects and Engineers*:355-358.
- Jiang, M., Shen, Z. & Wang, J. (2015) A novel three-dimensional contact model for granulates incorporating rolling and twisting resistances. *Computers and Geotechnics* **65**:147-163.
- Karatza, Z., Andò, E., Papanicolopoulos, S. A., Ooi, J. Y. & Viggiani, G. (2018) Evolution of deformation and breakage in sand studied using X-ray tomography. *Geotechnique* **68(2)**:107-117.
- Karimpour, H. & Lade, P. V. (2013) Creep behavior in Virginia Beach sand. *Canadian Geotechnical Journal* **50(11)**:1159-1178.
- Karner, S. L., Chester, F. M., Kronenberg, A. K. & Chester, J. S. (2003) Subcritical compaction and yielding of granular quartz sand. *Tectonophysics* **377(3)**:357-381.
- Komba, J., Anochie-Boateng, J. & Steyn, W. (2013) Analytical and Laser Scanning Techniques to Determine Shape Properties of Aggregates. *Transp. Res. Record*(**2335**):60-71.
- Kuwajima, K., Hyodo, M. & Hyde, A. L. (2009) Pile bearing capacity factors and soil crushability. *Journal of Geotechnical and Geoenvironmental Engineering* **135(7)**:901-913.

- Kwok, C. Y. & Bolton, M. D. (2013) DEM simulations of soil creep due to particle crushing. *Geotechnique* **63(16)**:1365-1376.
- Lade, P. V. & Karimpour, H. (2010) STATIC FATIGUE CONTROLS PARTICLE CRUSHING AND TIME EFFECTS IN GRANULAR MATERIALS. *Soils and Foundations* **50(5)**:573-583.
- Lade, P. V. & Karimpour, H. (2015) Stress relaxation behavior in Virginia Beach sand. *Canadian Geotechnical Journal* **52(7)**:813-835.
- Lade, P. V., Yamamuro, J. A. & Bopp, P. A. (1996) Significance of particle crushing in granular materials. *Journal of Geotechnical Engineering* **122(4)**:309-316.
- Lin, C. L. & Miller, J. D. (2005) 3D characterization and analysis of particle shape using X-ray microtomography (XMT). *Powder Technology* **154(1)**:61-69.
- Lixin, Y., Jie, W., Chuanqing, S., Guo, J.-W., Yanxiang, J. & Liu, B. (2010) Land subsidence disaster survey and its economic loss assessment in Tianjin, China. *Natural Hazards Review* **11(1)**:35-41.
- Marone, C., Vidale, J. E. & Ellsworth, W. L. (1995) Fault healing inferred from time dependent variations in source properties of repeating earthquakes. *Geophysical Research Letters* **22(22)**:3095-3098.
- Maugis, D. (1985) Subcritical crack growth, surface energy, fracture toughness, stick-slip and embrittlement. *Journal of Materials Science* **20(9)**:3041-3073.
- Mcdowell, G. R. (2002) On the yielding and plastic compression of sand. *Soils and Foundations* **42(1)**:139-145.
- Mcdowell, G. R. & Bolton, M. D. (1998) On the micromechanics of crushable aggregates. *Geotechnique* **48(5)**:667-679.

- Mcdowell, G. R., Bolton, M. D. & Robertson, D. (1996) The fractal crushing of granular materials. *Journal of the Mechanics and Physics of Solids* **44(12)**:2079-2101.
- Mcdowell, G. R. & De Bono, J. P. (2013) On the micro mechanics of one-dimensional normal compression. *Geotechnique* **63(11)**:895-908.
- Mcdowell, G. R. & Khan, J. J. (2003) Creep of granular materials. *Granular Matter* **5(3)**:115-120.
- Mesri, G. & Castro, A. (1987)  $C_c/C_c$  Concept and  $K_0$  During Secondary Compression. *Journal of Geotechnical Engineering* **113(3)**:230-247.
- Miura, N. & O-Hara, S. (1979) Particle-crushing of a decomposed granite soil under shear stresses. *Soils and Foundations* **19(3)**:1-14.
- Nakata, Y., Hyodo, M., Hyde, A. F. L., Kato, Y. & Murata, H. (2001a) Microscopic particle crushing of sand subjected to high pressure one-dimensional compression. *Soils and Foundations* **41(1)**:69-82.
- Nakata, Y., Kato, Y., Hyodo, M., Hyde, A. F. L. & Murata, H. (2001b) One-dimensional compression behaviour of uniformly graded sand related to single particle crushing strength. *Soils and Foundations* **41(2)**:39-51.
- Nara, Y., Yamanaka, H., Oe, Y. & Kaneko, K. (2013) Influence of temperature and water on subcritical crack growth parameters and long-term strength for igneous rocks. *Geophysical Journal International* **193(1)**:47-60.
- Nguyen, G. & Einav, I. (2009) The Energetics of Cataclasis Based on Breakage Mechanics. *Pure and Applied Geophysics* **166(10)**:1693-1724.
- O'sullivan, C. (2011) *Particulate discrete element modelling : a geomechanics perspective*. 1st ed.. edn. London New York, Spon Press/Taylor & Francis.

- Oldecop, L. A. & Alonso, E. E. (2001) A model for rockfill compressibility. *Geotechnique* **51(2)**:127-139.
- Oldecop, L. A. & Alonso, E. E. (2007) Theoretical investigation of the time-dependent behaviour of rockfill. *Geotechnique* **57(3)**:289-301.
- Ovalle, C., Dano, C. & Hicher, P.-Y. (2013) Experimental Data Highlighting the Role of Surface Fracture Energy in Quasi-Static Confined Comminution. *International Journal of Fracture* **182(1)**:123-130.
- Ovalle, C., Dano, C., Hicher, P.-Y. & Cisternas, M. (2015) Experimental framework for evaluating the mechanical behavior of dry and wet crushable granular materials based on the particle breakage ratio. *Canadian Geotechnical Journal* **52(5)**:587-598.
- Perzyna, P. (1966) Fundamental Problems in Viscoplasticity. In *Advances in Applied Mechanics*. (Chernyi, G. G., Dryden, H. L., Germain, P., Howarth, L., Olszak, W., Prager, W., Probstein, R. F., and Ziegler, H. (eds)) Elsevier, vol. 9, pp. 243-377.
- Rice, J. R. (1978) Thermodynamics of the quasi-static growth of Griffith cracks. *Journal of the Mechanics and Physics of Solids* **26(2)**:61-78.
- Rivers, M. L. (2012) tomoRecon: High-speed tomography reconstruction on workstations using multi-threading.), vol. 8506, pp. 85060U-85060U-13.
- Rivers, M. L. (2016) High-speed tomography using pink beam at GeoSoilEnviroCARS.), vol. 9967, pp. 99670X-99670X-10.
- Rivers, M. L., Citron, D. T. & Wang, Y. (2010) Recent developments in computed tomography at GSECARS.), vol. 7804, pp. 780409-7804015.
- Russell, A. & Einav, I. (2013) Energy dissipation from particulate systems undergoing a single particle crushing event. *Granular Matter* **15(3)**:299-314.

- Russell, A. R. & Muir Wood, D. (2009) Point load tests and strength measurements for brittle spheres. *International Journal of Rock Mechanics and Mining Sciences* **46(2)**:272-280.
- Sadrekarami, A. & Olson, S. M. (2010) Particle damage observed in ring shear tests on sands. *Canadian Geotechnical Journal* **47(5)**:497-515.
- Salgado, R., Mitchell, J. K. & Jamiolkowski, M. (1997) Cavity expansion and penetration resistance in sand. *Journal of Geotechnical and Geoenvironmental Engineering* **123(4)**:344-354.
- Shahnazari, H. & Rezvani, R. (2013) Effective parameters for the particle breakage of calcareous sands an experimental study. *Engineering Geology* **159**:98-105.
- Shipway, P. H. & Hutchings, I. M. (1993) Fracture of brittle spheres under compression and impact loading. I. Elastic stress distributions. *Philosophical Magazine A* **67(6)**:1389-1404.
- Sohn, C., Zhang, Y., Cil, M. & Buscarnera, G. (2017) Experimental assessment of continuum breakage models accounting for mechanical interactions at particle contacts. *Granular Matter* **19(4)**:1-14.
- Takei, M., Kusakabe, O. & Hayashi, T. (2001) Time-dependent behavior of crushable materials in one-dimensional compression tests. *Soils and Foundations* **41(1)**:97-121.
- Tapias, M., Alonso, E. E. & Gili, J. (2015) A particle model for rockfill behaviour. *Geotechnique* **65(11)**:975-994.
- Tavares, L. M. & King, R. P. (1998) Single-particle fracture under impact loading. *International Journal of Mineral Processing* **54(1)**:1-28.
- Tenthorey, E., Cox, S. F. & Todd, H. F. (2003) Evolution of strength recovery and permeability during fluid-rock reaction in experimental fault zones. *Earth and Planetary Science Letters* **206(1-2)**:161-172.

- Ueda, T., Matsushima, T. & Yamada, Y. (2013) DEM simulation on the one-dimensional compression behavior of various shaped crushable granular materials. *Granular Matter* **15(5)**:675-684.
- Wang, F. W., Sassa, K. & Wang, G. (2002) Mechanism of a long-runout landslide triggered by the August 1998 heavy rainfall in Fukushima Prefecture, Japan. *Engineering Geology* **63(1)**:169-185.
- Wiederhorn, S. M. (1974) Subcritical Crack Growth in Ceramics. In *Fracture Mechanics of Ceramics: Volume 2 Microstructure, Materials, and Applications*. (Bradt, R. C., Hasselman, D. P. H., and Lange, F. F. (eds)) Springer US, Boston, MA, pp. 613-646.
- Wiederhorn, S. M., Fuller, E. R. & Thomson, R. (1980) Micromechanisms of crack growth in ceramics and glasses in corrosive environments. *Metal Science* **14(8-9)**:450-458.
- Wong, T.-F. & Baud, P. (2012) The brittle-ductile transition in porous rock: A review. *Journal of Structural Geology* **44**:25-53.
- Yamamuro, J. A. (1996) One-dimensional compression of sands at high pressures. *Journal of Geotechnical Engineering* **122(2)**:147-155.
- Yang, Z. X., Jardine, R. J., Zhu, B. T., Foray, P. & Tsuha, C. H. C. (2010) Sand grain crushing and interface shearing during displacement pile installation in sand. *Geotechnique* **60(6)**:469-482.
- Yashima, S., Kanda, Y. & Sano, S. (1987) Relationships between particle size and fracture energy or impact velocity required to fracture as estimated from single particle crushing. *Powder Technology* **51(3)**:277-282.
- Zhang, J., Wong, T.-F. & Davis, D. M. (1990) Micromechanics of pressure-induced grain crushing in porous rocks. *Journal of Geophysical Research: Solid Earth* **95(B1)**:341-352.

- Zhang, Y. & Buscarnera, G. (2014) Grainsize dependence of elastic yielding in unsaturated granular soils. *Granular Matter* **16(4)**:469-483.
- Zhang, Y. & Buscarnera, G. (2018) Breakage mechanics for granular materials in surface-reactive environments. *Journal of the Mechanics and Physics of Solids* **112**:89-108.
- Zhang, Y. D. & Buscarnera, G. (2017) A rate-dependent breakage model based on the kinetics of crack growth at the grain scale. *Geotechnique* **67(11)**:953-967.
- Zhang, Y. D., Buscarnera, G. & Einav, I. (2016) Grain size dependence of yielding in granular soils interpreted using fracture mechanics, breakage mechanics and Weibull statistics. *Geotechnique* **66(2)**:149-160.
- Zhao, B., Wang, J., Coop, M. R., Viggiani, G. & Jiang, M. (2015) An investigation of single sand particle fracture using x-ray micro-tomography. *Geotechnique* **65(8)**:625-641.
- Zhao, Z. & Song, E.-X. (2015) Particle mechanics modeling of creep behavior of rockfill materials under dry and wet conditions. *Computers and Geotechnics* **68**:137-146.

## APPENDIX A: FRACTURE MODELS

### A.1 Surface Crack Model

The failure load due to the surface crack can be expressed as follows (Zhang et al., 2016):

$$F_f = \frac{9}{64} \left( \frac{2\pi b'}{1-2\nu} \right)^3 \left( \frac{1-\nu^2}{E} \right)^{1/2} G_{IC}^{3/2} d_p^{1/2} \quad (4.11)$$

where  $b' = \frac{1}{1.12} \left( \frac{\pi\alpha}{2} \right)^{-1/2}$  is a coefficient associated with the crack geometry, while  $\alpha$  is a dimensionless crack size (i.e., the crack length normalized for the particle diameter).  $G_{IC}$  is the critical energy release rate (here assumed to be 0.95 J/m<sup>2</sup>).

### A.2 Central Crack Model

The failure load for central split of a particle can be expressed through the following equation (Zhang et al., 2016):

$$F_f = \frac{\pi a'}{2.8} \sqrt{\frac{G_{IC} E}{1-\nu^2}} d_p^{3/2} \quad (4.12)$$

where  $a' = \frac{\sqrt{\pi}}{\sqrt{2\alpha}}$  is a coefficient associated with the crack geometry,  $G_{IC}$  is the critical energy release rate (here assumed to be 0.95 J/m<sup>2</sup>) and the coefficients  $a'$  and  $b'$  are associated with the dimensionless crack size.

## APPENDIX B: CONTACT MODELS

### B.1 Linear Contact Model

A linear contact involves a constant contact area (i.e., not altered by the applied force). This type of contact is here modeled through the following force-displacement law:

$$F = \frac{E\pi a_c^2}{R} \delta \quad (4.13)$$

where  $a_c$  is the contact radius;  $R$  is the particle radius; and  $\delta$  is the contact deformation ( $\delta = \Delta/2$ ).

By substituting Eq. (4.13) into Eq. (4.2), the relation between characteristic particle strength and energy stored at the onset of fracture can be expressed as follows:

$$E_{pc} = \frac{12}{E\pi^2} \left( \frac{a_c}{R} \right)^{-2} \sigma_{pc}^2 \quad (4.14)$$

### B.2 Hertzian Contact Model

In case of the contact between an elastic particle and a rigid loading plate, the force-displacement response for a Hertzian contact can be expressed through the following relations:

$$F = \frac{4}{3} R^{1/2} \left( \frac{1-\nu^2}{E} \right)^{-1} \delta^{3/2} \quad (4.15)$$

By substituting Eq. (4.15) into Eq. (4.2), the relation between characteristic particle strength and the energy stored at the onset of fracture can be expressed as follows:

$$E_{pc} = 4.989 \frac{1}{\pi} \left( \frac{1-\nu^2}{E} \right)^{2/3} \sigma_{pc}^{5/3} \quad (4.16)$$

### B.3 Conical Contact Model

The load-displacement relation for a conical contact model derived by Zhang et al. (2016) can be expressed as follows:

$$F = \frac{E}{1-\nu^2} \left( \frac{2}{\pi A_s} \right)^{1/2} \delta^2 \quad (4.17)$$

By substituting Eq. 4.17 into Eq. (4.2), the relation between characteristic particle strength and the energy stored at the onset of fracture is:

$$E_{pc} = 3.360 A_s^{1/4} \pi^{-(3/4)} \left( \frac{1-\nu^2}{E} \right)^{1/2} \sigma_{pc}^{3/2} \quad (4.18)$$

where  $A_s$  is the tangent of the contact angle between the particle and a horizontal surface (Zhang et al., 2016).

## APPENDIX C: COMBINATION OF FAILURE MODEL AND CONTACT MODEL

It is possible to express the characteristic particle strength,  $\sigma_{pc}$ , in Eqs. (4.14), (4.16), and (4.18) in terms of grain size by combining Eqs. (4.11) and (4.12) with Eq. (4.1). While the failure model based on central splitting can be combined with any of three contact models, the failure criterion based on surface fracture can only be used in combination with a Hertzian contact law. Therefore, four expressions of  $E_{pc}$  are obtained as a function of the grain size,  $d$ .

### C.1 Surface Crack

#### C.1.1 Hertzian contact model

Eq. (4.11) can be expressed as a function of  $\sigma_{pc}$  by using Eq. (4.1). By substituting the resulting expression into Eq. (4.16) gives:

$$E_{pc} = 6.071\pi^{-1}b^5 \left( \frac{1-\nu^2}{E} \right)^{3/2} \left( \frac{\pi}{1-2\nu} \right)^5 G_{IC}^{5/2} d_p^{-5/2} \quad (4.19)$$

### C.2 Central Crack

Eq. (4.12) can be expressed as a function of  $\sigma_{pc}$  by using Eq. (4.1). Then, by substituting the resulting expression into Eqs. (4.14), (4.16) and (4.18) the following relations are obtained:

#### C.2.1 Linear contact model

$$E_{pc} = 1.531a' \left( \frac{a_c}{R} \right)^{-2} \left( \frac{G_{IC}}{1-\nu^2} \right) d_p^{-1} \quad (4.20)$$

#### C.2.2 Hertzian contact model

$$E_{pc} = 0.897\pi^{2/3} a'^{5/3} \left( \frac{1-\nu^2}{E} \right)^{-1/6} G_{IC}^{5/6} d_p^{-5/6} \quad (4.21)$$

*C.2.3 Conical contact model*

$$E_{pc} = 0.717 A_s^{1/4} \pi^{3/4} a^{3/2} \left( \frac{1-\nu^2}{E} \right)^{-1/4} G_{IC}^{3/4} d_p^{-3/4} \quad (4.22)$$

## APPENDIX D: TIME-TO-FAILURE OF PARTICLE BASED ON SUBCRITICAL CRACK GROWTH THEORY

Maugis Law

$$\dot{l} = \dot{l}_o \times \left( \frac{G}{2\gamma} - 1 \right)^{n/2} \quad \text{Eq (D.1)}$$

Griffith Criterion

$$G = \frac{K_1^2}{E}$$

$$K_1 = \sigma \sqrt{\pi a}$$

$$\therefore G = \frac{\sigma^2 \pi a}{E} = \frac{\sigma^2 \pi l}{2E} \quad \text{Eq (D.2)}$$

Particle Failure Model

Substitute Eq (D.2) into Eq (D.1)

$$\dot{l} = \dot{l}_o \times \left( \frac{\sigma^2 \pi l}{4E\gamma} - 1 \right)^{n/2}$$

$$\frac{\dot{l}}{\dot{l}_o} = \left( \frac{\sigma^2 \pi l}{4E\gamma} - 1 \right)^{n/2} ; \dot{l} = \frac{dl}{dt}$$

$$\frac{1}{\dot{l}_o} \frac{dl}{dt} = \left( \frac{\sigma^2 \pi l}{4E\gamma} - 1 \right)^{n/2}$$

$$\frac{1}{\dot{l}_o} \left( \frac{\sigma^2 \pi l}{4E\gamma} - 1 \right)^{-n/2} dl = dt$$

$$\frac{1}{\dot{l}_o} \int \left( \frac{\sigma^2 \pi l}{4E\gamma} - 1 \right)^{-n/2} dl = \int dt \quad \text{Eq (D.3)}$$

Let's say

$$\xi = \frac{\sigma^2 \pi l}{4E\gamma} - 1 \quad \text{Eq (D.4)}$$

From Eq (D.4),

$$\begin{aligned} \frac{d\xi}{dl} &= \frac{\sigma^2 \pi}{4E\gamma} \\ \therefore dl &= \frac{4E\gamma}{\sigma^2 \pi} d\xi \end{aligned} \quad \text{Eq (D.5)}$$

Substitute Eq (D.5) into Eq (D.3)

$$\begin{aligned} \frac{1}{\dot{l}_o} \int \xi^{-n/2} \left( \frac{4E\gamma}{\sigma^2 \pi} \right) d\xi &= \int dt \\ \frac{1}{\dot{l}_o} \left( \frac{4E\gamma}{\sigma^2 \pi} \right) \int \xi^{-n/2} d\xi &= \int dt \\ \therefore \frac{1}{\dot{l}_o} \left( \frac{4E\gamma}{\sigma^2 \pi} \right) \frac{1}{1-n/2} \xi^{1-n/2} &= t + c \end{aligned} \quad \text{Eq (D.6)}$$

At  $l = l_o$ , Eq (D.4) becomes

$$\xi = \xi_o = \frac{\sigma^2 \pi l_o}{4E\gamma} - 1 \quad \text{Eq (D.7)}$$

Substitute Eq (D.7) into Eq (D.6) and  $t = 0$  gives

$$\frac{1}{\dot{l}_o} \left( \frac{4E\gamma}{\sigma^2 \pi} \right) \frac{1}{1-n/2} \left[ \frac{\sigma^2 \pi l_o}{4E\gamma} - 1 \right]^{1-n/2} = c \quad \text{Eq (D.8)}$$

Substitute Eq (D.8) into Eq (D.6)

$$t = \frac{1}{\dot{l}_o} \left( \frac{4E\gamma}{\sigma^2 \pi} \right) \frac{1}{1-n/2} \left[ \left( \frac{\sigma^2 \pi l}{4E\gamma} - 1 \right)^{1-n/2} - \left( \frac{\sigma^2 \pi l_o}{4E\gamma} - 1 \right)^{1-n/2} \right] \quad \text{Eq (D.9)}$$

Note that

$$\xi = \frac{\sigma^2 \pi l}{4E\gamma} - 1 = 0 \quad \text{if } l = \infty \text{ (e.g., failure)}$$

Rearrange Eq (D.9) gives

$$\left(\frac{\sigma^2 \pi l}{4E\gamma} - 1\right)^{1-n/2} = i_o \left(\frac{\sigma^2 \pi}{4E\gamma}\right) (1-n/2)t + \left(\frac{\sigma^2 \pi l_o}{4E\gamma} - 1\right)^{1-n/2}$$

Let's say

$$A(t) = i_o \left(\frac{\sigma^2 \pi}{4E\gamma}\right) (1-n/2)t + \left(\frac{\sigma^2 \pi l_o}{4E\gamma} - 1\right)^{1-n/2}$$

then,

$$\left(\frac{\sigma^2 \pi l}{4E\gamma} - 1\right)^{1-n/2} = A(t)$$

$$\frac{\sigma^2 \pi l}{4E\gamma} - 1 = A(t)^{1/(1-n/2)}$$

$$\frac{\sigma^2 \pi l}{4E\gamma} = 1 + A(t)^{1/(1-n/2)}$$

$$\therefore l(t) = \frac{4E\gamma}{\sigma^2 \pi} \left[ 1 + A(t)^{1/(1-n/2)} \right] \quad \text{Eq (D.10)}$$

From Eq (D.9), time to failure occurs at  $l \rightarrow \infty$

$$\left(\frac{\sigma^2 \pi l}{4E\gamma} - 1\right)^{1-n/2} = 0$$

Therefore, time to failure is

$$t_f = \frac{1}{i_o} \left(\frac{4E\gamma}{\sigma^2 \pi}\right) \frac{1}{1-n/2} \left[ -\left(\frac{\sigma^2 \pi l_o}{4E\gamma} - 1\right)^{1-n/2} \right] \quad \text{Eq (D.11)}$$